

1 **Organic Aerosol Composition and Sources in Pasadena, California during the**
2 **2010 CalNex Campaign**

3
4 P. L. Hayes^{1,2}, A. M. Ortega^{1,3}, M. J. Cubison^{1,2}, K. D. Froyd^{1,4}, Y. Zhao⁵, S. S. Cliff⁵, W. W.
5 Hu^{1,6}, D. W. Toohey³, J. H. Flynn⁷, B. L. Lefer⁷, N. Grossberg⁷, S. Alvarez⁷, B. Rappenglück⁷, J.
6 W. Taylor⁸, J. D. Allan^{8,9}, J. S. Holloway^{1,4}, J. B. Gilman^{1,4}, W. C. Kuster⁴, J. A. de Gouw^{1,4}, P.
7 Massoli¹⁰, X. Zhang¹¹, J. Liu¹¹, R. J. Weber¹¹, A. L. Corrigan¹², L. M. Russell¹², G. Isaacman¹³,
8 D. R. Worton^{13,14}, N. M. Kreisberg¹⁴, A. H. Goldstein¹³, R. Thalman^{1,2}, E. M. Waxman^{1,2}, R.
9 Volkamer^{1,2}, Y. H. Lin¹⁵, J. D. Surratt¹⁵, T. E. Kleindienst¹⁶, J. H. Offenberg¹⁶, S. Dusanter^{17,18,19},
10 S. Griffith¹⁷, P. S. Stevens¹⁷, J. Brioude^{1,4}, W. M. Angevine^{1,4}, J. L. Jimenez^{1,2}

11
12 (1) Cooperative Institute for Research in the Environmental Sciences (CIRES), Univ. of
13 Colorado, Boulder, CO, USA

14 (2) Dept. of Chemistry and Biochemistry, Univ. of Colorado, Boulder, CO, USA

15 (3) Dept. of Atmospheric and Oceanic Sciences, Univ. of Colorado, Boulder, CO, USA

16 (4) NOAA Chemical Sciences Division, Boulder, CO, USA

17 (5) Univ. of California, Davis, CA, USA

18 (6) College of Environmental Sciences and Engineering, Peking Univ., China

19 (7) Dept. of Earth and Atmospheric Sciences, Univ. of Houston, TX, USA

20 (8) School of Earth, Atmospheric, and Environmental Sciences, The Univ. of Manchester,
21 Manchester, UK

22 (9) National Centre for Atmospheric Science, The Univ. of Manchester, Manchester, UK

23 (10) Aerodyne Research Inc., Billerica, MA, USA

24 (11) Georgia Institute of Technology, Atlanta, GA, USA

25 (12) Scripps Institution of Oceanography, Univ. of California San Diego, La Jolla, CA, USA

26 (13) Univ. of California, Berkeley, CA, USA

27 (14) Aerosol Dynamics Inc., Berkeley, CA, USA

28 (15) Dept. of Environmental Sciences and Engineering, Univ. of North Carolina, Chapel Hill,
29 NC USA

30 (16) US Environmental Protection Agency, Research Triangle Park, NC, USA

31 (17) Center for Research in Environmental Science, School of Public and Environmental Affairs,
32 and Department of Chemistry, Indiana Univ., Bloomington, IN, USA

33 (18) Univ Lille Nord de France, F-59000 Lille, France

34 (19) EMDouai, CE, F-59508 Douai, France

35
36 *Correspondence to:* J. L. Jimenez (jose.jimenez@colorado.edu)

37
38 Running title: Aerosol Composition in Los Angeles

39
40 Index terms: 0365 (Troposphere: composition and chemistry), 0305 (Aerosols and particles),
41 0345 (Pollution: urban and regional)

42
43 Keywords: Organic aerosol, Los Angeles, CalNex, Positive Matrix Factorization, Particulates

44 **Abstract**

45 Organic aerosols (OA) in Pasadena are characterized using multiple measurements from the
46 CalNex campaign. Five OA components are identified using positive matrix factorization
47 including hydrocarbon-like OA (HOA), and two types of oxygenated OA (OOA). The Pasadena
48 OA elemental composition when plotted as H:C versus O:C follows a line less steep than that
49 observed for Riverside, California. The OOA components from both locations follow a common
50 line, however, indicating similar secondary organic aerosol (SOA) oxidation chemistry at the two
51 sites such as fragmentation reactions leading to acid formation. In addition to the similar
52 evolution of elemental composition, the dependence of SOA concentration on photochemical age
53 displays quantitatively the same trends across several North American urban sites. First, the
54 OA/ Δ CO values for Pasadena increase with photochemical age exhibiting a slope identical to or
55 slightly higher than those for Mexico City and the northeastern United States. Second, the ratios
56 of OOA to odd-oxygen (a photochemical oxidation marker) for Pasadena, Mexico City, and
57 Riverside are similar, suggesting a proportional relationship between SOA and odd-oxygen
58 formation rates. Weekly cycles of the OA components are examined as well. HOA exhibits
59 lower concentrations on Sundays versus weekdays, and the decrease in HOA matches that
60 predicted for primary vehicle emissions using fuel sales data, traffic counts, and vehicle emission
61 ratios. OOA does not display a weekly cycle – after accounting for differences in photochemical
62 aging and emissions – which suggests the dominance of gasoline emissions in SOA formation
63 under the assumption that most urban SOA precursors are from motor vehicles.

64

65 **1. Introduction**

66 Atmospheric aerosols have been the subject of intensive ongoing research due to their
67 important impacts on the radiative forcing of climate, which occur through several mechanisms
68 that include the scattering and absorption of solar radiation as well as the alteration of the
69 formation and properties of clouds [IPCC, 2007]. In addition, atmospheric aerosols reduce
70 visibility [Watson, 2002] and increase cardiac and respiratory disease in humans [Dockery *et al.*,
71 1994; Dockery *et al.*, 1993]. The impact of aerosols on climate, the environment, and human
72 health is determined, in part, by particle size and chemical composition. In many environments a
73 large fraction (~50%) of the submicron aerosol mass in the troposphere is organic aerosol (OA),
74 but the sources, composition and chemical processing of OA are not well understood [Jimenez *et*
75 *al.*, 2009]. Generally, OA is comprised of thousands of individual compounds that are either
76 directly emitted into the atmosphere (i.e. ‘primary’ OA or ‘POA’) or formed through chemical
77 reactions involving gas phase precursors (i.e. ‘secondary’ OA or ‘SOA’). The multiple sources
78 and complexity of molecular composition represent major challenges for understanding and
79 prediction of OA properties.

80 Elevated aerosol concentrations are often associated with megacities such as Los Angeles
81 (LA). Particulate matter concentrations in LA are among the highest in the United States
82 [American Lung Association, 2011], and multiple previous measurement campaigns have aimed
83 to characterize aerosols in this region. These campaigns include the 1987 Southern California Air
84 Quality Study (SCAQS) [Lawson, 1990], the 1997 Southern California Ozone Study (SCOS97-
85 NARSTO) [Croes *et al.*, 2003], the Study of Organic Aerosol at Riverside, which took place in
86 the Summer (SOAR-1) and Fall (SOAR-2) of 2005 [Docherty *et al.*, 2011], and the 2009
87 Pasadena Aerosol Characterization Observatory (PACO) [Hersey *et al.*, 2011]. In addition,

88 several research flights were performed over California and LA during the Arctic Research of the
89 Composition of the Troposphere from Aircraft and Satellites Campaign (ARCTAS-CARB)
90 [Jacob *et al.*, 2010]. Using data from these campaigns it has been shown that SOA represents a
91 majority of the total OA mass in both Riverside [Docherty *et al.*, 2008] and Pasadena, CA
92 [Hersey *et al.*, 2011], which is similar to findings in other urban regions [Jimenez *et al.*, 2009].
93 The gas phase precursors for SOA potentially have many sources including vehicle emissions,
94 the biosphere, biomass burning, and food cooking [Bahreini *et al.*, 2012; Hodzic *et al.*, 2010;
95 Schauer *et al.*, 1999; 2002b]. Also, vehicle emissions, food cooking, biomass burning, and
96 primary biogenics have all been identified as sources of POA in the South Coast Air Basin
97 [Williams *et al.*, 2010; Wonaschutz *et al.*, 2011].

98 The California Research at the Nexus of Air Quality and Climate Change (CalNex) field
99 campaign was conducted in Spring 2010, and was a multi-institution effort to address
100 outstanding questions regarding atmospheric chemistry processes over the state of California and
101 the adjacent Pacific coastal region [Ryerson *et al.*, manuscript submitted for J. Geophys. Res.-
102 Atmos., 2012]. The CalNex campaign featured several research aircraft, the research vessel
103 Atlantis off the California coast, and two ground sites in Pasadena and Bakersfield. A major
104 scientific goal for CalNex was to improve scientific understanding of atmospheric aerosols in
105 California, and specifically, characterize important SOA precursors and formation pathways, as
106 well as the impacts of aerosols on radiative forcing and cloud formation [NOAA, 2008]. For
107 CalNex the Pasadena ground site was uniquely equipped to characterize aerosols, and especially,
108 organic aerosols. In total approximately 70 gas and particle phase measurements were taken at
109 the site representing, to our knowledge, one of the largest studies of aerosols and their
110 precursors. A full list of the instrumentation is available in the CalNex overview [Ryerson *et al.*,

111 manuscript submitted for J. Geophys. Res.-Atmos., 2012] and also at: <http://tinyurl.com/CalNex>.
112 Additionally, the ground site featured many state-of-the-art aerosol instruments including several
113 that had never been field-deployed previously.

114 Here we present a detailed analysis of aerosol measurements from multiple instruments,
115 including on- and off-line bulk and single particle methods, deployed to the Pasadena ground site
116 during CalNex. The goals of this work are to quantitatively evaluate SOA formation for the
117 South Coast Air Basin and compare it against other major urban regions, as well as to determine
118 the contributions of various sources to organic aerosol mass loadings. In particular, the relative
119 importance of diesel versus gasoline emissions in secondary organic aerosol formation has been
120 a source of scientific controversy [*Bahreini et al.*, 2012; *Gentner et al.*, 2012] and will be
121 examined here. To achieve these goals the following approach is utilized: (1) using positive
122 matrix factorization (PMF) the components of OA are identified and characterized (Section 3.2),
123 (2) the POA emission ratios with elemental carbon (EC) and CO are determined and rationalized
124 (Section 3.3), (3) the dependence of SOA concentration on photochemical age is quantified and
125 compared against previous measurements conducted in Riverside, Mexico City, and the
126 northeastern United States (Section 3.4), and (4) the weekly cycles (or lack thereof) in POA and
127 SOA concentrations are analyzed in the context of understanding the relative contributions to
128 each from diesel and gasoline motor vehicles (Section 3.5). The unique findings of this work
129 include the observation of a similar SOA formation rate for Pasadena versus other urban
130 locations, the first reported weekly cycle for POA concentrations, and an improved analysis of
131 the contribution of diesel emissions to SOA formation based on the lack of a weekly cycle in
132 SOA concentrations.

133

134 **2. Experimental**

135 **2.1. CalNex ground site in Pasadena, California**

136 The CalNex Pasadena ground site was located on the California Institute of Technology
137 (Caltech) campus in Pasadena, California (34.1406 N, 118.1225 W, 236 m above mean sea
138 level). The measurement period was May 15 2010 00:00 – June 16 2010 00:00 (local time). The
139 Pasadena ground site was located 18 km northeast of downtown Los Angeles. Pasadena lies
140 within the South Coast Air Basin, which is bordered on the north and east by the San Gabriel,
141 San Bernardino, and San Jacinto mountains as well as on the southwest by the Pacific Ocean.
142 Pasadena is part of the dense, urban Los Angeles metropolitan area. The prevailing wind
143 direction during daytime in Pasadena was from the southwest due to the sea-breeze, which
144 brought air masses from the Santa Monica and San Pedro Bays through central Los Angeles to
145 Pasadena (FLEXPART back-trajectories are available in Section A of the Supporting Material).
146 At nighttime winds were weaker and were most frequently from the southwest or southeast.
147 Sunrise and sunset were approximately 5:30 and 20:00 (local time) during the sampling period.
148 Boundary layer height, temperature, and relative humidity (RH) data are presented in the
149 Supporting Material (Figure A-1) along with wind roses (Figure A-2).

150 **2.2. AMS sampling and analysis**

151 The concentrations of submicron non-refractory (nrPM₁) organic and inorganic (nitrate,
152 sulfate, ammonium, chloride) aerosol particles were measured using an Aerodyne High
153 Resolution Time-of-Flight Aerosol Mass Spectrometer (hereinafter referred to as ‘AMS’)
154 [DeCarlo *et al.*, 2006]. The AMS sampled from an inlet equipped with a PM_{2.5} cyclone located 2
155 m above the roof of the container housing the instrument. The sampled air passed through a 6.8

156 m insulated copper inlet line and a dryer prior to analysis by the AMS. The resulting data were
157 averaged over 2.5 minute intervals. The ion paths through the time-of-flight chamber were
158 alternated between “V” and “W” modes every 150 s, and the reported concentrations correspond
159 to V-mode acquisition periods only. Size distributions were acquired during every V-mode
160 acquisition by operating the AMS in particle time-of-flight (PToF) mode [Jimenez *et al.*, 2003].
161 All data were analyzed using standard AMS software (SQUIRREL v1.51 and PIKA v1.10)
162 within Igor Pro 6.2.1 (WaveMetrics, Lake Oswego, OR) [Sueper, 2011].

163 It is well-known that for most ambient sampling conditions a collection efficiency (CE)
164 correction must be applied to the AMS data to account for particle bounce from the AMS
165 vaporizer [Middlebrook *et al.*, 2012]. Mass concentrations are typically calculated with a default
166 CE of 0.5. The degree to which particles bounce, and hence collection efficiency, are a function
167 of particle phase, which is influenced by the relative humidity of the sampling line, the
168 acidity/neutralization of the sulfate content, the ammonium nitrate content, and the organic liquid
169 content [Middlebrook *et al.*, 2012]. The sample flow was dried as described above, and the
170 sulfate content was largely neutralized (see Appendix). Thus, these experimental parameters are
171 not expected to impact CE. Ammonium nitrate concentrations varied widely during the
172 measurement period though, and accordingly a nitrate-dependent CE is applied following Nemitz
173 *et al.* [2010]. Quantifying the organic liquid content is challenging for ambient samples, however
174 the ratio of AMS mass to Scanning Mobility Particle Sizer (SMPS) mass exhibits no dependence
175 on the amount of OA oxidation as measured by O:C indicating that phase changes associated
176 with organic material are either not occurring or are not influencing the particle bounce and CE.
177 In total, the aerosol mass concentrations measured by the AMS after applying the CE correction,
178 which ranged from 0.5 to 0.7, are consistent with most other measurements from the Pasadena

179 ground site. The relevant inter-comparisons are discussed in Section B of the Supporting
180 Material for this paper, including details regarding how mass concentrations are calculated from
181 SMPS number distributions.

182 High-resolution (HR) analysis of the mass spectra, including application of the HR AMS
183 fragmentation table, was carried out following previously published procedures [Aiken *et al.*,
184 2007, 2008]. The reported AMS mass concentrations were determined from the HR AMS spectra
185 and are very similar to unit mass resolution (UMR) concentrations, within 5%, that are
186 determined using the UMR fragmentation table of Allan *et al.* [2004]. The HR fragmentation
187 table was also used to obtain the OA mass spectral matrix for the PMF analysis described in the
188 next paragraph.

189 The OA mass spectral matrix was deconvolved into components using PMF, a receptor-
190 based factorization model [Paatero *et al.*, 1994]. The application of PMF to AMS spectra has
191 been discussed in detail previously [Ulbrich *et al.*, 2009; Q Zhang *et al.*, 2011]. The same
192 method is used here including the PMF2 algorithm, which is run in robust mode via the PMF
193 Evaluation Tool panel (PET, v2.03). The high-resolution organic aerosol mass spectra for the
194 entire CalNex campaign were analyzed, and the full range of the high-resolution spectra was
195 utilized (m/z 12 – 204). Error matrices were calculated using the methods of Allan *et al.* [2003]
196 and Ulbrich *et al.* [2009]. Weak variables (i.e. m/z 's) with lower signal-to-noise ratios ($0.2 < S/N$
197 < 2) were down-weighted by a factor of three, and bad variables ($S/N \leq 0.2$) were down-weighted
198 by a factor of 10 following the recommendations of Paatero and Hopke [2003]. For the results
199 presented here the model error was set to zero.

200

201 2.3. Co-located CalNex measurements utilized in this study

202 A SMPS (Model 3936, TSI Inc.) measured ambient number distributions between 7 and
203 690 nm mobility diameter. The SMPS was operated at a sampling frequency of 5 min and used
204 the same inlet as the AMS (including drier) except that the aerosol flow passed through an
205 additional 2.1 m of copper inlet line (0.3 lpm flow). For the SMPS the aerosol flow rate was 0.3
206 lpm and the sheath flow rate was 3 lpm. Ambient particle number distributions were also
207 measured from 60 to 1000 nm using an Ultra-High Sensitivity Aerosol Spectrometer (UHSAS,
208 Droplet Measurement Technologies), which also used the same inlet as the AMS (including
209 drier), but the sample flow passed through an additional 2 m of inlet line (0.3 lpm flow). A
210 White-Light Optical Particle Counter (WLOPC, Climet model 208 fitted with a multi-channel
211 analyzer) measured size distributions from 500 to 4000 nm. Hourly PM_{2.5} organic carbon (OC)
212 and elemental carbon (EC) concentrations were measured using a Sunset Labs field OC/EC
213 analyzer [Peltier *et al.*, 2007]. Blank-corrected optical OC and EC data from the Sunset field
214 analyzer are reported here. Measurements of refractory black carbon (rBC) were performed with
215 a Single Particle Soot Photometer (SP2, Droplet Measurement Technologies) [Schwarz *et al.*,
216 2006], as well as with a Soot Particle Aerosol Mass Spectrometer (SP-AMS, Aerodyne Research
217 & Droplet Measurement Technology) [Onasch *et al.*, 2012]. The concentrations of semi-volatile
218 and particulate organic molecular tracers were measured by 2-D Thermal Desorption Aerosol
219 Gas Chromatography Mass Spectrometry (2DTAG, UC-Berkeley & Aerosol Dynamics) [Worton
220 *et al.*, 2012]. PM_{2.5} nitrate and sulfate concentrations were measured with a Particle-into-Liquid
221 Sampling and Ion Chromatography (PILS-IC) system [Orsini *et al.*, 2003]. The Particle Analysis
222 by Laser Mass Spectrometry (PALMS) instrument provided number fractions for individual
223 particle composition classes from 190 – 4000 nm [Froyd *et al.*, 2009; Thomson *et al.*, 2000].

224 The PALMS instrument also measures scattered light from single particles allowing for
225 calculation of particle size in addition to particle classification. Volume concentrations of the
226 different PALMS particle classes were calculated by multiplying the volume concentration size
227 distribution determined from the SMPS or WLOPC measurements by the fractions of the
228 different PALMS particle types in each size bin. Particle optical extinction for PM_{10} was
229 measured at 532 nm and 630 nm by a Cavity Attenuated Phase Shift (CAPS) instrument
230 [Kebabian *et al.*, 2007; Massoli *et al.*, 2010]. All of the online measurements described in this
231 paragraph were located at the CalNex ground site described above.

232 Data from offline particulate matter measurements are included in this paper as well. In
233 particular, size-resolved elemental concentrations were determined by X-ray Fluorescence (XRF)
234 analysis of Mylar substrates from a rotating drum impactor (RDI). The XRF analysis was
235 performed at the Advanced Light Source at Lawrence Berkeley National Lab. Using the XRF
236 results, the mineral dust concentration corresponding to oxides of Al, Si, Ca, K, Fe, and Ti is
237 estimated from the elemental concentrations following the method of Simon *et al.* [2011] and
238 Malm *et al.* [1994]. The particulate metal concentration is calculated as the sum of the mass
239 concentrations of Mg, V, Cr, Mn, Co, Ni, Cu, Zn, Ga, As, Se, Rb, Sr, Y, Zr, Mo, and Pb. The Cl
240 concentrations from XRF measurements are reported as refractory chloride (rCl), since the
241 placement of samples under vacuum for analysis is expected to cause evaporation of non-
242 refractory species such as ammonium chloride. The time resolution of the XRF data was 1.5 h.
243 Offline OC measurements of high volume $PM_{2.5}$ samples collected with quartz fiber filters were
244 performed using three separate sets of filters and two laboratory-based Sunset Labs OC/EC
245 analyzers (NIOSH TOT protocol). For clarity, the three sets of filters are named according to the
246 institution that collected them: Georgia Institute of Technology (GIT), U.S. Environmental

247 Protection Agency (EPA), and University of North Carolina (UNC). Following the technique of
248 Russell et al. [2009], Fourier Transform Infrared Spectroscopy (FTIR) analysis of Teflon filter
249 samples provided PM_{2.5} OA and organic functional group mass concentrations. All samples for
250 offline analyses were collected at about 12 m above ground level on the roof of the Keck
251 Building located on the Caltech campus approximately 0.3 km southwest of the ground site.

252 The concentration of O₃ was measured by UV differential absorption (49c Ozone
253 Analyzer, Thermo Scientific), and CO concentrations were measured by two vacuum-UV
254 resonance fluorescence instruments (AL5001 & AL5002, Aerolaser) [Gerbig et al., 1999]. An
255 in-situ Gas Chromatography Mass Spectrometry (GC-MS) instrument provided the mixing ratios
256 for a variety of VOCs [Gilman et al., 2009]. A Fluorescence Assay by Gas Expansion (FAGE)
257 instrument was utilized to determine the OH concentration [Dusanter et al., 2009]. The NO_x and
258 NO_y concentrations were measured using chemiluminescence (42i-TL with Mo converter,
259 Thermo Scientific), and NO₂ was measured with Cavity Enhanced Differential Optical
260 Absorption Spectroscopy (CE-DOAS) [Thalman et al., 2010]. The CE-DOAS instrument was
261 located on the Caltech Millikan Library roof, which is approximately 45 m tall and 0.5 km
262 southwest of the Pasadena ground site.

263 Meteorological data were acquired by a station that included a temperature/RH sensor
264 (Campbell Scientific Inc., HMP35C) and a wind monitor (R.M. Young, 05103). The boundary
265 layer height was determined using a ceilometer (Vaisala, CL31) following the method described
266 by Haman et al. [2012], and the ceilometer results have been shown to be consistent with
267 boundary layer heights from Weather Research Forecasting (WRF) modeling [Washenfelder et
268 al., 2011]. To track the origins of the air masses sampled at the ground site, a modified version of
269 the FLEXPART Lagrangian particle dispersion model [Stohl et al., 2005] was used to calculate

270 back trajectories of air masses based on advection and turbulent mixing processes. The main
271 modification consists of using time-averaged winds from the WRF (version 3.3) meteorology
272 model instead of instantaneous winds to improve uncertainties within the FLEXPART model
273 [Brioude *et al.*, 2012]. The WRF output has a spatial grid of 4 km x 4 km, with a temporal
274 resolution of 30 min and 60 vertical levels. Lastly, all linear regressions in this paper are
275 performed as orthogonal distance regressions using Igor Pro 6.2.1 software.

276 **3. Results and discussion**

277 **3.1. Total submicron aerosol composition at the Pasadena ground site during CalNex**

278 While the focus of this paper is OA, a survey of the total aerosol composition can provide
279 valuable context for the OA analysis, and providing such a context is the goal of this section
280 (3.1). (Note: Comparisons with previous campaigns as well as additional figures regarding the
281 total submicron aerosol composition are shown in Section B of the Supporting Material.) The
282 time series for the nrPM₁ species and EC are shown in Figure 1B. In addition, the diurnal cycles
283 of the nrPM₁ species and EC are shown in Figure 2A. The time series for metals, mineral dust,
284 and refractory chloride (rCl) are shown in Figure 1C, and for comparison the PALMS particle
285 type time series are included in Figure 1 as well (Panels D and E). The fractional composition of
286 the total submicron mass is determined by combining the AMS, Sunset Analyzer, XRF, and
287 PALMS measurements, and is summarized in Figure 2C. (Note: see the Figure 2 caption for
288 details regarding which instrument measured each species as well as how the PALMS data is
289 converted to mass concentration.) In the interpretation of the data in Figures 1 and 2 it is
290 important to consider some differences in size cuts of the measurements. First, the XRF
291 measurements used in Figures 1 and 2 correspond to a size cut of 1150 nm aerodynamic

292 diameter. By linearly interpolating the size-resolved XRF measurements the average
293 overestimate relative to the actual PM_{10} concentrations was found to be approximately 30%.
294 Second, the online Sunset OC/EC analyzer was equipped with a $PM_{2.5}$ cyclone for most of the
295 campaign. From 6/12 through 6/16 the EC measurement was performed while switching between
296 a $PM_{2.5}$ and PM_{10} cyclone, and the ratio of the PM_{10} EC to the linearly interpolated $PM_{2.5}$ EC was
297 0.93 (± 0.19 standard deviation). Thus, while the EC data in Figures 1 and 2 may overestimate the
298 true PM_{10} EC concentrations, it is expected that this error will be reasonably small ($\sim 7\%$). Despite
299 these overestimates of refractory mass, the total PM_{10} concentration is still dominated by non-
300 refractory species (OA + sulfate + nitrate + ammonium + nrCl) that account for 93% of the
301 measured mass. Similarly, particle types measured by the PALMS instrument that are
302 predominately composed of non-refractory material comprised 90% of submicron aerosol
303 volume (Figure 3).

304 A clear diurnal cycle is observed for most nr PM_{10} species. As shown in Figure 2, the
305 maxima in the EC and CO (commonly used combustion emission tracers) diurnal cycles are both
306 observed between 12:00 and 13:00 PDT (local time). These maxima do not coincide with the Los
307 Angeles County morning rush hour, which occurs between about 06:00 and 08:00 PDT
308 [Caltrans, 2010]. Instead, they appear to result from polluted air masses initially emitted in the
309 source-rich regions west and south of Pasadena. The wind speed and wind direction measured at
310 the ground site are consistent with the transport of this plume to Pasadena over several hours. In
311 addition, FLEXPART back-trajectories show that the air masses over the Pasadena ground site
312 when EC and CO concentrations are highest have significant footprint residence times over
313 downtown LA as well as the Ports of LA and Long Beach, which are regions with significant
314 combustion emissions.

315 Compared to EC and CO, the OA concentrations peak later in the day, about 3 pm, which
316 corresponds to the same time-of-day when air masses over the Pasadena ground site were the
317 most photochemically processed (Figure 2B). The photochemical age for the air mass over the
318 Pasadena site was calculated with two different methods. First, using the ratio of 1,2,4-
319 trimethylbenzene to benzene, as described in Parrish et al. [2007]. Second, by defining the
320 photochemical age as $-\log_{10}(\text{NO}_x/\text{NO}_y)$ similar to Kleinman et al. [2008]. All photochemical
321 ages were calculated using a standard OH radical concentration of 1.5×10^6 molecules cm^{-3} . For
322 reference, the daily OH radical concentrations averaged for the whole campaign at the Pasadena
323 site was 1.3×10^6 molecules cm^{-3} . Interestingly, when using the NO_x/NO_y method, the
324 photochemical age slowly increases from 00:00 – 06:00 local time, likely due to N_2O_5 and
325 ClNO_2 formation, which are NO_x sinks [Chang et al., 2011]. Outside of this time range however,
326 the diurnal cycles of the two photochemical age estimates show good agreement.

327 The diurnal cycle for OA is relatively flat and low during the early morning hours, 00:00
328 to 06:00, suggesting a small role for nighttime chemistry driven by either NO_3 radicals or
329 aqueous chemistry (RH peaked during this time of day). The lack of aqueous chemistry may be
330 driven by the low oxidant concentrations at night. In parallel work, X Zhang et al. [2012] showed
331 that for Pasadena the aerosol water was not an important absorbing phase, and instead the
332 partitioning coefficient for organics was correlated with OA mass. This result suggests that semi-
333 volatile organic compounds are primarily partitioning to the organic phase.

334 The submicron nitrate diurnal cycle is different from OA with a peak in the morning. The
335 afternoon decrease in nitrate can be attributed to both vertical dilution due to the increase in
336 boundary layer height as well as the higher temperatures and lower RH values that favor
337 evaporation of ammonium nitrate [Neuman et al., 2003]. In Pasadena both nitric acid and

338 ammonia exhibit peaks around noon and elevated concentrations in the afternoon, which is
339 consistent with volatilization of ammonium nitrate [Veres *et al.*, 2011; Ellis *et al.*, Manuscript in
340 Preparation, 2012]. The diurnal cycle of sulfate is not influenced by temperature because
341 ammonium sulfate is non-volatile at atmospheric temperatures, and the sulfate maximum is
342 observed in the afternoon, which may be due to advection to the ground site from sources west
343 and south of Pasadena and/or photochemical production of sulfate.

344 In addition to the diurnal cycles, substantial multi-day variability is evident in Figure 1.
345 In particular, from June 2nd through June 6th there appears to be a high pollution episode where a
346 steady increase in organic aerosol concentrations occurs that is most evident during the nighttime
347 and morning hours. A similar, second high pollution episode is observed at the end of the
348 campaign (June 13th – June 16th). These episodes were likely the result of synoptic conditions
349 that trapped pollution in the LA Basin overnight in the boundary layer and in residual layers aloft
350 that tend to contain more aged air [Lu *et al.*, 1995]. Recirculation of pollution in the LA Basin
351 has been recognized for several decades [e.g. Blumenthal *et al.*, 1978; Moore *et al.*, 1991;
352 Ulrickson *et al.*, 1990]. Additionally, a distinct period of greater marine influence is observed
353 between May 20th and 25th. The highest concentrations of rCl are observed during this period, as
354 well as a prominent rCl diurnal cycle (Figure 1C). Dimethyl sulfoxide concentrations, a well-
355 known indicator of marine influence, are also elevated during this period and exhibit a similar
356 diurnal pattern (data not shown).

357 The PALMS single-particle instrument provides important complementary information
358 regarding aerosol composition at the Pasadena ground site. In particular, the PALMS is capable
359 of characterizing refractory and super-micron aerosols that cannot be measured using the AMS.
360 As stated in the first sentence of this section the focus of this paper is OA, but a survey of the

361 total aerosol composition can provide valuable context for the OA analysis, hence the inclusion
362 of the PALMS results here. The volume concentration time series for particle composition types
363 identified by the PALMS single-particle instrument are shown in Figures 1D and 1E. In addition,
364 the campaign average volume concentrations are summarized in the pie charts shown in Figures
365 3A and 3B. The particle composition types were identified from PALMS mass spectra following
366 the method described in Froyd et al. [2009]. For instance, biomass burning spectra are identified
367 by a prominent K^+ peak along with organic peaks and a lack of other metals. Vanadium with
368 organic species was used as a tracer to identify aerosol from heavy oil combustion (e.g. from
369 ship engines), which allows for the definition of a particle class termed ‘Oil Combustion’ similar
370 to previous work with other single-particle instruments that studied emissions from commercial
371 ports [Ault et al., 2009; Healy et al., 2009]. Since the PALMS is a single-particle instrument, it is
372 capable of determining aerosol mixing state. One consideration when comparing the PALMS
373 results against the AMS and other measurements is that the classification of particles typically
374 follows the most abundant components in a particle, but the PALMS volume concentration for
375 each particle type also includes secondary material on the particle that may even dominate the
376 particle volume at the time of detection. For the Pasadena ground site it was observed that all the
377 particle types contained substantial amounts of nitrate, sulfate, and organics, which indicates that
378 either condensation of secondary material is occurring on primary aerosols (e.g., sea salt and
379 mineral dust) and/or particle mixing is occurring through coagulation. The nitrate observed on
380 sea salt particles is also at least partially due to the heterogeneous reaction between sea salt and
381 nitric acid as discussed in the Appendix. An important conclusion that can be made from the data
382 in Figure 3 is that the PM_{10} aerosol volume concentration is dominated by sulfate/OA/nitrate type
383 particles, and the super-micron aerosol is dominated by sea salt particles. These findings are

384 generally consistent with the mass concentration data from XRF and AMS measurements. The
385 PALMS biomass burning results are discussed further in section 3.2.3.

386 **3.2. Source apportionment of organic aerosol mass by positive matrix factorization**

387 **3.2.1. Mass spectra, time series, and diurnal cycles of the organic aerosol components**

388 The OA components from the PMF analysis were identified by their mass spectra, diurnal
389 cycles, and elemental composition, as well as by the concentration ratios and correlations of their
390 time series with tracers. Figure 4 shows the mass spectra and time series for the five identified
391 components. Additionally, Figure 5 shows the diurnal profiles of the OA components and the
392 campaign-average fractional contribution of each component to the total OA concentration, as
393 well as a stacked plot illustrating the fractional contributions to OA mass by time-of-day. A
394 summary of correlations between the OA components and various tracers is provided in Section
395 D of the Supporting Material. The five PMF components identified are: (1) Hydrocarbon-like
396 Organic Aerosol (HOA), (2) Cooking-Influenced Organic Aerosol (CIOA), (3) Local Organic
397 Aerosol (LOA), (4) Semi-Volatile Oxygenated Organic Aerosol (SV-OOA), and (5) Low-
398 Volatility Oxygenated Organic Aerosol (LV-OOA). The naming based on volatility is adopted
399 according to several studies showing a relationship between high oxygenation and lower
400 volatility for the OOA components [e.g. *Cappa et al.*, 2010; *Huffman et al.*, 2009; *Jimenez et al.*,
401 2009; *Lanz et al.*, 2007; *Ulbrich et al.*, 2009]. The HOA component has been previously
402 described as a surrogate for primary combustion OA, and the SV-OOA and LV-OOA
403 components as surrogates for ‘fresher’ and ‘aged’ SOA, respectively. [*Aiken et al.*, 2008;
404 *Jimenez et al.*, 2009; *Ulbrich et al.*, 2009; *Q Zhang et al.*, 2007b]. The identification of CIOA is
405 consistent with previous research that has shown food cooking, which includes activities such as

406 seed oil frying and meat charbroiling, is an important source of fine organic aerosol in urban
407 environments [e.g. *Mohr et al.*, 2011; *Schauer et al.*, 2002b]. The precise source (or sources) of
408 the LOA component is not known, however similar, highly variable, nitrogen-rich components
409 have been identified in Mexico City [*Aiken et al.*, 2009], Riverside, CA [*Docherty et al.*, 2011],
410 Crete [*Hildebrandt et al.*, 2011], and New York City [*Sun et al.*, 2011]. This component is
411 termed ‘local organic aerosol’ because the LOA time series exhibits high-frequency fluctuations
412 that indicate a relatively local source for this component. (Auto-correlation plots of the
413 component time series are shown in Figure D-7 of the Supporting Material.) The LOA mass
414 represents only a small portion of the total OA mass (5%). Still, the reoccurrence of LOA in
415 different urban areas is an interesting finding. Additional details regarding how the PMF solution
416 was selected are provided in Section D of the Supporting Material.

417 The mass spectra and elemental ratios of the five components displayed in Figure 4A are
418 similar to those reported in previous studies [e.g. *Aiken et al.*, 2009; *Hersey et al.*, 2011; *Mohr et*
419 *al.*, 2011]. For HOA, O:C is relatively high (0.14), but not out of the range of previously reported
420 values. For instance, O:C values as low as 0.02 (Riverside, CA) and 0.03 (Barcelona) [*Docherty*
421 *et al.*, 2011; *Mohr et al.*, 2011] and as high as 0.16 (Mexico City) and 0.17 (Beijing) have been
422 reported for HOA components [*Aiken et al.*, 2009; *Huang et al.*, 2010]. The diurnal cycle of
423 HOA is similar to that of EC (and rBC) with a peak between 13:00 and 14:00 PDT (local time),
424 and HOA and EC (and rBC) show high correlation (See Table D-1 in the Supporting Material,
425 and Section 3.3 below). Therefore, as discussed in Section 3.1 for other primary emissions, it
426 appears that a large portion of the HOA is transported to Pasadena over a period of several hours
427 from the west and south, which is consistent with the relatively high HOA oxidation. Evidence
428 that HOA is dominated by primary sources is given in Section 3.4.1. In addition, the Van

429 Krevelen diagram analysis described in the next section indicates that the types of oxygen-
430 containing functional groups in HOA are different from OOA (on average), which suggests a
431 different oxidation pathway(s). A possible cause for the oxygen content in HOA is therefore
432 heterogeneous oxidation, although other causes including primary emission of oxygenates cannot
433 be conclusively ruled out using the results reported here. The CIOA component is more
434 oxygenated than HOA, which is consistent with previous reports and the known presence of
435 oxygenated compounds such as fatty acids and cholesterol in food cooking aerosol [*Mohr et al.*,
436 2011; *Robinson et al.*, 2006; *Sun et al.*, 2011]. The HOA and CIOA spectra are compared in
437 detail in Section D of the Supporting Material. The diurnal cycle of CIOA exhibits peaks near
438 mealtimes with a smaller peak between 14:00 and 15:00 PDT and a larger peak between 21:00
439 and 22:00 PDT similar to the cooking organic aerosol diurnal cycles observed for other field
440 measurements [*Allan et al.*, 2010; *Crippa et al.*, 2013; *Mohr et al.*, 2011; *Sun et al.*, 2011]. The
441 lunchtime and the dinnertime peaks are both slightly delayed from traditional American
442 mealtimes. The delays could be due to transport time from areas south and west of Pasadena. The
443 delay in the dinner time peak may also be the result of the convolution of the emission rates with
444 the lower boundary layer in the evenings and thus reduced vertical dilution of CIOA.

445 Both SV-OOA and LV-OOA display higher O:C compared to the other OA components
446 for Pasadena, and LV-OOA is the most oxygenated as expected for more aged SOA. The SV-
447 OOA and LV-OOA O:C values (0.38 and 0.8, respectively) are similar to those measured at
448 Barcelona (0.32 & 0.75), New York City (0.38 & 0.68), and Riverside (0.29 & 0.72) [*Docherty*
449 *et al.*, 2011; *Mohr et al.*, 2011; *Sun et al.*, 2011], and are consistent with the range of O:C values
450 for OOA reported by Ng et al. [2011]. The diurnal cycle of SV-OOA is very strong and peaks in
451 the afternoon. This pattern is likely due to photochemical age peaking at a similar time compared

452 to when SOA precursors emitted during the morning rush hour arrive in Pasadena (along with
453 EC and CO). The temporal variability of SV-OOA therefore indicates this component is closely
454 linked to in-basin photochemical production of SOA, as has been seen in other studies [*Aiken et*
455 *al.*, 2009]. In contrast, LV-OOA does not show a strong diurnal variation on average, but the
456 LV-OOA time series does vary substantially during the campaign measurement period. In
457 particular, there is an increasing trend in LV-OOA concentrations during the June 2nd – June 6th
458 period when there is evidence for recirculation of polluted air within the South Coast Air Basin
459 impacting aerosol concentrations. A build-up of LV-OOA concentrations during this period is
460 consistent with describing this component as ‘aged’, since the OA is expected to be increasingly
461 oxidized during periods of recirculation.

462 The mass spectrum of LOA is distinct from the other OA components and contains
463 prominent ions that are characteristic of amines: CH_4N^+ (m/z 30), $\text{C}_2\text{H}_4\text{N}^+$ (m/z 42), $\text{C}_3\text{H}_6\text{N}^+$ (m/z
464 56), $\text{C}_3\text{H}_8\text{N}^+$ (m/z 58), $\text{C}_5\text{H}_{10}\text{N}^+$ (m/z 84), $\text{C}_5\text{H}_{12}\text{N}^+$ (m/z 86) [*McLafferty et al.*, 1993]. The large
465 contribution of nitrogen to this factor (N:C = 0.05) is explained by the substantial presence of
466 these ions. The contribution of LOA to the total mass for each listed amine fragment ranges from
467 4% for CH_4N^+ to 89% for $\text{C}_5\text{H}_{12}\text{N}^+$. In total, the LOA component accounts for 34% of the
468 measured amine mass, and the contributions from the other PMF components are 31% (LV-
469 OOA), 15% (HOA), 13% (SV-OOA), and 8% (CIOA). As discussed in Section D of the
470 Supporting Material, the correlations of LOA with other measured species (e.g. VOCs and
471 metals) suggest that LOA sources are related to industrial processes, especially paint application,
472 but the results are not conclusive.

473 Shown in Figure 5C are the diurnal profiles for the total OA elemental ratios (O:C and
474 H:C). The diurnal trend in the elemental ratios is mostly consistent with the trends in the OA

475 components determined from the PMF analysis. In the early morning hours, the O:C ratio is the
476 highest, which suggests the presence of highly aged, likely secondary, aerosol. Indeed, during
477 this period LV-OOA is the dominant OA component. In the afternoon (~14:00), there is a strong
478 decrease in O:C, which can be attributed to the arrival of POA at the Pasadena ground site and/or
479 the formation of fresh secondary organic aerosol. In the evening (~21:30) there is second
480 minimum in the O:C, but this occurs during a period of low photochemical age (Figure 2), which
481 implies that the ground site is impacted at this time by POA. As seen in Figure 5, this evening
482 O:C minimum matches the peak in CIOA, a primary OA component with relatively low oxygen
483 content. An interesting difference between the PMF and elemental ratio diurnal trends is the peak
484 in H:C that is observed in the morning (~08:00) and is likely due to primary emissions from the
485 local morning rush hour. This peak is three to four times smaller than the H:C peaks for the
486 afternoon and evening events also associated with POA however, indicating a very weak
487 influence from the local rush hour. The PMF analysis is not expected to resolve components that
488 are less than approximately 5% of the OA mass [Ulbrich *et al.*, 2009], and therefore, the absence
489 of this weak local contribution in the PMF results is not surprising.

490 From Figure 5D, if total OOA is taken as a surrogate for SOA, and the sum of HOA,
491 CIOA, and LOA is taken as a surrogate for POA, then it can be concluded that SOA is dominant
492 at the Pasadena ground site, which is consistent with earlier findings in Riverside, CA [Docherty
493 *et al.*, 2008]. On average the total OA mass for the measurement period is composed of 66%
494 OOA (SV-OOA + LV-OOA), and this percentage lies between that observed for a selection of
495 ‘urban’ and ‘urban downwind’ sites [Q Zhang *et al.*, 2007b]. This percentage is also similar to
496 previous results from measurements based in Pasadena. In particular, Hersey *et al.* [2011]
497 reported that during the PACO campaign in May/June 2009 77% of OA was classified as OOA,

498 and Turpin et al. [1991] reported that during the summer of 1984 SOA contributed roughly half
499 of the OA mass. In contrast, there is a wide range of SOA to OA ratios reported for areas east of
500 Pasadena over the past several decades (~20 – 70%) [*Docherty et al.*, 2008 and references
501 therein].

502 **3.2.2. The atmospheric evolution of H:C versus O:C and the elemental ratios of the organic** 503 **aerosol components**

504 To relate the elemental composition of the OA components to each other as well as to the
505 bulk OA the H:C and O:C values from the combined AMS/PMF analysis are plotted in a Van
506 Krevelen diagram (Figure 6). Within a Van Krevelen diagram more oxidized organic compounds
507 lie at the lower right, and different oxidation reactions fall along individual straight lines. For
508 instance, oxidation of a methylene group ($-\text{CH}_2-$) to a carbonyl group ($-\text{C}(=\text{O})-$) corresponds to
509 a slope of -2 , and oxidation of a methylene group to an alcohol group ($-\text{C}(\text{OH})-$) corresponds
510 to a slope of zero. Other reactions or combinations of reactions relevant to OA may lead to a
511 variety of slopes in the Van Krevelen diagram as well, which makes attributing a particular slope
512 to a specific chemical reaction difficult in the case of ambient field measurements. Despite this
513 complexity the Van Krevelen diagram is still useful for constraining the reactions that are
514 responsible for the aging of OA, including for SOA models and their comparison to
515 measurements [e.g., *Murphy et al.*, 2011].

516 Elemental ratios have been reported previously for the SOAR-1 campaign in Riverside,
517 California [*Heald et al.*, 2010], and these data are included in Figure 6 as well. The slope of the
518 Van Krevelen diagram for bulk OA is different when comparing the data from Pasadena and
519 Riverside. The regression analysis for Pasadena results in a best-fit slope of -0.64 whereas a

520 slope of -1.1 is obtained for Riverside. However, when the OOA factors are analyzed alone they
521 correspond to a line with a slope of -0.55 similar to other field measurements [Ng *et al.*, 2011],
522 which is consistent with methylene fragmentation reactions leading to carboxylic acids.

523 Given that the composition and chemical evolution of OOA in Pasadena and Riverside
524 are similar within this analysis, the differences in the slopes for bulk OA in the Van Krevelen
525 diagram cannot be explained by changes in SOA oxidation chemistry. The composition of the
526 HOA measured at the two locations is dissimilar, however. The HOA in Riverside exhibits a
527 very low O:C ratio (0.02), while in Pasadena HOA is more oxidized ($O:C = 0.14$). Thus, it is
528 proposed that the different slope for Riverside is due to the atmospheric mixing of fresh HOA-
529 rich particles into the air mass above the site. In Riverside, the addition of less oxidized HOA to
530 the air mass results in the steep slope observed in that location. Contrastingly, in Pasadena the
531 more oxidized HOA does not influence the slope strongly when mixing occurs because the
532 Pasadena HOA falls near the line defined by the OOA components in the Van Krevelen diagram.

533 Based on the diurnal cycles of HOA for the two sites, it seems that that the Pasadena
534 HOA is more oxidized because it has undergone more photochemical aging relative to the
535 Riverside HOA. In Riverside, the HOA concentration peaks in the morning as expected for fresh
536 emissions from the local morning rush hour traffic [Docherty *et al.*, 2011], consistent with the
537 location of the Riverside site downwind and nearby large highways. In Pasadena the HOA
538 concentration peaks around 13:30, however, due to advection over several hours from the west
539 and south. We note that the major combustion tracers follow similar diurnal trends for the two
540 sites.

541 It was also observed by Ng et al. [2011] that HOA components occupy a different space
542 of the Van Krevelen diagram relative to OOA and display variability that can be approximated
543 by a line with a -2 slope. The HOA components for Riverside and Pasadena shown in the Van
544 Krevelen diagram presented here follow a similar line, which is indicative of HOA aging. As
545 described already, a slope of -2 is consistent with functionalization of a methylene chain with
546 carbonyls. For Pasadena, the HOA component also correlated with several ketones (see 2DTAG
547 data discussed in Section D of the Supporting Material), which provides further evidence that
548 carbonyl groups may be an important oxygen-containing functional group for HOA.

549 **3.2.3. Constraints on the biomass burning contribution to the organic aerosol mass**

550 An apparent discrepancy between the combined AMS/PMF analysis and the PALMS
551 measurements is that the latter classified 12% of the PM_1 aerosol volume as biomass burning, but
552 the AMS does not show a significant amount of biomass burning influence as indicated by the
553 ratio of the organic mass at m/z 60 to total organic mass (f_{60}) [Cubison et al., 2011]. (Note: the
554 possible contribution of organic acids to f_{60} is accounted for by simultaneously analyzing f_{44} in an
555 f_{44} vs. f_{60} plot as described previously by Cubison et al.) Also, a Biomass Burning Organic
556 Aerosol (BBOA) component is not identified in the PMF analysis, in which OA components
557 accounting for about 5% or more of the OA mass are expected to be resolved [Ulbrich et al.,
558 2009]. Acetonitrile, a tracer for biomass burning, is generally near background concentrations
559 (100 – 150 pptv) except for several high concentration events that are short in duration that do
560 not correlate with the PALMS biomass burning particles, and could be related to nearby solvent
561 use (e.g. in the Caltech campus). It is possible that potassium-containing particles from sources
562 other than biomass burning such as meat cooking [Hildemann et al., 1991; Schauer et al., 1999],
563 which can represent a substantial fraction of the potassium in some urban regions [Aiken et al.,

2010; X Zhang *et al.*, 2010], may be classified as biomass burning by the PALMS algorithm due to the presence of potassium and abundant organic species. If cooking activities were the dominant source of the PALMS biomass burning particles however, then the PALMS biomass burning volume concentration would be expected to correlate with the CIOA mass concentration, which is not the case ($R = -0.03$). An alternative explanation is that the primary biomass burning mass is small, and there is a large amount of secondary mass that has condensed on the biomass burning particles. (Similarly, the primary biomass burning particles may have coagulated with secondary aerosol particles.) The particles would then be classified as biomass burning by the PALMS algorithm, but their measured volume would be significantly increased by secondary material (e.g. SOA, nitrate, sulfate, and ammonium). Finally, it is also possible that the biomass burning particles are very aged as the result of long-range transport, and due to aging they are difficult to identify with the AMS biomass burning tracers or PMF [Cubison *et al.*, 2011]. When the observations described in this paragraph are evaluated together, then the best explanation for the discrepancy is that while 12% of submicron particles (by volume) contained some biomass burning material, the overall mass of these particles at the Pasadena ground site was dominated by condensation or particle coagulation of non-biomass burning material. Based on the limit of AMS/PMF analysis to resolve small fractions of OA, we estimate that primary biomass burning material contributed <5% to submicron aerosol mass during the study.

3.3. Evaluation of primary organic aerosol emission ratios with EC and CO

The HOA concentration correlates strongly with EC determined from the online Sunset analyzer ($R=0.71$), and the ratio of HOA to EC can provide valuable insight regarding the source of this OA component. To explore this correlation further a scatter plot of HOA versus EC mass concentration data is plotted in Figure 7A. The data points in the plot are colored with the

587 corresponding NO_y to ΔCO ratios. Periods with higher diesel influence are expected to exhibit
588 higher $(\text{NO}_y/\Delta\text{CO})$ [Ban-Weiss *et al.*, 2008a; Parrish *et al.*, 2007]. The ratio is not corrected for
589 dry deposition losses of nitric acid though, and thus it cannot be treated as a quantitative metric.
590 In addition, the grey shaded areas in Figure 7A indicate the range of POA to EC emission ratios
591 for gasoline and diesel vehicles that were measured during summer 2006 at the Caldecott Tunnel
592 in California [Ban-Weiss *et al.*, 2008b]. The HOA to EC ratios at the Pasadena ground site
593 overlap the range of POA to EC ratios from the Caldecott Tunnel. A linear regression analysis of
594 the Pasadena data yields a line with a slope of 1.82, which is close to the upper limit of the POA
595 to EC ratios reported in the tunnel study. The Pasadena ratio is at times higher, but this
596 difference could be due to changes in the emission ratios of vehicles between 2006 and 2010, or
597 the larger influence of cold starts for our dataset versus warm-running vehicles for the Caldecott
598 Tunnel. In Pasadena, for periods more influenced by diesel emissions, as indicated by high
599 $(\text{NO}_y/\Delta\text{CO})$, generally lower HOA to EC ratios are observed. Specifically, the best-fit slope is
600 1.51 for $(\text{NO}_y/\Delta\text{CO}) > 0.124$, which corresponds to the highest 10th percentile of $(\text{NO}_y/\Delta\text{CO})$
601 values. This finding is consistent with the emission ratios reported by Ban-Weiss *et al.* [2008b],
602 and suggests that both diesel and gasoline vehicle emissions are contributing to the HOA mass.

603 A correlation between HOA and CO is also observed ($R = 0.59$). A stronger correlation is
604 observed between CO and the sum of HOA and CIOA ($R = 0.71$) however. Shown in Figure 7B
605 is a scatter plot of the CO and the HOA+CIOA data. The improved correlation when the CIOA
606 mass concentration is added to the HOA mass concentration is surprising because cooking is not
607 considered a major source of carbon monoxide, although it is a significant source of organic
608 aerosol [Allan *et al.*, 2010; CARB, 2008; Harley *et al.*, 1997]. Emissions of CO have been
609 measured from certain cooking activities [Lee *et al.*, 2001], but it is still a possibility that the

610 CIOA component contains particulate mass from non-cooking sources that also emit CO (e.g.
611 gasoline vehicles). Therefore, it is most reasonable to characterize this component as ‘cooking-
612 influenced’, but not purely from cooking sources. It should be noted that different PMF solution
613 rotations were explored using the FPeak parameter as discussed in the Supporting Material.
614 There are rotations that exhibit lower correlations between CIOA and CO, but HOA+CIOA
615 always displays a higher correlation than HOA with CO (within the constraint of not
616 substantially diminishing the correlation between HOA and rBC). In addition, these alternative
617 solutions exhibit lower correlations between HOA and rBC, as well as between HOA+CIOA and
618 CO.

619 The data in Figure 7B are also colored by the relative amount of CIOA, so that the ratios
620 of HOA to CO and CIOA to CO can be at least partially resolved. For periods when HOA
621 concentrations are high (i.e. greater than 90% of the sum of HOA and CIOA) the correlation with
622 CO is very strong ($R = 0.9$) and the linear slope is $6.4 \mu\text{g m}^{-3} \text{ppmv}^{-1}$ when using a CO
623 background (x-intercept) of 105 ppbv, which is comparable to slopes found in previous studies
624 [Aiken *et al.*, 2009]. In contrast, for periods when CIOA concentrations are high the linear slope
625 is $13 \mu\text{g m}^{-3} \text{ppmv}^{-1}$, more than twice that for HOA. The steeper slope for CIOA is indicative of
626 significant cooking sources for CIOA that, as stated earlier, produce a larger amount of organic
627 aerosol relative to CO [McDonald *et al.*, 2003]. A lower limit on the relative amount of CIOA
628 mass from cooking sources can be estimated using the observation that the linear regression
629 slope of CIOA is about twice that of HOA when the mass concentrations are plotted versus CO.
630 Assuming that CO is overwhelmingly from vehicle emissions and no CO is emitted from
631 cooking sources then CIOA would be 50% from cooking sources *on average* with the remainder
632 from vehicle emissions (i.e. the additional cooking organic aerosol mass would double the mass

633 concentration versus CO slope relative to HOA). This percentage is a lower limit because some
634 CO could be co-emitted with cooking organic aerosol, for instance from burning of charcoal
635 [Bhattacharya *et al.*, 2002], and that would raise the percentage of CIOA from cooking above
636 50%. This approach is a simplistic approximation, but the lower limit appears to be reasonable
637 given that the diurnal cycles and spectral characteristics of CIOA are consistent with previous
638 studies. In addition, comparison of the CIOA concentration against that predicted from the
639 amount of organic mass measured by the AMS at m/z 55 following Mohr *et al.* [2011] indicates
640 that approximately 75% of CIOA is from cooking sources (See Section D of the Supporting
641 Material for the details of this comparison). A higher percentage up to almost 100% is also
642 possible given the uncertainties in the comparison.

643 An alternative approach for analyzing the correlation with CO is to use a multi-linear
644 regression instead of filtering the data for periods of high HOA or CIOA influence. For
645 completeness, a multi-linear regression was performed where HOA and CIOA were the
646 independent variables and CO was the dependent variable. Emission ratios of 8.0 and 16 $\mu\text{g m}^{-3}$
647 ppmv^{-1} were obtained for HOA and CIOA, respectively (using 105 ppbv background CO as
648 above). This result is similar to that described in the preceding paragraph, which indicates both
649 approaches for treating the data are robust.

650 **3.4. The quantitative dependence of secondary organic aerosol concentration on** 651 **photochemical oxidation**

652 **3.4.1. Increases in the organic aerosol to ΔCO ratio with photochemical age**

653 To evaluate if the timescales and efficiency of SOA formation observed in Pasadena are
654 similar to other urban regions the evolution of (OA/ ΔCO) as a function of photochemical age is

655 plotted in Figure 8, where ΔCO is the CO concentration enhancement over its background
656 concentration. The background CO is estimated to be between 85 – 125 ppbv using CO
657 measurements taken aboard the NOAA WP-3D aircraft off the LA coastline at altitudes less than
658 200 m (Latitude range: 32 to 35, Longitude range: -117 to -120). A concentration of 102 ppbv
659 was the minimum observed and concentrations below 110 ppbv were regularly observed.
660 Accordingly, the background CO was taken to be 105 ppb when calculating $(\text{OA}/\Delta\text{CO})$, and the
661 error bars in Figure 8 represent the variability in the data if the background CO is taken to be
662 either 85 or 125 ppb. Given the observed CO values off the LA coastline this range represents a
663 conservative estimate of the uncertainty in background CO. The CO enhancement is assumed to
664 be a conservative tracer of urban combustion emissions that are also a source of aerosols and
665 aerosol precursors, and thus, normalizing the OA concentration to CO will remove the effect of
666 dilution. Photochemical formation of CO from VOCs or destruction of CO by OH reactions were
667 estimated to perturb CO concentrations minimally over these time and spatial scales [Griffin *et*
668 *al.*, 2007].

669 The grey region in Figure 8 represents $(\text{OA}/\Delta\text{CO})$ versus photochemical age observations
670 from previous campaigns in Mexico City and the northeastern United States as summarized by
671 DeCarlo *et al.* [2010]. All the data sets display an increase in the $\text{OA}/\Delta\text{CO}$ ratios with
672 photochemical age due to secondary organic aerosol formation. The Pasadena $\text{OA}/\Delta\text{CO}$ versus
673 photochemical age plot follows the upper limit of the range of previously reported values,
674 although the differences should not be over interpreted given the uncertainties associated with
675 the background CO determination (indicated by the error bars) and the photochemical age
676 calculations. The photochemical age uncertainty has been discussed extensively in previous
677 papers and is due to, in part, the presence of mixed sources with different emission profiles and

678 spatial distributions [e.g. *Kleinman et al.*, 2007; *Parrish et al.*, 2007]. We evaluate this potential
679 source of error in Section E of the supporting material, and use sensitivity studies to determine
680 that photochemical age may be underestimated by approximately 10% in our analysis. This error
681 is in the accuracy rather than the precision, and thus, it does not impact relative comparisons for
682 Pasadena such as the weekday versus Sunday comparison described below. The underestimation
683 may impact comparisons with other campaigns though, and thus it is concluded that SOA
684 production per unit CO in the South Coast Air Basin is not different from other locations given
685 our estimated errors. (In Section E of the supporting material we also demonstrate that OH
686 radical chemistry dominates over Cl radical chemistry in the oxidation of the VOCs used to
687 calculate photochemical age.) The data in Figure 8 suggest that similar precursors are responsible
688 for SOA production in Pasadena, Mexico City, and the northeastern United States, and that the
689 precursors are emitted proportionally to CO. These conditions then imply a relatively constant
690 mix of the important SOA precursor and CO sources across the locations discussed.

691 To understand the similarity in $OA/\Delta CO$ it is important to consider the emission ratios for
692 SOA precursors (e.g., $\Delta VOC/\Delta CO$), especially given the long-term decrease of CO
693 concentrations in the United States [*Parrish et al.*, 2002] that could potentially influence
694 $OA/\Delta CO$ values. The emission ratios of aromatic, alkyne, and alkene VOCs with CO have
695 remained constant between 2002 and 2010, as has the ratio for acetaldehyde [*Warneke et al.*,
696 2012] a species that correlates strongly with OOA ($R=0.81$ in Pasadena) and is dominated by
697 secondary sources after sufficient photochemical processing of emissions. Furthermore, it has
698 been shown that urban VOC emissions at different locations in the US have similar composition
699 and emission ratios with CO (within a factor of 2) [*de Gouw et al.*, 2012; *Warneke et al.*, 2007].
700 The similarity of $OA/\Delta CO$ values described here for different campaigns spanning several years

701 is consistent with the lack of change in $\Delta\text{VOC}/\Delta\text{CO}$ over spatial and temporal scales for the US.
702 However, in Mexico City the $\Delta\text{VOC}/\Delta\text{CO}$ ratios are on average about a factor of 2 higher than in
703 the US [Bon *et al.*, 2011], but the $\text{OA}/\Delta\text{CO}$ values for Mexico City are not substantially higher
704 than in Pasadena or the northeastern US. This observation highlights the possibility that there
705 may be unmeasured organic compounds that are SOA precursors and do not follow the
706 $\Delta\text{VOC}/\Delta\text{CO}$ emission trends discussed above. Lastly, we note that while plotting $\text{OA}/\Delta\text{CO}$
707 versus photochemical age should account for differences in the amount of aging, the average
708 daily OH radical concentrations at the sites were fairly similar where measurements were
709 available: 1.3×10^6 molecules cm^{-3} for Pasadena, 1.5×10^6 molecules cm^{-3} for Mexico City
710 [Hodzic *et al.*, 2011].

711 Marked in Figure 8 is the sum of HOA, CIOA, and background LV-OOA ($\text{LVOOA}_{\text{PCA}=0}$)
712 divided by CO. The ratio of HOA+CIOA to CO is determined from the linear regression analysis
713 of the data in Figure 7B, and the background LV-OOA to CO ratio is the average of LV-OOA
714 divided by CO at photochemical ages less than 0.05 days (Figure 8 inset). Several explanations
715 are possible for the source of background LV-OOA. First, some very aged SOA may be present
716 due to recirculation in the LA basin, for which the photochemical tracers have mostly decayed
717 away. However, the similarity in calculated photochemical ages using either
718 (trimethylbenzene/benzene) or (NO_x/NO_y) suggests that this scenario is not the case, since the
719 high deposition velocity of nitric acid would lead to an observed discrepancy between the two
720 methods at high photochemical ages. A second plausible explanation is ‘dark’ SOA production
721 from ozone or nitrate radicals that will react with alkenes and PAHs. An important piece of
722 evidence to support this possibility would be an increase in $\text{OA}/\Delta\text{CO}$ at low photochemical ages
723 as the time-of-day approached sunrise, since the increase in morning traffic would lead to fresh

724 emissions that decrease photochemical age and react with ozone or nitrate radical to form SOA.
725 This phenomenon is not observed however, which indicates that ‘dark’ SOA is not an important
726 source of the background LV-OOA, consistent with the expected minor contribution of alkenes
727 to SOA in urban areas [Dzepina *et al.*, 2009; Wood *et al.*, 2010].

728 A third explanation is that marine OA may be contributing to the background LV-OOA.
729 However the very low OA concentrations, less than $0.2 \mu\text{g m}^{-3}$, over the open ocean west of
730 California for periods with low pollution influence [P. K. Quinn, NOAA, personal
731 communication, 2012] indicate that this source is less important. In addition, low marine OA
732 concentrations, $0.5 \mu\text{g m}^{-3}$, have been measured by an AMS in La Jolla, CA (located on the
733 California coast 170 km southeast of Pasadena) [Liu *et al.*, 2011], which is an amount similar to
734 other marine studies [Russell *et al.*, 2010], and would only account for a third of the background
735 LV-OOA.

736 The last and most likely explanation for the background LV-OOA is the influence of
737 biogenic sources that emit SOA precursors but relatively small amounts of 1,2,4-
738 trimethylbenzene, benzene, NO_x , and CO [Slowik *et al.*, 2010]. If the air mass above Pasadena
739 was influenced by a biogenic source, an increase in $\text{OA}/\Delta\text{CO}$ would be observed, but the
740 photochemical age as measured by the ratio of (1,2,4-trimethylbenzene/benzene) or (NO_x/NO_y)
741 would not be significantly altered. Back-trajectories for air reaching Pasadena during CalNex
742 often travel over the coastal California mountain ranges where biogenic VOC emissions are large
743 (see Figures A-3 through A-5 in the Supporting Material). Interestingly, at low photochemical
744 ages (less than 0.05 days) there is a general increase in $\text{OA}/\Delta\text{CO}$ with the sum of the
745 concentrations of the two isoprene oxidation products measured by the GC-MS. In particular,
746 when averaging the data into the three bins corresponding to low, medium, and high

747 concentrations of MVK plus methacrolein the binned OA/ Δ CO increases from 21 to 26 $\mu\text{g sm}^{-3}$
748 ppmv^{-1} (standard errors are less than 0.5) from the lowest third to the highest third. This
749 observation indicates biogenic sources are influencing OA/ Δ CO. Furthermore, ^{14}C measurements
750 for selected days during CalNex show that in the early morning hours when LV-OOA is
751 dominant (compared to other OA components and EC) about 50% of total carbon is non-fossil
752 (e.g. from modern sources) [Bahreini *et al.*, 2012]. These results are consistent with biogenic
753 sources influencing the OA/ Δ CO ratio and substantially contributing to background LV-OOA
754 [Zotter *et al.*, Manuscript in Preparation, 2012].

755 In the Figure 8 inset, the organic mass to Δ CO ratio is plotted for each PMF component.
756 The ratio increases for SV-OOA and LV-OOA with photochemical age consistent with both
757 components being dominated by secondary sources. In contrast, the ratios for HOA, CIOA, and
758 LOA do not vary substantially with photochemical age, which strongly supports that these three
759 components are dominated by primary sources. The data in Figure 8 also allow for estimating the
760 amount of background OA (i.e. OA from long range transport). As described above, the
761 concentration of LV-OOA at the lowest photochemical ages should approximately correspond to
762 background OA. Taking LV-OOA/ Δ CO for the lowest age bin in Figure 8 and multiplying it by
763 the Δ CO for this bin yields a background OA concentration of 1.5 $\mu\text{g m}^{-3}$.

764 For HOA heterogeneous oxidation could potentially increase or decrease the magnitude
765 of HOA/ Δ CO through either functionalization or fragmentation reactions, respectively. Given the
766 Van Krevelen diagram analysis described above in Section 3.2.2, fragmentations reactions
767 appear not to be the dominant oxidation pathway. This conclusion is consistent with the recent
768 work of Lambe *et al.* [2012] that showed for larger alkanes the onset of fragmentation occurs at

769 an O:C of about 0.3, which is much higher than the O:C of HOA reported here (0.14). For
770 functionalization reactions, based on the OM:OC ratio of 1.3 for HOA and an estimated OM:OC
771 of 1.2 for an un-oxidized alkane chain, it is calculated that the increase in HOA mass due to
772 oxidation is only 8%, which is smaller than the standard deviation (21%) of the data shown in
773 Figure 8. Condensation of primary semi-volatile organic compounds could also potentially
774 increase HOA/ Δ CO since the averaged OA mass concentration increases with photochemical age
775 from 5 to 15 $\mu\text{g m}^{-3}$ for the binned data shown in Figure 8. However, an increase in HOA/ Δ CO
776 with photochemical age is not observed in Figure 8. This result is consistent with the calculated
777 change in HOA concentrations due to partitioning. Specifically, using the volatility distribution
778 for POA and primary semi-volatile organic compounds reported by Robinson et al. [2007] it is
779 calculated that the increase in HOA concentrations (and HOA/ Δ CO) would be only 28% for an
780 increase of OA from 5 to 15 $\mu\text{g m}^{-3}$. This calculated increase is similar in magnitude to the
781 standard deviation of HOA/ Δ CO, and hence, would be hard to discern. In addition, it is
782 substantially smaller than the increase observed for SV-OOA/ Δ CO (540%) and LV-OOA/ Δ CO
783 (300%). The considerations described in this paragraph also apply to CIOA and LOA but are
784 more difficult to quantify for these components given the lack of literature data (e.g.,
785 fragmentation reaction studies and volatility distributions).

786 **3.4.2. Correlation of oxygenated organic aerosols with the photochemical oxidation marker** 787 **odd-oxygen ($\text{O}_3 + \text{NO}_2$)**

788 Odd-oxygen, O_x , concentrations are closely linked to the extent of photochemical
789 oxidation in an air mass because O_3 production results from OH reactions with VOCs and CO.
790 Therefore, the ratios of OOA to odd-oxygen provide another metric for quantifying the

791 dependence of SOA concentration on photochemical oxidation. Following the work of Herndon
792 et al. [2008] and Wood et al. [2010], we examine the correlations of O_x instead of O_3 to account
793 for the titration of O_3 by fresh NO emissions which produces NO_2 . When comparing the time
794 series of total OOA (SV-OOA + LV-OOA) versus O_x in Figure 9 similar temporal changes are
795 observed ($R^2 = 0.53$), but the correlation is stronger during the more polluted periods of high
796 OOA concentrations that occurred in June ($R^2 = 0.72$ for the June 2nd through 6th high pollution
797 period). It has also been observed that for long-range transported air the correlation vanishes due
798 to differing losses and ongoing chemistry of SOA and O_x [Dunlea et al., 2009]. In Pasadena the
799 regression slope for OOA versus O_x is $0.146(\pm 0.001) \mu\text{g sm}^{-3} \text{ppbv}^{-1}$ (Figure 9 inset). The data in
800 the scatter plot is colored by time-of-day, and interestingly, the slope observed for the morning
801 (06:00 – 12:00 PDT) is steeper than the slope in the afternoon (12:00 – 18:00 PDT):
802 $0.183(\pm 0.004)$ versus $0.163(\pm 0.002) \mu\text{g sm}^{-3} \text{ppbv}^{-1}$. This trend has also been observed in other
803 field measurements [Herndon et al., 2008; Wood et al., 2010], and has been attributed to several
804 factors including increased evaporation of SV-OOA, mixing with air aloft that contains residual
805 OOA and O_x during boundary layer growth, and OOA production occurring on shorter
806 timescales than O_x . The slopes of identical analyses for Riverside, CA and Mexico City are
807 $0.142(\pm 0.004)$ and $0.156(\pm 0.001) \mu\text{g sm}^{-3} \text{ppbv}^{-1}$ [Aiken et al., 2009; Docherty et al., 2011],
808 which are similar to the Pasadena ground site. This agreement indicates that the ratios of the
809 SOA to O_x production rates are remarkably constant for the different sites suggesting similar
810 SOA and O_x formation chemistries on average. As discussed by Wood et al. [2010], changes
811 in the OOA/ O_x ratio would be expected at locations where the relative concentrations of SOA
812 and O_x precursors are different. In Houston for instance, ratios as low as $0.030 \mu\text{g sm}^{-3} \text{ppbv}^{-1}$
813 were found in correlation analyses during periods impacted by large petrochemical plant

814 emissions. This observation was explained by very high concentrations of light alkenes that
815 cause high ozone concentrations but are not expected to contribute greatly to SOA formation.
816 Contrastingly, in Riverside the relative concentrations of SOA and O_x precursors are expected to
817 be similar to Pasadena given that urban VOC emissions have similar composition and emission
818 ratios throughout the US [Warneke *et al.*, 2007] and have not changed over the past several years
819 [Warneke *et al.*, 2012]. In Mexico City, the emission ratios for VOCs (i.e., VOC/CO) are
820 generally higher by a factor of approximately 2 [Bon *et al.*, 2011], which would impact both
821 SOA and O_x production rates proportionally. An important exception is the emission ratios for
822 propane and butane, which were disproportionality high in Mexico City due to liquid petroleum
823 use [Apel *et al.*, 2010]. The contribution of these light VOC compounds was found to be small
824 for O_x production and zero for SOA production, however [Wood *et al.*, 2010]. Similar to the
825 OA/ Δ CO discussion in the preceding section, the consistency in OOA/O_x for multiple field
826 campaigns suggests a relatively constant mix of different O₃ and SOA precursor sources, leading
827 to similar production ratios across multiple urban locations in North America. As also discussed
828 above, the insensitivity of OA/ Δ CO to differences in VOC/CO suggests unmeasured precursors,
829 but if these unidentified species were emitted in proportion to other VOCs, then consistent
830 OOA/O_x values would be expected for the different locations.

831 Chlorine radicals are expected to play a larger role in ozone formation for Pasadena and
832 Riverside in comparison to Mexico City, since the first two locations are near the Pacific Ocean.
833 The contribution of chlorine radical chemistry to the total ozone concentration is a topic of
834 current research [Young *et al.*, 2012]. Still, published work [Knipping *et al.*, 2003] indicates that
835 in Pasadena and Riverside it is relatively small and, as a percentage, less than the 30%
836 uncertainty for AMS measurements [Middlebrook *et al.*, 2012], which is expected to dominate in

837 the OOA/O_x comparison. Thus, the similarity of OOA/O_x between the three locations is
838 consistent with previous work on chloride radical chemistry in the South Coast Air Basin. For
839 reference, average 24 hr OH radical concentrations in Mexico City and Pasadena were 1.3×10^6
840 and 1.5×10^6 molec. cm⁻³, respectively.

841 Meteorological parameters could also influence OOA/O_x in a number of ways including
842 through changes in OOA partitioning with temperature or increases in the importance of aqueous
843 chemistry at high RH. These parameters do not appear to be important for the OOA/O_x analysis
844 presented here, however. The average temperatures and RHs for the different sites with similar
845 OOA/O_x were: 18°C and 83% (Pasadena), 27°C and 53% (Riverside), 16°C and 50% (Mexico
846 City). While higher temperatures in Riverside will favor partitioning of OOA to the vapor phase,
847 the measured volatility of OA for Riverside [Huffman *et al.*, 2009] indicates the amount of
848 evaporation will be small (less than 10%), and thus, will have little effect on OOA/O_x.
849 Additionally, the higher RH in Pasadena relative to Riverside and Mexico City may not
850 influence OOA concentrations given that aerosol water was not an important absorbing phase [X
851 Zhang *et al.*, 2012] as discussed in Section 3.1 above.

852 **3.5. Weekly cycles for organic aerosol components**

853 **3.5.1. Weekly cycles: Primary organic aerosols**

854 It is well-known that in California and the South Coast Air Basin a large decrease in on-
855 road diesel vehicle activity occurs on weekends, which leads to significant reductions in
856 atmospheric species associated with diesel vehicles such as NO_x, EC, specific VOCs, and
857 particulate nitrate [Marr *et al.*, 2002; Millstein *et al.*, 2008; Pollack *et al.*, 2012]. To explore if
858 primary organic aerosols show an analogous weekend effect in Pasadena during CalNex, the

859 diurnal cycles for HOA, EC, rBC, CIOA, CO, and benzene are plotted for weekdays and
860 Sundays separately in Figure 10. Included in the Sunday diurnal cycle is data from the Memorial
861 Day holiday, which occurred on a Monday and exhibited traffic patterns typical of Sundays
862 [Caltrans, 2010]. Thus, the ‘Sunday’ diurnal cycle combines data from six days. Saturday data is
863 not included in Figure 10 to avoid carryover effects from the preceding Friday. Carryover effects
864 on Mondays appear to have little impact on the weekday diurnal cycle with less than a 3%
865 change in the average daily concentrations when Mondays are omitted from averaging and no
866 qualitative change in the diurnal cycles. Thus, Monday data are included with the other weekday
867 data in Figure 10.

868 The EC (and rBC) concentration decreases on Sundays to $71(\pm 6)\%$ of its weekday
869 average and has a very different diurnal cycle. A similar change is observed for HOA, which
870 decreases to $82(\pm 4)\%$ of its weekday average. (Note: uncertainties are the standard errors of the
871 mean.) The decrease in concentrations is consistent with the weekend effect and the importance
872 of diesel vehicle emissions as a source for HOA and EC (and rBC). In contrast, CO
873 concentrations when integrated over the entire day are not substantially different on Sundays
874 versus weekdays, and the average concentration on Sundays is $99.4(\pm 0.3)\%$ of the weekday
875 average. The CO diurnal cycles are dissimilar probably due to changes in traffic patterns.
876 Benzene displays a similar lack of change on Sundays increasing to $105(\pm 3)\%$ of the weekday
877 average. Since gasoline vehicles are an important source of CO and benzene [Fruin *et al.*, 2001;
878 Schauer *et al.*, 2002a], the lack of a weekend effect for these compounds is consistent with
879 previous studies that demonstrated similar overall activity for gasoline vehicles on weekends
880 compared to weekdays [Marr and Harley, 2002; Pollack *et al.*, 2012]. The CIOA concentrations
881 are elevated on Sundays by $161(\pm 4)\%$ displaying a weekly cycle distinctly different from the

882 other species in Figure 10. An increase in barbecuing on weekends has been reported previously
883 for the South Coast Air Basin [*Chinkin et al.*, 2003], which is consistent with elevated CIOA
884 concentrations on weekends. However, given the limited corroborating evidence and lack of
885 previous long term observations of cooking emissions (to our knowledge), further studies are
886 needed to make a confident conclusion regarding the weekly variations in cooking organic
887 aerosol.

888 The observed decreases in HOA and EC concentrations on Sundays can be compared
889 against the expected decreases in their emissions, estimated from a combination of data on fuel
890 sales [*BOE*, 2011], emission ratios [*Ban-Weiss et al.*, 2008b], and traffic volume [*Caltrans*,
891 2010]. The first step to obtain the estimates is calculating the percentage of weekday EC and
892 HOA attributable to diesel emissions using Equation 2 below.

$$893 \quad \frac{EC_{Diesel}}{EC_{Total}} = \frac{ER_{Diesel} \times FS_{Diesel}}{(ER_{Diesel} \times FS_{Diesel}) + (ER_{Gasoline} \times FS_{Gasoline})} \quad (1)$$

894 In Equation 2, *ER* is the emission ratio for diesel and gasoline vehicles taken from Ban-Weiss et
895 al. [2008b], and *FS* is the gasoline and diesel fuel sales reported for the State of California during
896 May and June 2010 [*BOE*, 2011]. An analogous equation is used for HOA. The *ER* is defined as
897 the amount of EC (or HOA) emitted per unit fuel burned, and the values used in this work are:
898 0.022 (gasoline EC), 0.86 (diesel EC), 0.031 (gasoline HOA), 0.41 g kg⁻¹ (diesel HOA). It is
899 assumed that the monthly fuel sales are representative of weekday fuel use in the South Coast
900 Air Basin. Following this method it is estimated that diesel emissions account for 87(±3)% of EC
901 and 70(±10)% of HOA. The second step utilizes daily vehicle miles traveled (VMT) data for Los
902 Angeles County to calculate that during the campaign truck traffic decreased 44% on Sundays
903 relative to weekdays [*Caltrans*, 2010]. This figure lies within the range of other estimates for

904 weekend reductions of heavy-duty vehicle traffic [Chinkin *et al.*, 2003]. Finally, an estimate of
905 EC concentrations on Sunday relative to weekdays, ΔEC_{sun} (%), can be calculated as follows (an
906 analogous equation can be used for HOA).

$$907 \quad \Delta EC_{Sun} = \frac{EC_{Diesel}}{EC_{Total}} \times \frac{(Truck\ VMT)_{Sun}}{(Truck\ VMT)_{WD}} + \frac{EC_{Gas}}{EC_{Total}} \times \frac{(Non-Truck\ VMT)_{Sun}}{(Non-Truck\ VMT)_{WD}} + \frac{EC_{Background}}{EC_{Total}} \quad (2)$$

908 Using Equation 3 the Sunday concentrations of EC and HOA are estimated to be 64(\pm 3)% and
909 72(\pm 6)% of their weekday concentrations, respectively. To estimate these values the non-truck
910 VMT on Sundays versus weekdays was taken to be equal because of the similarity in the average
911 daily CO and benzene concentrations. In addition, the background EC is the average of the
912 values from Langridge *et al.* [2012], 40(\pm 20) ng m⁻³, and the background HOA, 70(\pm 40) ng m⁻³,
913 was calculated from EC using the slope of HOA to EC reported in Figure 7. (Note: The
914 uncertainties for the calculated Sunday reductions in EC and HOA include the uncertainties in
915 the background concentrations reported in Langridge *et al.*) For comparison, the observed
916 average Sunday EC and HOA concentrations at the Pasadena ground site are 71(\pm 6)% and
917 82(\pm 4)% of the weekday averages, respectively. The agreement between the estimated and
918 observed values is good, given the need for several approximations to obtain the estimate. The
919 reduction in HOA is less than the reduction in EC for both the estimated and the observed values,
920 due to the greater portion of HOA emitted from gasoline vehicles. It is noted that in contrast to
921 HOA, the CIOA concentration is higher on Sundays as discussed above, and the combination of
922 the two opposite trends leads to a net increase of POA on the weekends.

923 An important assumption of this analysis is the only sources of EC are on-road diesel and
924 gasoline emissions, as well as the background from long range transport. Transport is the single

925 largest source of EC in the United States, and in the absence of biomass burning it accounts for
926 81% of emitted EC. Within the transport sector EC emissions are dominated by on-road and non-
927 road diesel [EPA, 2012]. Another question is whether commercial marine emissions may have a
928 substantial contribution to the EC budget. To address this consideration we examined the
929 correlation between EC and the oil combustion particles identified by the PALMS instrument,
930 which are presumably from shipping activities. We observed a low correlation ($R^2=0.24$), which
931 is consistent with commercial marine EC emission not substantially impacting the ground site.
932 Ultimately, accounting for only three sources of EC (on-road diesel, on-road gasoline, and a
933 background) is a simplifying assumption, but one that is consistent with emission inventories and
934 other observations. The reasonableness of this assumption is further supported by the closure
935 obtained between the calculated and measured weekly cycles.

936 **3.5.2. Weekly Cycles: Secondary organic aerosols and constraining the importance of diesel** 937 **emissions**

938 To evaluate the weekly cycle for secondary organic aerosols $OA/\Delta CO$ versus
939 photochemical age is plotted in Figure 11A for weekdays and Sundays. Also shown is the
940 analogous plot for total OOA (Figure 11B). The OOA plot is similar for weekdays versus
941 Sundays, and linear regression analyses of the data yield slopes of $108(\pm 5)$ and $98(\pm 8)$ $\mu\text{g sm}^{-3}$
942 ppmv^{-1} for weekdays and Sundays, respectively. (Note: the data fitted are averages resulting
943 from binning the raw data according to photochemical age, and the averages are weighted by the
944 standard errors of the x and y data.) After propagation of error these slopes correspond to a ratio
945 of $1.1(\pm 0.1)$ for weekdays to weekends. Following the estimation method described by Bahreini
946 et al. [2012], and using a 44% decrease in diesel traffic on Sundays as determined above, this
947 ratio corresponds to diesel emissions accounting for $19(+17/-21)\%$ of the OOA mass. Also, a

948 consistently higher photochemical age is observed on Sunday versus weekdays due to the higher
949 oxidant concentrations resulting from reduced NO_x emissions. These results are in good
950 agreement with other CalNex papers that address weekday/weekend effects [Bahreini *et al.*,
951 2012; Pollack *et al.*, 2012]. In particular, they are consistent with the conclusion reported by
952 Bahreini *et al.* [2012] that gasoline emissions are substantially more important than diesel
953 emissions in the formation of secondary organic aerosol mass within the LA Basin, since a large
954 decrease in the OOA/ Δ CO ratio is not observed on weekends when there is less diesel traffic. It
955 should be noted as well that the results present here are better constrained than the Bahreini *et al.*
956 analysis because the PMF results are used to obtain OOA/ Δ CO rather than relying on estimated
957 values of POA/ Δ CO to calculate OOA/ Δ CO, and because of the more precise binning by
958 photochemical age.

959 We note that for the diesel versus gasoline analysis presented in the preceding paragraph
960 three important assumptions are made. First, it is assumed that SOA precursors in the South
961 Coast Air Basin are dominated by motor vehicle emissions. While this is consistent with
962 measured VOC/CO ratios [Warneke *et al.*, 2012], the possibility of important and unidentified
963 SOA precursors from non-vehicular sources cannot be completely ruled out. Therefore, further
964 research is needed to constrain the contribution of non-vehicular sources to SOA.

965 The second important assumption is that some of the SOA measured may be due to long
966 range transport, which is not accounted for in the preceding analysis. To at least partially account
967 for this possible source of error, we repeat the analysis above but only for photochemical ages
968 above 0.1 days. Photochemical ages above 0.1 days generally occur during daytime when the
969 higher amount of SV-OOA versus LV-OOA indicates that SOA production is more local and
970 recent. The resulting slopes of the regression analyses are 121(\pm 7) and 115(\pm 10) $\mu\text{g sm}^{-3} \text{ppmv}^{-1}$

971 for weekdays and Sunday, respectively, and then the ratio of the slopes is $1.0(\pm 0.1)$. This ratio
972 corresponds to diesel emissions accounting for $-2(+21/-26)\%$ of the OOA mass. The upper limit
973 of this range is less than that for the original analysis (36%) for all photochemical ages. Thus, we
974 report the $19(+17/-21)\%$ result, since it is more conservative and represents the entirety of the
975 campaign.

976 The third assumption made in this analysis is that SOA yields do not change on weekends
977 when NO_x concentrations are lower. To test the impact of this assumption the branching ratios
978 for the high- NO_x and low- NO_x VOC oxidation channels were calculated following the same
979 method as described in Dzepina et al. [2011]. It is found that the high- NO_x channel dominates on
980 both weekdays and Sundays with mean branching ratios of 99% and 91%, respectively (see
981 Section F of the supporting material for box-and-whiskers plot). Using the NO_x -dependent
982 yields of Tsimpidi et al. [Tsimpidi et al., 2010] this difference in branching ratio would
983 correspond to an increase in weekend SOA yields of 1% (assuming a $7 \mu\text{g}/\text{m}^3$ OA concentration)
984 for the aromatic precursors that dominate SOA formation from VOCs [Dzepina et al., 2011;
985 Dzepina et al., 2009]. This difference in yields would only change the determined diesel
986 contribution by about 2%, which is much smaller than our reported uncertainty. Thus, the
987 assumption that SOA yields do not change on weekends is robust. However, it should be noted
988 that primary semi-volatile and intermediate volatility compounds may have an important
989 contribution to SOA formation in the South Coast Air Basin [Robinson et al., 2007], but their
990 NO_x -dependent SOA yields are not well constrained.

991 **4. Conclusions**

992 Ambient aerosol measurements were made using a suite of aerosol composition
993 instruments, including on- and off-line bulk and single particle methods at the Pasadena ground
994 site during May and June 2010 as part of the CalNex campaign. Organic aerosols account for
995 41% of the total submicron aerosol mass. An in-depth analysis of OA in Pasadena was carried
996 out including a comparison to measurements from previous field campaigns. Positive matrix
997 factorization analysis of the high resolution mass spectra resolved five components from the total
998 organic mass. The identified components are hydrocarbon-like organic aerosol (HOA, primary
999 combustion), cooking-influenced organic aerosol (CIOA), semi-volatile oxygenated organic
1000 aerosol (SV-OOA, fresh secondary), low volatility oxygenated organic aerosol (LV-OOA, aged
1001 secondary), and amine-rich local organic aerosol (LOA) that accounts for a small amount of the
1002 OA mass. A large majority of the OA mass is classified as oxygenated / secondary (66%), but
1003 there are important contributions from the primary components with HOA and CIOA accounting
1004 for 12% and 17% of the total OA mass, respectively. To compare the OA oxidation reactions
1005 occurring in different regions of the South Coast Air Basin, the Van Krevelen diagrams for
1006 Pasadena and Riverside are analyzed and it is observed that OOA components follow a similar
1007 line with a slope of -0.55 .

1008 The HOA component correlates well with EC, and the emission ratio of HOA to EC
1009 varies with the relative importance of diesel versus gasoline vehicle emissions at the Pasadena
1010 ground site. The dependence of secondary organic aerosol concentration on photochemical
1011 oxidation is quantitatively similar to other urban field sites suggesting similar SOA chemistry
1012 and sources. First, the OA to ΔCO ratios for Pasadena increase with photochemical age and
1013 closely resemble the upper limit of analogous data from Mexico City and the northeastern United
1014 States. Thus, within experimental error, the OA production per unit CO is the same in Pasadena

1015 compared to other locations. Second, the OOA to odd-oxygen ratios for Pasadena are similar to
1016 those observed in Riverside and Mexico City, which indicates that SOA and odd-oxygen
1017 production rates are proportional across the different sites. Both HOA and EC exhibit weekly
1018 cycles with substantially lower concentrations on Sundays versus weekdays consistent with the
1019 well-known weekday/weekend effect in the South Coast Air Basin. The decreases in HOA and
1020 EC concentrations are quantitatively similar to those predicted for their emissions using fuel
1021 sales, traffic counts, and literature gasoline and diesel vehicle emission ratios. In contrast, OOA
1022 does not display a strong weekly cycle – after controlling for differences in photochemical ages
1023 and emission strengths – which is consistent with the dominance of gasoline emissions in SOA
1024 formation, insofar as non-vehicular emissions of SOA precursors are minor. In total, the findings
1025 reported here highlight several quantitative similarities in SOA properties observed in Pasadena,
1026 Riverside, Mexico City, and the northeastern United States including the ratios of SOA to odd-
1027 oxygen, the increases in $OA/\Delta CO$ with photochemical age, and the evolution of elemental
1028 composition (i.e. H:C versus O:C). These observations are consistent with a relatively constant
1029 mix of sources of CO, O₃ precursors, and SOA precursors across urban locations in North
1030 America.

1031

1032 5. Appendix: Size Distributions, chemical aging of sea salt, and particulate charge balance

1033 Displayed in Figure 12 are the AMS size distributions (Panel A), XRF size distributions
1034 (Panel C), and the contribution of all species to the total aerosol mass as a function of particle
1035 size (Panel D). The rBC size distribution was measured by the SP-AMS and is normalized to the
1036 total EC concentration measured by the online Sunset analyzer. As seen in Figure 12D, the
1037 smaller particles, especially those below 200 nm, are predominately composed of OA. In
1038 contrast, the larger particles have an increasing inorganic contribution due to nitrate, sulfate,
1039 ammonium, and the non-EC refractory components. The AMS size distributions have a gradual
1040 cut of approximately PM_{10} , and can have a tail due to slow evaporating particles [*Canagaratna et*
1041 *al.*, 2004] and should be interpreted accordingly. Also shown in Figure 12E are the PALMS size
1042 distributions, which feature a broad submicron mode that is dominated by the
1043 sulfate/organic/nitrate particle type as well as a supermicron mode composed primarily of sea
1044 salt. The PALMS distributions above 2.5 μm and below 200 nm underestimate concentrations
1045 due to instrument limitations associated with both the PALMS and WLOPC.

1046 Further information about the OA, nitrate, and sulfate size distributions can be inferred
1047 from comparisons of various PM_{10} and $PM_{2.5}$ measurements. For sulfate and OA the comparisons
1048 indicate that on average an overwhelming majority of the mass for these species is below 1 μm ,
1049 but for nitrate there appears to be a substantial amount mass above 1 μm . Specifically, a
1050 regression analysis of OC concentrations from the AMS, a PM_{10} instrument, and several $PM_{2.5}$
1051 OC time series taken from the GIT, EPA, and UNC filter samples results in slopes greater than
1052 0.81, when the AMS data is plotted on the y-axis. (Supporting Material Section B contains
1053 further details about the OA, sulfate, and nitrate comparisons.) This observation indicates that
1054 less than about 20% of the OC mass is above 1 μm . Similarly, a regression analysis of sulfate

1055 concentrations from the AMS and a PM_{2.5} PILS-IC instrument results in slope of 1.01 leading to
1056 the conclusion that the sulfate mass above 1 μm is insignificant on average. The regression
1057 analysis of AMS and PILS-IC concentration data for nitrate results in a much different finding,
1058 and exhibits slope of 0.64 that is also dependent on sea salt concentrations measured by the
1059 PALMS instrument. These observations indicate that a substantial amount of nitrate mass is
1060 present above 1 μm , about 35%, and that the supermicron nitrate is at least partially comprised of
1061 sodium nitrate from chemical aging of sea salt by nitric acid although some supermicron
1062 ammonium nitrate may be present as well. The PILS-IC inlet was alternated between a PM₁ and
1063 PM_{2.5} cyclone for a portion of the measurement period (6/12 – 6/16), which provides data that
1064 can also be used to assess the amount of sulfate and nitrate between 1 and 2.5 μm . The linear
1065 regressions of the PM₁ and linearly interpolated PM_{2.5} data indicate that 34% and 80% of the
1066 nitrate and sulfate mass was present below 1 μm . (Note: Interpolation of the PM_{2.5} data is
1067 necessary since only a single inlet and cyclone were used for the PILS-IC measurement
1068 preventing simultaneous measurements with different size cuts.) Similar to the AMS versus PILS
1069 comparison, these percentages indicate that the supermicron mass represents a greater fraction of
1070 the PM_{2.5} mass for nitrate relative to sulfate. When using the PILS data with alternating cyclones
1071 a larger percentage of supermicron mass is found than in the AMS versus PILS comparison. This
1072 difference may be due to the stronger influence of sea salt during the portion of the campaign
1073 when the cyclones were alternated, as clearly seen in the PALMS time series (Figure 1E), which
1074 is consistent with substantial amounts of sodium nitrate, and to a lesser extent sodium sulfate,
1075 above 1 μm . The aging of sea salt upon exposure to pollution is described further in the next
1076 paragraph.

1077 Both the CalNex XRF and PALMS measurements provide quantitative information about
 1078 non-EC refractory materials including sea salt. An important detail regarding the measurement of
 1079 particulate chloride is that XRF is assumed to measure refractory chloride (rCl) since the XRF
 1080 samples are placed under vacuum before measurements [Johnson *et al.*, 2008]. The non-
 1081 refractory and refractory chloride fractions are thought to be predominately ammonium chloride
 1082 [Salcedo *et al.*, 2006] and sodium chloride (from sea salt), respectively [Malm *et al.*, 1994;
 1083 Simon *et al.*, 2011]. Sodium data is not available from XRF data due to measurement limitations,
 1084 but the sodium mass concentration can be estimated from PALMS sea salt volume
 1085 concentrations as described in the Figure 2 caption. For fresh sea salt the expected ratio of
 1086 chloride to sodium mass concentrations is 1.8 [Finlayson-Pitts *et al.*, 2000]. However, a ratio of
 1087 0.12 is observed for rCl to sodium at the Pasadena ground site indicating that the sodium
 1088 chloride in sea salt aerosol has undergone a substantial amount of chemical processing by nitric
 1089 and sulfuric acid, which depletes the amount of chloride ions in the sea salt aerosol by converting
 1090 sodium chloride to sodium nitrate and sodium sulfate [Gard *et al.*, 1998]. For Pasadena, a
 1091 fractional chloride depletion of 94% is calculated using the following equation described by
 1092 Zhuang *et al.* [1999]. (In Equation 3 all concentrations are in units of moles m⁻³.)

1093
$$Depletion = \frac{[Cl]_{original} - [Cl]}{[Cl]_{original}} \times 100\% = \frac{1.174[Na] - [Cl]}{1.174[Na]} \times 100\% \quad (3)$$

1094 This agrees with qualitative results from the PALMS mass spectra, which show significant
 1095 displacement of chloride and accumulation of nitrate on individual sea salt particles that
 1096 correlated with nitric acid concentrations.

1097 The acidity of the submicron aerosols in Pasadena can be evaluated by comparing the
1098 measured ammonium mass concentration against the amount needed to fully neutralize the
1099 measured sulfate, nitrate, and chloride, which is termed here ‘NH₄⁺ predicted’. The AMS
1100 measurements of non-refractory aerosol composition were used for this charge balance
1101 calculation. Particles are considered acidic if the measured ammonium concentration is
1102 substantially lower than the predicted values [*Q Zhang et al.*, 2007a]. As seen in Figure 13A,
1103 overall the particles appear to be bulk neutralized by ammonium with a majority of the data near
1104 the one-to-one line. It should be noted that the measured amines are not accounted for in the
1105 predicted ammonium, but even if it is assumed that the amines are all present as salts, the impact
1106 on the fit is minimal with the slope changing from 1.02 to 0.99 or 0.96 when AMS or FTIR
1107 measurements of amines are used, respectively. There are selected periods when the measured
1108 ammonium concentrations are not sufficient to neutralize the anions, especially at lower
1109 concentrations. These periods are more easily observed in the histogram shown in Figure 13B.
1110 The low ammonium measured-to-predicted ratios may be due to more acidic particles, but based
1111 on PALMS spectra only about 0.1% of particles contained sulfate that was highly acidic
1112 (NH₄⁺:SO₄²⁻ < 1) [*Froyd et al.*, 2009]. An alternative explanation then is the presence of sodium
1113 cations that are not accounted for in Figures 13A and 13B. Typically when using AMS data to
1114 evaluate particle acidity it must be assumed that ammonium is the only significant cation, and
1115 cations from sources such as sea salt are ignored [*Aiken et al.*, 2009; *Docherty et al.*, 2011; *Q*
1116 *Zhang et al.*, 2007a]. For Pasadena however, sodium concentration data can be estimated from
1117 PALMS measurements providing an opportunity to evaluate the role of sea salt in particle
1118 neutralization. (Note: The PALMS data was restricted to the submicron size range to match the
1119 AMS measurements.) In Figure 13C, there is a clear dependence of the ammonium measured-to-

1120 predicted ratios on the fraction of cations that are sodium (ratios are taken from molar units),
1121 which indicates that sodium plays a role in the charge balance.

1122 An important consideration when evaluating particle neutralization is whether the sodium
1123 cations are present as sodium nitrate or sodium chloride, and if those species can be vaporized by
1124 the AMS heater for detection. From the charge balance calculations above it appears that anions
1125 associated with sodium are detected by the AMS indicating that at least a fraction of the sodium
1126 nitrate evaporates rapidly (~ 1 s) in the AMS. The chloride depletion results and size distribution
1127 analysis discussed above indicate that a large majority of the sodium is present as sodium nitrate,
1128 which is more volatile than sodium chloride, and thus, more readily detected by the AMS, in
1129 which the vaporizer temperature was operated at approximately 600°C . Therefore, it appears that
1130 counter ions associated with sodium from sea salt do impact the AMS measurements of charge
1131 balance.

1132 Previously, Docherty et al. [2011] demonstrated that for Riverside during the SOAR-1
1133 campaign organonitrates and organosulfates impacted the charge balance calculation. These
1134 species add to the nitrate and sulfate mass measured by the AMS [Farmer et al., 2010] due to
1135 fragmentation of the molecular parent, but do not contribute the expected amount of ionic
1136 charge, which leads to apparent particle acidity. An important contrast between Pasadena and
1137 Riverside is that the deviation between measured ammonium and NH_4^+ predicted occurs at low
1138 concentrations for Pasadena, but at high concentrations for Riverside. In addition, the measured
1139 versus predicted scatter plot for Pasadena has slope close to one, 1.02, whereas the analogous
1140 plot for Riverside has a lower slope of 0.86. (Note: sodium from sea salt is not accounted for in
1141 either slope.) For Riverside, the deviation in the slope from one was attributed to organosulfates
1142 and organonitrates. For Pasadena the charge balance calculation does not appear to be

1143 significantly impacted by organosulfates or organonitrates, which implies that the concentrations
1144 for these species are relatively low. This conclusion is supported by measurements from other
1145 instruments. The PALMS instrument observed that the isoprene-derived organosulfate, IEPOX
1146 sulfate ester, comprised <0.01% of submicron aerosol mass in Pasadena, which supports the
1147 negligible role of organosulfates in this location. (Note: The mass abundance for the IEPOX
1148 sulfate ester was determined using detailed laboratory calibrations that were performed for a
1149 previous study [*Froyd et al.*, 2010].) Furthermore, FTIR measurements of organonitrates [*Day et*
1150 *al.*, 2010] found that concentrations were less than 2% of the measured nitrate (by AMS) on
1151 average, which is much lower than the percentage estimated in Riverside (10%).

1152 Combining the discussions of size distributions and sea salt aging from above, in Figure
1153 12B the rCl to Mg ratio is shown as function of particle size for the period of high marine
1154 influence identified in Section 3.1 (5/20/2010 – 5/25/2010). During this period rCl and Mg are
1155 correlated in the larger XRF size bins ($R > 0.62$), and the ratio of the Mg PM₁ mass concentration
1156 to the PALMS sea salt PM₁ mass concentration is very close to the expected ratio for sea salt:
1157 0.044 vs. 0.039, respectively ($R = 0.6$) [*Finlayson-Pitts and Pitts*, 2000]. Thus, Mg is taken to be
1158 predominately from sea salt, which allows for calculating the amount of chloride depletion
1159 following an approach analogous to that described for sodium. (Data is not shown for smaller
1160 particle diameters since a strong correlation between rCl and Mg is not observed.) The rCl to Mg
1161 ratio is fairly constant with particle size from 660 to 3010 nm d_{va} indicating similar amounts of
1162 chloride depletion. Additionally, the average rCl to Mg ratio (2.0) corresponds to 86% chloride
1163 depletion, which is similar to 94% chloride depletion calculated using the estimated sodium data
1164 from the PALMS instrument. In general, the sea salt measured in Pasadena appears to be very
1165 aged mostly from chemical reactions with nitric acid. The extensive chloride depletion observed

1166 in Pasadena is consistent with previous work including modeling studies that predicted ~80%
1167 chloride depletion in Riverside, CA [*Knipping and Dabdub*, 2003], and single particle mass
1168 spectra of aged sea salt, also from Riverside, which showed extensive chloride depletion
1169 [*Hughes et al.*, 2000]. In addition, chloride depletions of 71 and 74% were reported for coarse
1170 mode aerosol in Upland and Rubidoux, CA, respectively [*Eldering et al.*, 1991]. These values
1171 are lower than observed for Pasadena in this study, which may be due to the Eldering et al.
1172 percentages corresponding to particles greater than 2.2 μm in diameter.

1173 The extensive depletion of chloride from sea salt suggests that appreciable amounts of
1174 chlorine radicals may be present due to the photolysis of photo-labile chlorinated gases such as
1175 HCl, ClNO₂, and Cl₂. Oxidation reactions of organics by chlorine radicals that produce
1176 organochlorines in the particle phase would then be possible. To investigate this possibility the
1177 concentrations of several organochlorine fragments were determined from the AMS
1178 measurements (CCl⁺, C₂HCl⁺, CCl₂⁺, C₂Cl₂⁺, C₂HCl₂⁺, CHOCl₂⁺). The relative concentration of
1179 these species compared to the total OA is very small, on average less than 0.1% and always less
1180 than 0.4%. In addition, the 2DTAG identified only one chlorine-containing OA compound,
1181 chlorophthalic acid, which represents less than 1% of the total phthalic acid concentration. These
1182 results are also consistent with FTIR spectra of filter samples collected during the CalNex
1183 campaign, which do not display vibrational resonances for acid chlorides (730-550 cm⁻¹) or alkyl
1184 chlorides (785-540 cm⁻¹). It is noted though that quantification of organochlorines by FTIR is
1185 difficult due to Teflon filter interferences in the same spectral region. In total, these
1186 measurements provide no evidence for organochlorines representing a substantial portion of the
1187 OA mass, but the methods utilized here are not optimal for the detection of organochlorines.
1188

1189 **6. Acknowledgements**

1190 The authors thank Profs. Jochen Stutz and John Seinfeld for their leadership in organizing
1191 the Pasadena ground site, and CARB and NOAA for support of the site setup. We also wish to
1192 thank Dr. Ingrid Ulbrich for helpful discussions regarding the PMF analysis, and Dr. Cora
1193 Young for providing radical budgets for the CalNex ground site. The Jimenez Group
1194 acknowledges support from CARB 08-319 and CARB 11-305 as well as DOE (BER, ASR
1195 Program) DE-SC0006035, DE-SC0006711, and DE-FG02-11ER65293. PLH and AMO
1196 acknowledge fellowships from the CIRES Visiting Fellows Program and US DOE SCGF
1197 Program (ORAU, ORISE, DE-AC05-06OR23100), respectively. JT and JDA acknowledge
1198 funding from the Natural Environment Research Council [Ref: NE/H008136/1]. RJW and
1199 XZ were funded through National Science Foundation grants ATM-0931492 and ATM-
1200 0802237. ALC acknowledges fellowship support from US DOE SCGF Program (ORAU,
1201 ORISE, DE-AC05-06OR23100) and other expenses from NSF grant AGS-1009408. YZ and
1202 SSC acknowledge support from CARB 09-350. The US Environmental Protection Agency
1203 (EPA) through its Office of Research and Development collaborated in the research described
1204 here; the manuscript has been subjected to peer review and has been cleared for publication;
1205 mention of trade names or commercial products does not constitute endorsement or
1206 recommendation for use by the EPA.

1207 **7. References**

1208

1209 Aiken, A. C., P. F. DeCarlo, and J. L. Jimenez (2007), Elemental analysis of organic species with electron
1210 ionization high-resolution mass spectrometry, *Anal. Chem.*, 79(21), 8350-8358.

1211

1212 Aiken, A. C., et al. (2010), Mexico city aerosol analysis during MILAGRO using high resolution aerosol
1213 mass spectrometry at the urban supersite (T0) - Part 2: Analysis of the biomass burning contribution and
1214 the non-fossil carbon fraction, *Atmos. Chem. Phys.*, 10(12), 5315-5341.

1215

1216 Aiken, A. C., et al. (2008), O/C and OM/OC ratios of primary, secondary, and ambient organic aerosols
1217 with high-resolution time-of-flight aerosol mass spectrometry, *Environ. Sci. Technol.*, 42(12), 4478-4485.

1218

1219 Aiken, A. C., et al. (2009), Mexico City aerosol analysis during MILAGRO using high resolution aerosol
1220 mass spectrometry at the urban supersite (T0) - Part 1: Fine particle composition and organic source
1221 apportionment, *Atmos. Chem. Phys.*, 9(17), 6633-6653.

1222

1223 Allan, J. D., P. I. Williams, W. T. Morgan, C. L. Martin, M. J. Flynn, J. Lee, E. Nemitz, G. J. Phillips, M.
1224 W. Gallagher, and H. Coe (2010), Contributions from transport, solid fuel burning and cooking to
1225 primary organic aerosols in two UK cities, *Atmos. Chem. Phys.*, 10(2), 647-668.

1226

1227 Allan, J. D., et al. (2003), Quantitative sampling using an Aerodyne aerosol mass spectrometer: 2.
1228 Measurements of fine particulate chemical composition in two UK cities, *J. Geophys. Res.-Atmos.*,
1229 108(D3), 4091.

1230

1231 Allan, J. D., et al. (2004), A generalised method for the extraction of chemically resolved mass spectra
1232 from Aerodyne aerosol mass spectrometer data, *J. Aerosol. Sci.*, 35(7), 909-922.

1233

1234 Apel, E. C., et al. (2010), Chemical evolution of volatile organic compounds in the outflow of the Mexico
1235 City Metropolitan area, *Atmos. Chem. Phys.*, 10(5), 2353-2375.

1236

1237 American Lung Association (2011), State of the Air, <http://www.stateoftheair.org/>

1238

1239 Ault, A. P., M. J. Moore, H. Furutani, and K. A. Prather (2009), Impact of Emissions from the Los
1240 Angeles Port Region on San Diego Air Quality during Regional Transport Events, *Environ. Sci. Technol.*,
1241 43(10), 3500-3506.

1242

1243 Bahreini, R., et al. (2012), Gasoline emissions dominate over diesel in formation of secondary organic
1244 aerosol mass, *Geophys. Res. Lett.*, 39(6), L06805.

1245

1246 Ban-Weiss, G. A., J. P. McLaughlin, R. A. Harley, A. J. Kean, E. Grosjean, and D. Grosjean (2008a),
1247 Carbonyl and nitrogen dioxide emissions from gasoline- and diesel-powered motor vehicles, *Environ. Sci.*
1248 *Technol.*, 42(11), 3944-3950.

1249
1250 Ban-Weiss, G. A., J. P. McLaughlin, R. A. Harley, M. M. Lunden, T. W. Kirchstetter, A. J. Kean, A. W.
1251 Strawa, E. D. Stevenson, and G. R. Kendall (2008b), Long-term changes in emissions of nitrogen oxides
1252 and particulate matter from on-road gasoline and diesel vehicles, *Atmos. Environ.*, 42(2), 220-232.

1253
1254 Bhattacharya, S. C., D. O. Albina, and P. A. Salam (2002), Emission factors of wood and charcoal-fired
1255 cookstoves, *Biomass Bioenerg.*, 23(6), 453-469.

1256
1257 Blumenthal, D. L., W. H. White, and T. B. Smith (1978), Anatomy of a Los Angeles smog episode -
1258 pollutant transport in daytime sea breeze regime, *Atmos. Environ.*, 12(4), 893-907.

1259
1260 BOE: California State Board of Equalization (2011), Fuel Taxes Statistics & Reports,
1261 <http://www.boe.ca.gov/sptaxprog/spftrpts.htm>

1262
1263 Bon, D. M., et al. (2011), Measurements of volatile organic compounds at a suburban ground site (T1) in
1264 Mexico City during the MILAGRO 2006 campaign: measurement comparison, emission ratios, and
1265 source attribution, *Atmos. Chem. Phys.*, 11(6), 2399-2421.

1266
1267 Brioude, J., W. M. Angevine, S. A. McKeen, and E. Y. Hsie (2012), Numerical uncertainty at mesoscale
1268 in a Lagrangian model in complex terrain, *Geosci. Model Dev.*, 5(5), 1127-1136.

1269
1270 Caltrans: California Department of Transportation (2010), Caltrans Performance Measurement System,
1271 <http://pems.dot.ca.gov/>

1272
1273 Canagaratna, M. R., et al. (2004), Chase studies of particulate emissions from in-use New York City
1274 vehicles, *Aerosol Sci. Technol.*, 38(6), 555-573.

1275
1276 Cappa, C. D., and J. L. Jimenez (2010), Quantitative estimates of the volatility of ambient organic
1277 aerosol, *Atmos. Chem. Phys.*, 10(12), 5409-5424.

1278
1279 CARB: California Air Resources Board (2008), California Emission Inventory Data,
1280 <http://www.arb.ca.gov/ei/emsmain/emsmain.htm>

1281
1282 Chang, W. L., P. V. Bhave, S. S. Brown, N. Riemer, J. Stutz, and D. Dabdub (2011), Heterogeneous
1283 Atmospheric Chemistry, Ambient Measurements, and Model Calculations of N₂O₅: A Review, *Aerosol*
1284 *Sci. Technol.*, 45(6), 665-695.

1285

1286 Chinkin, L. R., D. L. Coe, T. H. Funk, H. R. Hafner, P. T. Roberts, P. A. Ryan, and D. R. Lawson (2003),
1287 Weekday versus weekend activity patterns for ozone precursor emissions in California's South Coast Air
1288 Basin, *J. Air Waste Manage. Assoc.*, 53(7), 829-843.

1289
1290 Crippa, M., et al. (2013), Wintertime aerosol chemical composition and source apportionment of the
1291 organic fraction in the metropolitan area of Paris, *Atmos. Chem. Phys.*, 13(2), 961-981.

1292
1293 Croes, B. E., and E. M. Fujita (2003), Overview of the 1997 Southern California Ozone Study (SCOS97-
1294 NARSTO), *Atmos. Environ.*, 37, S3-S26.

1295
1296 Cubison, M. J., et al. (2011), Effects of aging on organic aerosol from open biomass burning smoke in
1297 aircraft and laboratory studies, *Atmos. Chem. Phys.*, 11(23), 12049-12064.

1298
1299 Day, D. A., S. Liu, L. M. Russell, and P. J. Ziemann (2010), Organonitrate group concentrations in
1300 submicron particles with high nitrate and organic fractions in coastal southern California, *Atmos.*
1301 *Environ.*, 44(16), 1970-1979.

1302
1303 de Gouw, J. A., et al. (2012), Increasing atmospheric burden of ethanol in the United States, *Geophys.*
1304 *Res. Lett.*, 39(15), L15803.

1305
1306 DeCarlo, P. F., et al. (2010), Investigation of the sources and processing of organic aerosol over the
1307 Central Mexican Plateau from aircraft measurements during MILAGRO, *Atmos. Chem. Phys.*, 10(12),
1308 5257-5280.

1309
1310 DeCarlo, P. F., et al. (2006), Field-Deployable, High-Resolution, Time-of-Flight Aerosol Mass
1311 Spectrometer, *Anal. Chem.*, 78, 8281-8289.

1312
1313 Docherty, K. S., et al. (2008), Apportionment of Primary and Secondary Organic Aerosols in Southern
1314 California during the 2005 Study of Organic Aerosols in Riverside (SOAR-1), *Environ. Sci. Technol.*,
1315 42(20), 7655-7662.

1316
1317 Docherty, K. S., et al. (2011), The 2005 Study of Organic Aerosols at Riverside (SOAR-1): instrumental
1318 intercomparisons and fine particle composition, *Atmos. Chem. Phys.*, 11(23), 12387-12420.

1319
1320 Dockery, D. W., and C. A. Pope (1994), Acute respiratory effects of particulate air-pollution, *Annual*
1321 *Review of Public Health*, 15, 107-132.

1322
1323 Dockery, D. W., C. A. Pope, X. P. Xu, J. D. Spengler, J. H. Ware, M. E. Fay, B. G. Ferris, and F. E.
1324 Speizer (1993), An association between air-pollution and mortality in 6 united-states cities, *New England*
1325 *Journal of Medicine*, 329(24), 1753-1759.

1326

1327 Dunlea, E. J., et al. (2009), Evolution of Asian aerosols during transpacific transport in INTEX-B, *Atmos.*
1328 *Chem. Phys.*, 9(19), 7257-7287.

1329

1330 Dusanter, S., D. Vimal, P. S. Stevens, R. Volkamer, and L. T. Molina (2009), Measurements of OH and
1331 HO₂ concentrations during the MCMA-2006 field campaign – Part 1: Deployment of the Indiana
1332 University laser-induced fluorescence instrument, *Atmos. Chem. Phys.*, 9(5), 1665-1685.

1333

1334 Dzepina, K., C. D. Cappa, R. M. Volkamer, S. Madronich, P. F. DeCarlo, R. A. Zaveri, and J. L. Jimenez
1335 (2011), Modeling the Multiday Evolution and Aging of Secondary Organic Aerosol During MILAGRO
1336 2006, *Environ. Sci. Technol.*, 45(8), 3496-3503.

1337

1338 Dzepina, K., R. M. Volkamer, S. Madronich, P. Tulet, I. M. Ulbrich, Q. Zhang, C. D. Cappa, P. J.
1339 Ziemann, and J. L. Jimenez (2009), Evaluation of recently-proposed secondary organic aerosol models
1340 for a case study in Mexico City, *Atmos. Chem. Phys.*, 9(15), 5681-5709.

1341

1342 Eldering, A., P. A. Solomon, L. G. Salmon, T. Fall, and G. R. Cass (1991), Hydrochloric acid - a regional
1343 perspective on concentrations and formation in the atmosphere of southern California, *Atmospheric*
1344 *Environment Part a-General Topics*, 25(10), 2091-2102.

1345

1346 EPA: United States Environmental Protection Agency (2012), Black Carbon: Basic Information,
1347 <http://www.epa.gov/blackcarbon/basic.html>

1348

1349 Farmer, D. K., A. Matsunaga, K. S. Docherty, J. D. Surratt, J. H. Seinfeld, P. J. Ziemann, and J. L.
1350 Jimenez (2010), Response of an aerosol mass spectrometer to organonitrates and organosulfates and
1351 implications for atmospheric chemistry, *Proceedings of the National Academy of Sciences of the United*
1352 *States of America*, 107(15), 6670-6675.

1353

1354 Finlayson-Pitts, B. J., and J. N. Pitts (2000), *Chemistry of the Upper and Lower Atmosphere*, Academic
1355 Press, San Diego.

1356

1357 Froyd, K. D., S. M. Murphy, D. M. Murphy, J. A. de Gouw, N. C. Eddingsaas, and P. O. Wennberg
1358 (2010), Contribution of isoprene-derived organosulfates to free tropospheric aerosol mass, *Proceedings of*
1359 *the National Academy of Sciences of the United States of America*, 107(50), 21360-21365.

1360

1361 Froyd, K. D., D. M. Murphy, T. J. Sanford, D. S. Thomson, J. C. Wilson, L. Pfister, and L. Lait (2009),
1362 Aerosol composition of the tropical upper troposphere, *Atmos. Chem. Phys.*, 9(13), 4363-4385.

1363

1364 Fruin, S. A., M. J. St Denis, A. M. Winer, S. D. Colome, and F. W. Lurmann (2001), Reductions in
1365 human benzene exposure in the California South Coast Air Basin, *Atmos. Environ.*, 35(6), 1069-1077.

1366

1367 Gard, E. E., et al. (1998), Direct observation of heterogeneous chemistry in the atmosphere, *Science*,
1368 279(5354), 1184-1187.

1369
1370 Gentner, D. R., et al. (2012), Elucidating secondary organic aerosol from diesel and gasoline vehicles
1371 through detailed characterization of organic carbon emissions, *Proceedings of the National Academy of*
1372 *Sciences*, 109(45), 18318-18323.

1373
1374 Gerbig, C., S. Schmitgen, D. Kley, A. Volz-Thomas, K. Dewey, and D. Haaks (1999), An improved fast-
1375 response vacuum-UV resonance fluorescence CO instrument, *J. Geophys. Res.-Atmos.*, 104(D1), 1699-
1376 1704.

1377
1378 Gilman, J. B., et al. (2009), Measurements of volatile organic compounds during the 2006
1379 TexAQS/GoMACCS campaign: Industrial influences, regional characteristics, and diurnal dependencies
1380 of the OH reactivity, *J. Geophys. Res.*, 114, D00F06.

1381
1382 Griffin, R. J., J. J. Chen, K. Carmody, S. Vutukuru, and D. Dabdub (2007), Contribution of gas phase
1383 oxidation of volatile organic compounds to atmospheric carbon monoxide levels in two areas of the
1384 United States, *J. Geophys. Res.-Atmos.*, 112(D10), D10S17.

1385
1386 Hall, J. S., and E. W. Wolff (1998), Causes of seasonal and daily variations in aerosol sea-salt
1387 concentrations at a coastal Antarctic station, *Atmos. Environ.*, 32(21), 3669-3677.

1388
1389 Haman, C. L., B. Lefer, and G. A. Morris (2012), Seasonal Variability in the Diurnal Evolution of the
1390 Boundary Layer in a Near Coastal Urban Environment, *Journal of Atmospheric and Oceanic Technology*.

1391
1392 Harley, R. A., R. F. Sawyer, and J. B. Milford (1997), Updated photochemical modeling for California's
1393 South Coast Air Basin: Comparison of chemical mechanisms and motor vehicle emission inventories,
1394 *Environ. Sci. Technol.*, 31(10), 2829-2839.

1395
1396 Heald, C. L., J. H. Kroll, J. L. Jimenez, K. S. Docherty, P. F. DeCarlo, A. C. Aiken, Q. Chen, S. T.
1397 Martin, D. K. Farmer, and P. Artaxo (2010), A simplified description of the evolution of organic aerosol
1398 composition in the atmosphere, *Geophys. Res. Lett.*, 37, L08803.

1399
1400 Healy, R. M., I. P. O'Connor, S. Hellebust, A. Allan, J. R. Sodeau, and J. C. Wenger (2009),
1401 Characterisation of single particles from in-port ship emissions, *Atmos. Environ.*, 43(40), 6408-6414.

1402
1403 Herndon, S. C., et al. (2008), Correlation of secondary organic aerosol with odd oxygen in Mexico City,
1404 *Geophys. Res. Lett.*, 35(15), L15804.

1405

1406 Hersey, S. P., J. S. Craven, K. A. Schilling, A. R. Metcalf, A. Sorooshian, M. N. Chan, R. C. Flagan, and
1407 J. H. Seinfeld (2011), The Pasadena Aerosol Characterization Observatory (PACO): chemical and
1408 physical analysis of the Western Los Angeles basin aerosol, *Atmos. Chem. Phys.*, *11*(15), 7417-7443.

1409
1410 Hildebrandt, L., E. Kostenidou, V. A. Lanz, A. S. H. Prevot, U. Baltensperger, N. Mihalopoulos, A.
1411 Laaksonen, N. M. Donahue, and S. N. Pandis (2011), Sources and atmospheric processing of organic
1412 aerosol in the Mediterranean: insights from aerosol mass spectrometer factor analysis, *Atmos. Chem.*
1413 *Phys.*, *11*(23), 12499-12515.

1414
1415 Hildemann, L. M., G. R. Markowski, and G. R. Cass (1991), Chemical-composition of emissions from
1416 urban sources of fine organic aerosol, *Environ. Sci. Technol.*, *25*(4), 744-759.

1417
1418 Hodzic, A., and J. L. Jimenez (2011), Modeling anthropogenically-controlled secondary organic aerosols
1419 in a megacity: a simplified framework for global and climate models, *Geosci. Model Dev.*, *4*, 901-917.

1420
1421 Hodzic, A., J. L. Jimenez, A. S. H. Prevot, S. Szidat, J. D. Fast, and S. Madronich (2010), Can 3-D
1422 models explain the observed fractions of fossil and non-fossil carbon in and near Mexico City?, *Atmos.*
1423 *Chem. Phys.*, *10*(22), 10997-11016.

1424
1425 Huang, X. F., et al. (2010), Highly time-resolved chemical characterization of atmospheric submicron
1426 particles during 2008 Beijing Olympic Games using an Aerodyne High-Resolution Aerosol Mass
1427 Spectrometer, *Atmos. Chem. Phys.*, *10*(18), 8933-8945.

1428
1429 Huffman, J. A., et al. (2009), Chemically-resolved aerosol volatility measurements from two megacity
1430 field studies, *Atmos. Chem. Phys.*, *9*(18), 7161-7182.

1431
1432 Hughes, L. S., J. O. Allen, P. Bhave, M. J. Kleeman, G. R. Cass, D. Y. Liu, D. F. Fergenson, B. D.
1433 Morrical, and K. A. Prather (2000), Evolution of atmospheric particles along trajectories crossing the Los
1434 Angeles basin, *Environ. Sci. Technol.*, *34*(15), 3058-3068.

1435
1436 IPCC (2007), *Climate Change 2007: The Physical Scientific Basis Rep.*, Cambridge University Press,
1437 Cambridge England.

1438
1439 Jacob, D. J., et al. (2010), The Arctic Research of the Composition of the Troposphere from Aircraft and
1440 Satellites (ARCTAS) mission: design, execution, and first results, *Atmos. Chem. Phys.*, *10*(11), 5191-
1441 5212.

1442
1443 Jimenez, J. L., et al. (2003), Ambient aerosol sampling using the Aerodyne Aerosol Mass Spectrometer,
1444 *J. Geophys. Res.-Atmos.*, *108*(D7), 8425.

1445

1446 Jimenez, J. L., et al. (2009), Evolution of Organic Aerosols in the Atmosphere, *Science*, 326(5959), 1525-
1447 1529.

1448

1449 Johnson, K. S., A. Laskin, J. L. Jimenez, V. Shutthanandan, L. T. Molina, D. Salcedo, K. Dzepina, and
1450 M. J. Molina (2008), Comparative analysis of urban atmospheric aerosol by particle-induced X-ray
1451 emission (PIXE), proton elastic scattering analysis (PESA), and aerosol mass spectrometry (AMS),
1452 *Environ. Sci. Technol.*, 42(17), 6619-6624.

1453

1454 Keabian, P. L., W. A. Robinson, and A. Freedman (2007), Optical extinction monitor using cw cavity
1455 enhanced detection, *Rev. Sci. Instrum.*, 78(6), 063102.

1456

1457 Kleinman, L. I., et al. (2007), Aircraft observations of aerosol composition and ageing in New England
1458 and Mid-Atlantic States during the summer 2002 New England Air Quality Study field campaign, *J.*
1459 *Geophys. Res.-Atmos.*, 112(D9), D09310.

1460

1461 Kleinman, L. I., et al. (2008), The time evolution of aerosol composition over the Mexico City plateau,
1462 *Atmos. Chem. Phys.*, 8(6), 1559-1575.

1463

1464 Knipping, E. M., and D. Dabdub (2003), Impact of chlorine emissions from sea-salt aerosol on coastal
1465 urban ozone, *Environ. Sci. Technol.*, 37(2), 275-284.

1466

1467 Lambe, A. T., et al. (2012), Transitions from Functionalization to Fragmentation Reactions of Laboratory
1468 Secondary Organic Aerosol (SOA) Generated from the OH Oxidation of Alkane Precursors, *Environ. Sci.*
1469 *Technol.*, 46(10), 5430-5437.

1470

1471 Langridge, J. M., et al. (2012), Evolution of aerosol properties impacting visibility and direct climate
1472 forcing in an ammonia-rich urban environment, *J. Geophys. Res.-Atmos.*, 117.

1473

1474 Lanz, V. A., M. R. Alfarra, U. Baltensperger, B. Buchmann, C. Hueglin, and A. S. H. Prevot (2007),
1475 Source apportionment of submicron organic aerosols at an urban site by factor analytical modelling of
1476 aerosol mass spectra, *Atmos. Chem. Phys.*, 7(6), 1503-1522.

1477

1478 Lawson, D. R. (1990), The southern california air-quality study, *J. Air Waste Manage. Assoc.*, 40(2), 156-
1479 165.

1480

1481 Lee, S. C., W. M. Li, and L. Y. Chan (2001), Indoor air quality at restaurants with different styles of
1482 cooking in metropolitan Hong Kong, *Sci. Total Environ.*, 279(1-3), 181-193.

1483

1484 Liu, S., D. A. Day, J. E. Shields, and L. M. Russell (2011), Ozone-driven daytime formation of secondary
1485 organic aerosol containing carboxylic acid groups and alkane groups, *Atmos. Chem. Phys.*, 11(16), 8321-
1486 8341.

1487
1488 Lu, R., and R. P. Turco (1995), Air pollutant transport in a coastal environment .2. 3-dimensional
1489 simulations over los-angeles basin, *Atmos. Environ.*, 29(13), 1499-1518.

1490
1491 Malm, W. C., J. F. Sisler, D. Huffman, R. A. Eldred, and T. A. Cahill (1994), Spatial and seasonal trends
1492 in particle concentration and optical extinction in the united-states, *J. Geophys. Res.-Atmos.*, 99(D1),
1493 1347-1370.

1494
1495 Marr, L. C., and R. A. Harley (2002), Spectral analysis of weekday-weekend differences in ambient
1496 ozone, nitrogen oxide, and non-methane hydrocarbon time series in California, *Atmos. Environ.*, 36(14),
1497 2327-2335.

1498
1499 Massoli, P., P. L. Keabian, T. B. Onasch, F. B. Hills, and A. Freedman (2010), Aerosol Light Extinction
1500 Measurements by Cavity Attenuated Phase Shift (CAPS) Spectroscopy: Laboratory Validation and Field
1501 Deployment of a Compact Aerosol Particle Extinction Monitor, *Aerosol Sci. Technol.*, 44(6), 428-435.

1502
1503 McDonald, J. D., B. Zielinska, E. M. Fujita, J. C. Sagebiel, J. C. Chow, and J. G. Watson (2003),
1504 Emissions from charbroiling and grilling of chicken and beef, *J. Air Waste Manage. Assoc.*, 53(2), 185-
1505 194.

1506
1507 McLafferty, F. W., and F. Turecek (1993), *Interpretation of Mass Spectra*, 4th ed., University Science
1508 Books, Sausalito, CA.

1509
1510 Middlebrook, A. M., R. Bahreini, J. L. Jimenez, and M. R. Canagaratna (2012), Evaluation of
1511 Composition-Dependent Collection Efficiencies for the Aerodyne Aerosol Mass Spectrometer using Field
1512 Data, *Aerosol Sci. Technol.*, 46(3), 258-271.

1513
1514 Millstein, D. E., R. A. Harley, and S. V. Hering (2008), Weekly cycles in fine particulate nitrate, *Atmos.*
1515 *Environ.*, 42(4), 632-641.

1516
1517 Mohr, C., et al. (2011), Identification and quantification of organic aerosol from cooking and other
1518 sources in Barcelona using aerosol mass spectrometer data, *Atmos. Chem. Phys.*, 11(10), 1649-1665.

1519
1520 Moore, G. E., S. G. Douglas, R. C. Kessler, and J. P. Killus (1991), Identification and tracking of polluted
1521 air masses in the South-Central Coast Air Basin, *J. Appl. Meteorol.*, 30(5), 715-732.

1522
1523 Murphy, B. N., N. M. Donahue, C. Fountoukis, and S. N. Pandis (2011), Simulating the oxygen content
1524 of ambient organic aerosol with the 2D volatility basis set, *Atmos. Chem. Phys.*, 11(15), 7859-7873.

1525

1526 Nemitz, E. (2010), Aerosol Mass Spectrometer Network Measurements during the EUCAARI/EMEP
1527 Intensive Measurement Campaigns, paper presented at Aerodyne Aerosol Mass Spectrometer Users
1528 Meeting, Hyttiala, Finland, 4 - 6 Sept.

1529
1530 Neuman, J. A., et al. (2003), Variability in ammonium nitrate formation and nitric acid depletion with
1531 altitude and location over California, *J. Geophys. Res.-Atmos.*, 108(D17), 4557.

1532
1533 Ng, N. L., M. R. Canagaratna, J. L. Jimenez, P. S. Chhabra, J. H. Seinfeld, and D. R. Worsnop (2011),
1534 Changes in organic aerosol composition with aging inferred from aerosol mass spectra, *Atmos. Chem.*
1535 *Phys.*, 11(13), 6465-6474.

1536
1537 NOAA: National Oceanic and Atmospheric Administration (2008), 2010 CalNex White Paper: Research
1538 at the Nexus of Air Quality and Climate Change,
1539 <http://www.esrl.noaa.gov/csd/projects/calnex/whitepaper.pdf>

1540
1541 Onasch, T. B., A. Trimborn, E. C. Fortner, J. T. Jayne, G. L. Kok, L. R. Williams, P. Davidovits, and D.
1542 R. Worsnop (2012), Soot Particle Aerosol Mass Spectrometer: Development, Validation, and Initial
1543 Application, *Aerosol Sci. Technol.*, 46(7), 804-817.

1544
1545 Orsini, D. A., Y. L. Ma, A. Sullivan, B. Sierau, K. Baumann, and R. J. Weber (2003), Refinements to the
1546 particle-into-liquid sampler (PILS) for ground and airborne measurements of water soluble aerosol
1547 composition, *Atmos. Environ.*, 37(9-10), 1243-1259.

1548
1549 Paatero, P., and U. Tapper (1994), Positive matrix factorization - a nonnegative factor model with optimal
1550 utilization of error-estimates of data values, *Environmetrics*, 5(2), 111-126.

1551
1552 Paatero, P., and P. K. Hopke (2003), Discarding or downweighting high-noise variables in factor analytic
1553 models, *Analytica Chimica Acta*, 490(1-2), 277-289.

1554
1555 Parrish, D. D., M. Trainer, D. Hereid, E. J. Williams, K. J. Olszyna, R. A. Harley, J. F. Meagher, and F.
1556 C. Fehsenfeld (2002), Decadal change in carbon monoxide to nitrogen oxide ratio in US vehicular
1557 emissions, *J. Geophys. Res.-Atmos.*, 107(D12), 4140.

1558
1559 Parrish, D. D., A. Stohl, C. Forster, E. L. Atlas, D. R. Blake, P. D. Goldan, W. C. Kuster, and J. A. de
1560 Gouw (2007), Effects of mixing on evolution of hydrocarbon ratios in the troposphere, *J. Geophys. Res.-*
1561 *Atmos.*, 112(D10), D10S34.

1562
1563 Peltier, R. E., R. J. Weber, and A. P. Sullivan (2007), Investigating a liquid-based method for online
1564 organic carbon detection in atmospheric particles, *Aerosol Sci. Technol.*, 41(12), 1117-1127.

1565

1566 Pollack, I. B., et al. (2012), Airborne and ground-based observations of a weekend effect in ozone,
1567 precursors, and oxidation products in the California South Coast Air Basin, *J. Geophys. Res.*, *117*,
1568 D00V05.

1569
1570 Robinson, A. L., R. Subramanian, N. M. Donahue, A. Bernardo-Bricker, and W. F. Rogge (2006), Source
1571 apportionment of molecular markers and organic aerosol. 3. Food cooking emissions, *Environ. Sci.*
1572 *Technol.*, *40*(24), 7820-7827.

1573
1574 Robinson, A. L., N. M. Donahue, M. K. Shrivastava, E. A. Weitkamp, A. M. Sage, A. P. Grieshop, T. E.
1575 Lane, J. R. Pierce, and S. N. Pandis (2007), Rethinking organic aerosols: Semivolatile emissions and
1576 photochemical aging, *Science*, *315*(5816), 1259-1262.

1577
1578 Russell, L. M., L. N. Hawkins, A. A. Frossard, P. K. Quinn, and T. S. Bates (2010), Carbohydrate-like
1579 composition of submicron atmospheric particles and their production from ocean bubble bursting,
1580 *Proceedings of the National Academy of Sciences of the United States of America*, *107*(15), 6652-6657.

1581
1582 Russell, L. M., S. Takahama, S. Liu, L. N. Hawkins, D. S. Covert, P. K. Quinn, and T. S. Bates (2009),
1583 Oxygenated fraction and mass of organic aerosol from direct emission and atmospheric processing
1584 measured on the R/V Ronald Brown during TEXAQS/GoMACCS 2006, *J. Geophys. Res.-Atmos.*, *114*,
1585 D00F05.

1586
1587 Salcedo, D., et al. (2006), Characterization of ambient aerosols in Mexico City during the MCMA-2003
1588 campaign with Aerosol Mass Spectrometry: results from the CENICA Supersite, *Atmos. Chem. Phys.*, *6*,
1589 925-946.

1590
1591 Schauer, J. J., M. J. Kleeman, G. R. Cass, and B. R. T. Simoneit (1999), Measurement of emissions from
1592 air pollution sources. 1. C-1 through C-29 organic compounds from meat charbroiling, *Environ. Sci.*
1593 *Technol.*, *33*(10), 1566-1577.

1594
1595 Schauer, J. J., M. J. Kleeman, G. R. Cass, and B. R. T. Simoneit (2002a), Measurement of emissions from
1596 air pollution sources. 5. C-1-C-32 organic compounds from gasoline-powered motor vehicles, *Environ.*
1597 *Sci. Technol.*, *36*(6), 1169-1180.

1598
1599 Schauer, J. J., M. J. Kleeman, G. R. Cass, and B. R. T. Simoneit (2002b), Measurement of emissions from
1600 air pollution sources. 4. C-1-C-27 organic compounds from cooking with seed oils, *Environ. Sci.*
1601 *Technol.*, *36*(4), 567-575.

1602
1603 Schwarz, J. P., et al. (2006), Single-particle measurements of midlatitude black carbon and light-
1604 scattering aerosols from the boundary layer to the lower stratosphere, *J. Geophys. Res.-Atmos.*, *111*(D16),
1605 D16207.

1606

1607 Simon, H., P. V. Bhave, J. L. Swall, N. H. Frank, and W. C. Malm (2011), Determining the spatial and
1608 seasonal variability in OM/OC ratios across the US using multiple regression, *Atmos. Chem. Phys.*, *11*(6),
1609 2933-2949.

1610
1611 Slowik, J. G., et al. (2010), Characterization of a large biogenic secondary organic aerosol event from
1612 eastern Canadian forests, *Atmos. Chem. Phys.*, *10*(6), 2825-2845.

1613
1614 Stohl, A., C. Forster, A. Frank, P. Seibert, and G. Wotawa (2005), Technical note: The Lagrangian
1615 particle dispersion model FLEXPART version 6.2, *Atmos. Chem. Phys.*, *5*, 2461-2474.

1616
1617 Sueper, D. (2011), "ToF-AMS Analysis Software", [http://cires.colorado.edu/jimenez-](http://cires.colorado.edu/jimenez-group/wiki/index.php/ToF-AMS_Analysis_Software)
1618 [group/wiki/index.php/ToF-AMS_Analysis_Software](http://cires.colorado.edu/jimenez-group/wiki/index.php/ToF-AMS_Analysis_Software)

1619
1620 Sun, Y. L., et al. (2011), Characterization of the sources and processes of organic and inorganic aerosols
1621 in New York city with a high-resolution time-of-flight aerosol mass spectrometer, *Atmos. Chem. Phys.*,
1622 *11*(4), 1581-1602.

1623
1624 Thalman, R., and R. Volkamer (2010), Inherent calibration of a blue LED-CE-DOAS instrument to
1625 measure iodine oxide, glyoxal, methyl glyoxal, nitrogen dioxide, water vapour and aerosol extinction in
1626 open cavity mode, *Atmos. Meas. Tech.*, *3*(6), 1797-1814.

1627
1628 Thomson, D. S., M. E. Schein, and D. M. Murphy (2000), Particle analysis by laser mass spectrometry
1629 WB-57F instrument overview, *Aerosol Sci. Technol.*, *33*(1-2), 153-169.

1630
1631 Tsimpidi, A. P., V. A. Karydis, M. Zavala, W. Lei, L. Molina, I. M. Ulbrich, J. L. Jimenez, and S. N.
1632 Pandis (2010), Evaluation of the volatility basis-set approach for the simulation of organic aerosol
1633 formation in the Mexico City metropolitan area, *Atmos. Chem. Phys.*, *10*(2), 525-546.

1634
1635 Turpin, B. J., J. J. Huntzicker, S. M. Larson, and G. R. Cass (1991), LOS-ANGELES SUMMER
1636 MIDDAY PARTICULATE CARBON - PRIMARY AND SECONDARY AEROSOL, *Environ. Sci.*
1637 *Technol.*, *25*(10), 1788-1793.

1638
1639 Ulbrich, I. M., M. R. Canagaratna, Q. Zhang, D. R. Worsnop, and J. L. Jimenez (2009), Interpretation of
1640 organic components from Positive Matrix Factorization of aerosol mass spectrometric data, *Atmos. Chem.*
1641 *Phys.*, *9*(9), 2891-2918.

1642
1643 Ulrickson, B. L., and C. F. Mass (1990), Numerical investigation of mesoscale circulations over the los-
1644 angeles basin. 2. Synoptic influences and pollutant transport, *Mon. Weather Rev.*, *118*(10), 2162-2184.

1645
1646 Veres, P. R., et al. (2011), Evidence of rapid production of organic acids in an urban air mass, *Geophys.*
1647 *Res. Lett.*, *38*, L17807.

1648
1649 Warneke, C., J. A. de Gouw, J. S. Holloway, J. Peischl, T. B. Ryerson, E. Atlas, D. Blake, M. Trainer,
1650 and D. D. Parrish (2012), Multiyear trends in volatile organic compounds in Los Angeles, California:
1651 Five decades of decreasing emissions, *J. Geophys. Res.*, *117*, D00V17.

1652
1653 Warneke, C., et al. (2007), Determination of urban volatile organic compound emission ratios and
1654 comparison with an emissions database, *J. Geophys. Res.-Atmos.*, *112*(D10), D10S47.

1655
1656 Washenfelder, R. A., et al. (2011), The glyoxal budget and its contribution to organic aerosol for Los
1657 Angeles, California, during CalNex 2010, *J. Geophys. Res.-Atmos.*, *116*, D00V02.

1658
1659 Watson, J. G. (2002), Visibility: Science and regulation, *J. Air Waste Manage. Assoc.*, *52*(6), 628-713.

1660
1661 Williams, B. J., A. H. Goldstein, N. M. Kreisberg, S. V. Hering, D. R. Worsnop, I. M. Ulbrich, K. S.
1662 Docherty, and J. L. Jimenez (2010), Major components of atmospheric organic aerosol in southern
1663 California as determined by hourly measurements of source marker compounds, *Atmos. Chem. Phys.*,
1664 *10*(23), 11577-11603.

1665
1666 Wonaschutz, A., S. P. Hersey, A. Sorooshian, J. S. Craven, A. R. Metcalf, R. C. Flagan, and J. H.
1667 Seinfeld (2011), Impact of a large wildfire on water-soluble organic aerosol in a major urban area: the
1668 2009 Station Fire in Los Angeles County, *Atmos. Chem. Phys.*, *11*(16), 8257-8270.

1669
1670 Wood, E. C., et al. (2010), Investigation of the correlation between odd oxygen and secondary organic
1671 aerosol in Mexico City and Houston, *Atmos. Chem. Phys.*, *10*(18), 8947-8968.

1672
1673 Worton, D. R., N. M. Kreisberg, G. Isaacman, A. P. Teng, C. McNeish, T. Górecki, S. V. Hering, and A.
1674 H. Goldstein (2012), Thermal Desorption Comprehensive Two-Dimensional Gas Chromatography: An
1675 Improved Instrument for In-Situ Speciated Measurements of Organic Aerosols, *Aerosol Sci. Technol.*,
1676 *46*(4), 380-393.

1677
1678 Young, C. J., et al. (2012), Vertically Resolved Measurements of Nighttime Radical Reservoirs; in Los
1679 Angeles and Their Contribution to the Urban Radical Budget, *Environ. Sci. Technol.*, *46*(20), 10965-
1680 10973.

1681
1682 Zelenyuk, A., Y. Cai, L. Chieffo, and D. Imre (2005), High precision density measurements of single
1683 particles: The density of metastable phases, *Aerosol Sci. Technol.*, *39*(10), 972-986.

1684
1685 Zhang, Q., J. L. Jimenez, D. R. Worsnop, and M. Canagaratna (2007a), A case study of urban particle
1686 acidity and its influence on secondary organic aerosol, *Environ. Sci. Technol.*, *41*(9), 3213-3219.

1687

1688 Zhang, Q., J. L. Jimenez, M. R. Canagaratna, I. M. Ulbrich, N. L. Ng, D. R. Worsnop, and Y. L. Sun
1689 (2011), Understanding atmospheric organic aerosols via factor analysis of aerosol mass spectrometry: a
1690 review, *Anal. Bioanal. Chem.*, *401*(10), 3045-3067.

1691
1692 Zhang, Q., et al. (2007b), Ubiquity and Dominance of Oxygenated Species in Organic Aerosols in
1693 Anthropogenically—Influenced Northern Hemisphere Mid-latitudes. , *Geophys. Res. Lett.*, *34*, L13801.

1694
1695 Zhang, X., A. Hecobian, M. Zheng, N. H. Frank, and R. J. Weber (2010), Biomass burning impact on
1696 PM(2.5) over the southeastern US during 2007: integrating chemically speciated FRM filter
1697 measurements, MODIS fire counts and PMF analysis, *Atmos. Chem. Phys.*, *10*(14), 6839-6853.

1698
1699 Zhang, X., J. Liu, E. T. Parker, P. L. Hayes, J. L. Jimenez, J. A. de Gouw, J. H. Flynn, N. Grossberg, B.
1700 L. Lefer, and R. J. Weber (2012), On the gas-particle partitioning of soluble organic aerosol in two urban
1701 atmospheres with contrasting emissions: 1. Bulk water-soluble organic carbon, *J. Geophys. Res.*, *117*,
1702 D00V16.

1703
1704 Zhuang, H., C. K. Chan, M. Fang, and A. S. Wexler (1999), Formation of nitrate and non-sea-salt sulfate
1705 on coarse particles, *Atmos. Environ.*, *33*(26), 4223-4233.

1706
1707
1708

1709 8. Figure Captions

1710 **Figure 1:** (A) CO concentration. (B) The non-refractory aerosol concentrations sampled by the
1711 AMS. The measured species are organics (OA), nitrate (NO₃), sulfate (SO₄), ammonium (NH₄),
1712 and non-refractory chloride (nrCl). The elemental carbon (EC) concentration was measured *in-*
1713 *situ* by a Sunset analyzer. For completeness, the EC data includes occasional periods when a
1714 PM₁ cyclone was used instead of a PM_{2.5} cyclone (6/12 – 6/16). (C) Refractory aerosol mass
1715 concentrations as measured by XRF (rCl: Refractory Chloride). (D) Particle type volume
1716 concentrations measured by the PALMS for PM₁, and (E) for particles between 1 and 2.5 μm
1717 diameters. All size cuts are aerodynamic diameters, and the PALMS data have been converted
1718 from geometric diameters (1 μm aerodynamic diameter = 0.784 μm geometric diameter).

1719 **Figure 2:** (A) Diurnal profiles for the non-refractory PM₁ mass concentrations (from AMS) and
1720 for EC (from Sunset Analyzer). (B) Diurnal cycles of CO and photochemical age. The
1721 photochemical age is determined using the method of Parrish et al. [2007] and the ratio of 1,2,4-
1722 trimethylbenzene to benzene (solid line), or following Kleinman et al. [2008] and defining the
1723 photochemical age as $-\log_{10}(\text{NO}_x/\text{NO}_y)$ (dashed line). (C) Average PM₁ mass concentration (in
1724 μg/m³) for the ground site (5/15 00:00 – 6/16 00:00) including both refractory and non-refractory
1725 components. Concentrations of mineral dust, metals, and refractory chloride (rCl) were
1726 determined from XRF. The sodium concentration is estimated from PALMS sea salt volume
1727 concentrations using a NaNO₃ density of 2.1 g cm⁻³ [Zelenyuk et al., 2005] and a sodium to sea
1728 salt mass ratio of 0.308 [Hall et al., 1998]. All error bars indicate standard errors of the means.

1729 **Figure 3:** Average volume concentration (in μm³ cm⁻³) of the different PALMS particle types
1730 for (A) PM₁ and (B) particles between 1 and 2.5 μm diameters at the Pasadena ground site
1731 during CalNex. Size ranges correspond to aerodynamic diameters.

1732 **Figure 4:** (A) Mass spectra for the five factors identified in the PMF analysis. The mass spectra
1733 are colored by the ion type to indicate the contribution of each ion type to the mass spectra. For
1734 clarity spectra are shown only to *m/z* 150, although spectra were measured up to *m/z* 204. (B)
1735 Time series of the PMF factors.

1736 **Figure 5:** (A) Diurnal profiles for the PMF components. Shaded regions indicate uncertainties
1737 calculated using bootstrapping [Ulbrich et al., 2009]. (B) Diurnal profiles of the PMF
1738 components by percent mass. (C) Diurnal profiles of the oxygen-to-carbon and hydrogen-to-
1739 carbon elemental ratios for the total OA mass. Error bars indicate the standard error of the mean.
1740 (D) The campaign average contribution of each PMF component to the PM₁ organic aerosol
1741 mass concentration.

1742 **Figure 6:** Van Krevelen diagram for Pasadena during the CalNex campaign (red crosses) and for
1743 Riverside, CA during the SOAR-1 campaign (blue crosses). The PMF factors identified for
1744 Pasadena (hexagons) and Riverside (squares) are shown as well. The linear regression analyses
1745 correspond to the total OA data.

1746 **Figure 7:** (A) HOA versus EC concentration measured *in-situ* by the Sunset analyzer. Fits are
1747 shown for the entire plot (solid line) and for only data points corresponding to high $\text{NO}_y/\Delta\text{CO}$
1748 ratios (dashed line). The gray shaded regions indicate the range of expected slopes for gasoline
1749 and diesel vehicles based on the reported emission ratios of Ban-Weiss et al. [2008b] and a 1.34
1750 OM:OC. (B) The sum of HOA and CIOA versus CO concentration. Linear fits are shown for
1751 data points corresponding to high HOA (solid line) and high CIOA concentrations (dashed line).

1752 **Figure 8:** The evolution of $\text{OA}/\Delta\text{CO}$ versus photochemical age for Pasadena during CalNex. The
1753 measured ratios are averaged into 25 bins according to photochemical age. The enhanced CO
1754 (ΔCO) is the ambient CO minus the estimated background CO (105 ppb). The standard error of
1755 $\text{OA}/\Delta\text{CO}$ is smaller than the size of the data point, and therefore is not plotted. Instead error bars
1756 representing the uncertainty in the ratio due to an uncertainty of ± 20 ppbv in background CO are
1757 shown. Photochemical age is determined by two methods: (1) Following Parrish et al. [2007] and
1758 using the ratio of 1,2,4-trimethylbenzene to benzene (green); (2) Following Kleinman et al.
1759 [2008] and defining the photochemical age as $-\log_{10}(\text{NO}_x/\text{NO}_y)$ (red). All photochemical ages
1760 have been standardized to an OH radical concentration 1.5×10^6 molec. cm^{-3} , and the
1761 corresponding OH exposure for a given photochemical age is shown on the top axis. The gray
1762 region is adapted from DeCarlo et al. [2010] and represents the evolution of $\text{OA}/\Delta\text{CO}$ observed
1763 in the northeastern United States and the Mexico City area. The black horizontal line is the ratio
1764 of (HOA + CIOA + 'background LVOOA') to ΔCO . (Inset) Evolution of the PMF component
1765 concentrations normalized to ΔCO versus photochemical age. Data is binned according to
1766 photochemical age.

1767 **Figure 9:** Time series for OOA (the sum of SV-OOA and LV-OOA), and O_x (the sum of O_3 and
1768 NO_2). (Inset) Scatter plot of OOA versus O_x with linear fit and colored by time-of-day. The best-
1769 fit slope is 0.146 ($R^2 = 0.53$). A fixed x-intercept of 15 ppmv O_x is used in the fitting procedure
1770 identical to previously published work.

1771 **Figure 10:** Diurnal profiles, calculated using means, of HOA, EC, rBC, CIOA, CO, and Benzene
1772 for weekdays and Sundays during CalNex.

1773 **Figure 11:** (A) The evolution of $\text{OA}/\Delta\text{CO}$ versus photochemical age for Pasadena during
1774 CalNex separated by day of the week. The enhanced CO (ΔCO) is the ambient CO minus the
1775 estimated background CO (105 ppb). Error bars indicate the standard errors. Photochemical age
1776 is determined using the method of Parrish et al. [2007]. (B) Also shown is the analogous plot for
1777 OOA with the linear ODR fits of the data.

1778 **Figure 12:** (A) Size distributions measured by the AMS. Also shown is rBC measured by the
1779 SP-AMS. Note: The AMS size distributions have a gradual cut of approximately PM_{10} and can
1780 have a tail due to slow evaporating particles and should be interpreted accordingly. (B) The ratio
1781 of rCl to Mg plotted versus particle size. Ratio is calculated using mass concentrations from XRF
1782 for 5/20 00:00 to 5/25 00:00. (C) Distribution for refractory components measured by XRF. (D)

1783 PM₁ size distributions by percent mass. The XRF data are calculated by interpolating the original
1784 data to provide sufficient data points to create the stacked plot. Note: rBC concentrations below
1785 100 nm may be underestimated due to instrument limitations. Sodium is estimated from the
1786 PALMS data as described in the Figure 2 caption. **(E)** Distributions of particle types measured
1787 by the PALMS. Volume distributions determined from the SMPS and WLOPC are shown as
1788 well. For the size range overlap of the SMPS and WLOPC each particle type has two data points
1789 in each size bin, which is due to mapping the PALMS particle fractions onto the two sizing
1790 instruments.

1791 **Figure 13:** **(A)** Scatter plot of the measured ammonium versus ‘NH₄⁺ predicted’, which is
1792 calculated using the concentrations of nitrate, sulfate, and chloride, as well as assuming full
1793 neutralization by ammonium (all data from AMS). **(B)** Histogram for the ratios of the measured
1794 ammonium to the NH₄⁺ predicted. A Gaussian distribution is shown in the histogram for
1795 reference and is generated using the standard deviation of the data. **(C)** Scatter plot of the
1796 measured-to-predicted ratios versus the ratios of sodium to the total cations (ammonium plus
1797 sodium). Sodium is estimated from the PALMS sea salt concentrations as described in the Figure
1798 2 caption.

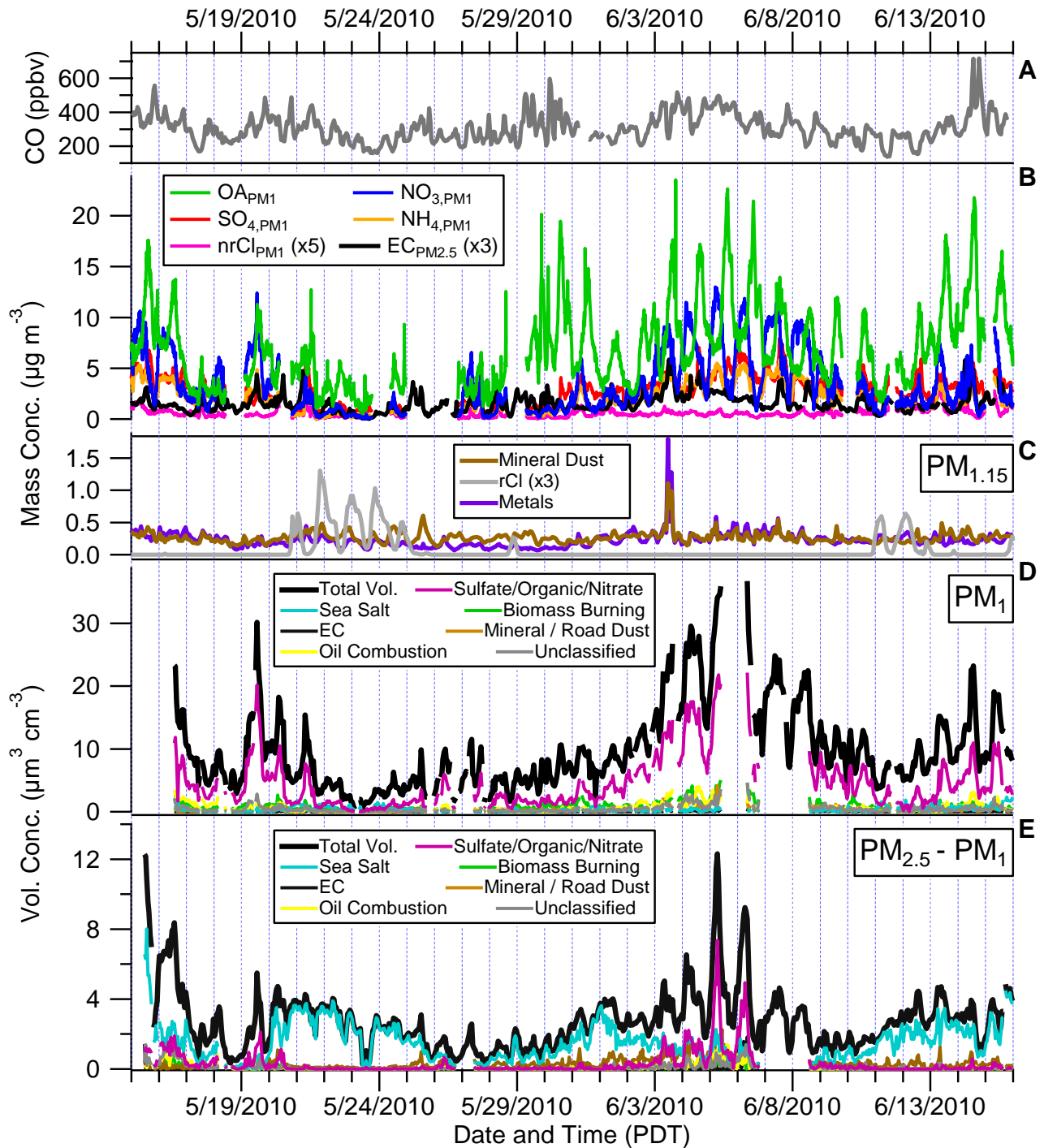


Figure 1: (A) CO concentration. (B) The non-refractory aerosol concentrations sampled by the AMS. The measured species are organics (OA), nitrate (NO_3), sulfate (SO_4), ammonium (NH_4), and non-refractory chloride (nrCl). The elemental carbon (EC) concentration was measured *in-situ* by a Sunset analyzer. For completeness, the EC data includes occasional periods when a PM_1 cyclone was used instead of a $\text{PM}_{2.5}$ cyclone (6/12 – 6/16). (C) Refractory aerosol mass concentrations as measured by XRF (rCl: Refractory Chloride). (D) Particle type volume concentrations measured by the PALMS for PM_1 , and (E) for particles between 1 and 2.5 μm diameters. All size cuts are aerodynamic diameters, and the PALMS data have been converted from geometric diameters (1 μm aerodynamic diameter = 0.784 μm geometric diameter).

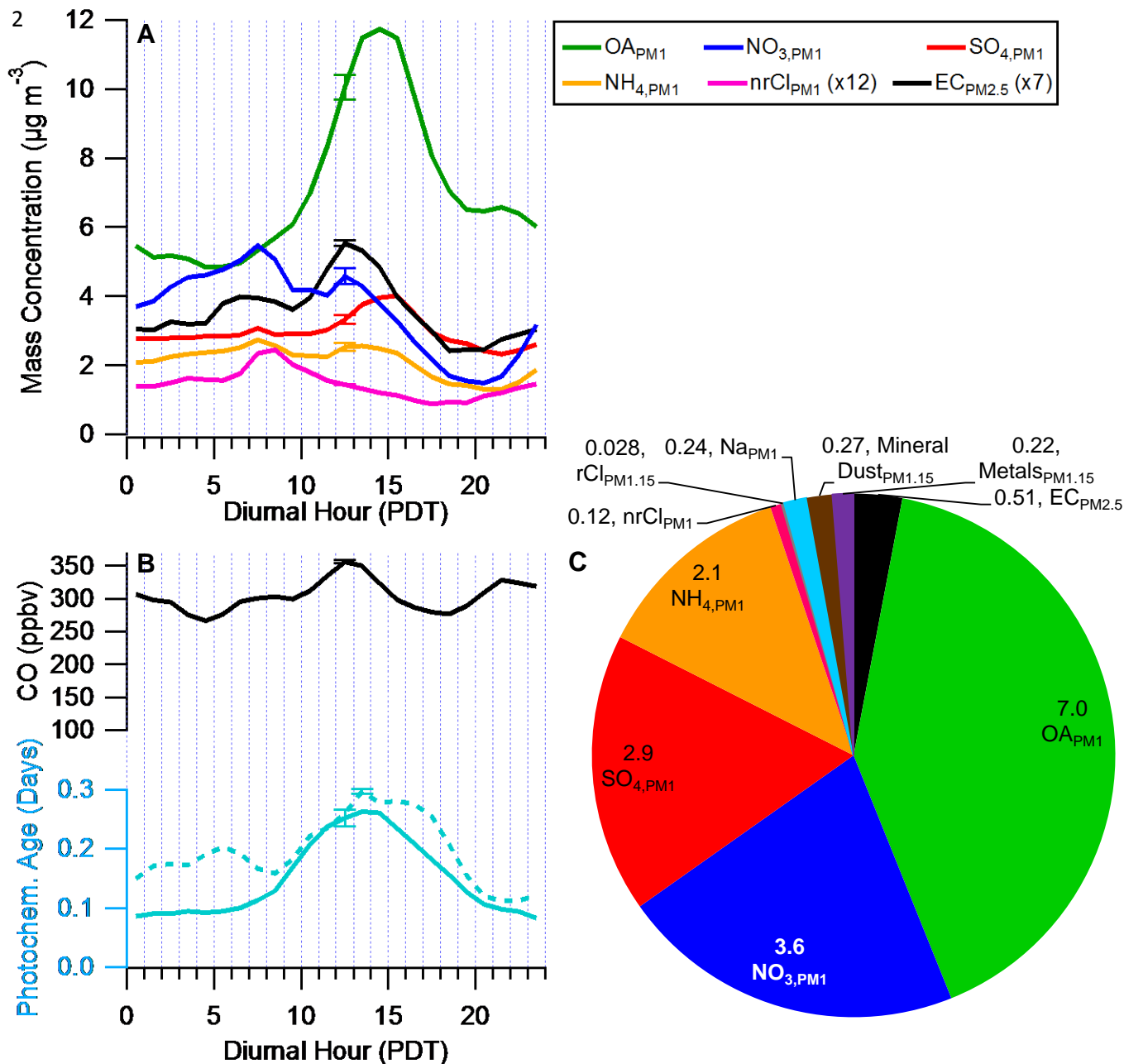


Figure 2: (A) Diurnal profiles for the non-refractory PM₁ mass concentrations (from AMS) and for EC (from Sunset Analyzer). (B) Diurnal cycles of CO and photochemical age. The photochemical age is determined using the method of Parrish et al. [2007] and the ratio of 1,2,4-trimethylbenzene to benzene (solid line), or following Kleinman et al. [2008] and defining the photochemical age as $-\log_{10}(\text{NO}_x/\text{NO}_y)$ (dashed line). (C) Average PM₁ mass concentration (in $\mu\text{g}/\text{m}^3$) for the ground site (5/15 00:00 – 6/16 00:00) including both refractory and non-refractory components. Concentrations of mineral dust, metals, and refractory chloride (rCl) were determined from XRF. The sodium concentration is estimated from PALMS sea salt volume concentrations using a NaNO_3 density of 2.1 g cm^{-3} [Zelenyuk et al., 2005] and a sodium to sea salt mass ratio of 0.308 [Hall et al., 1998]. All error bars indicate standard errors of the means.

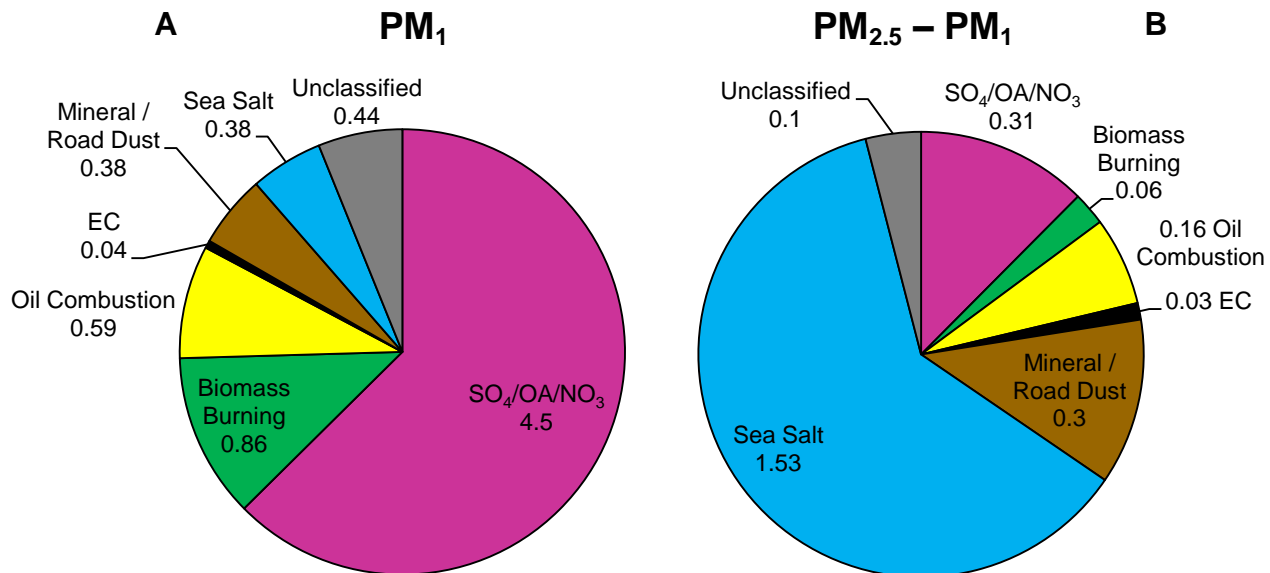


Figure 3: Average volume concentration (in $\mu m^3 cm^{-3}$) of the different PALMS particle types for (A) PM_1 and (B) particles between 1 and 2.5 μm diameters at the Pasadena ground site during CalNex. Size ranges correspond to aerodynamic diameters.

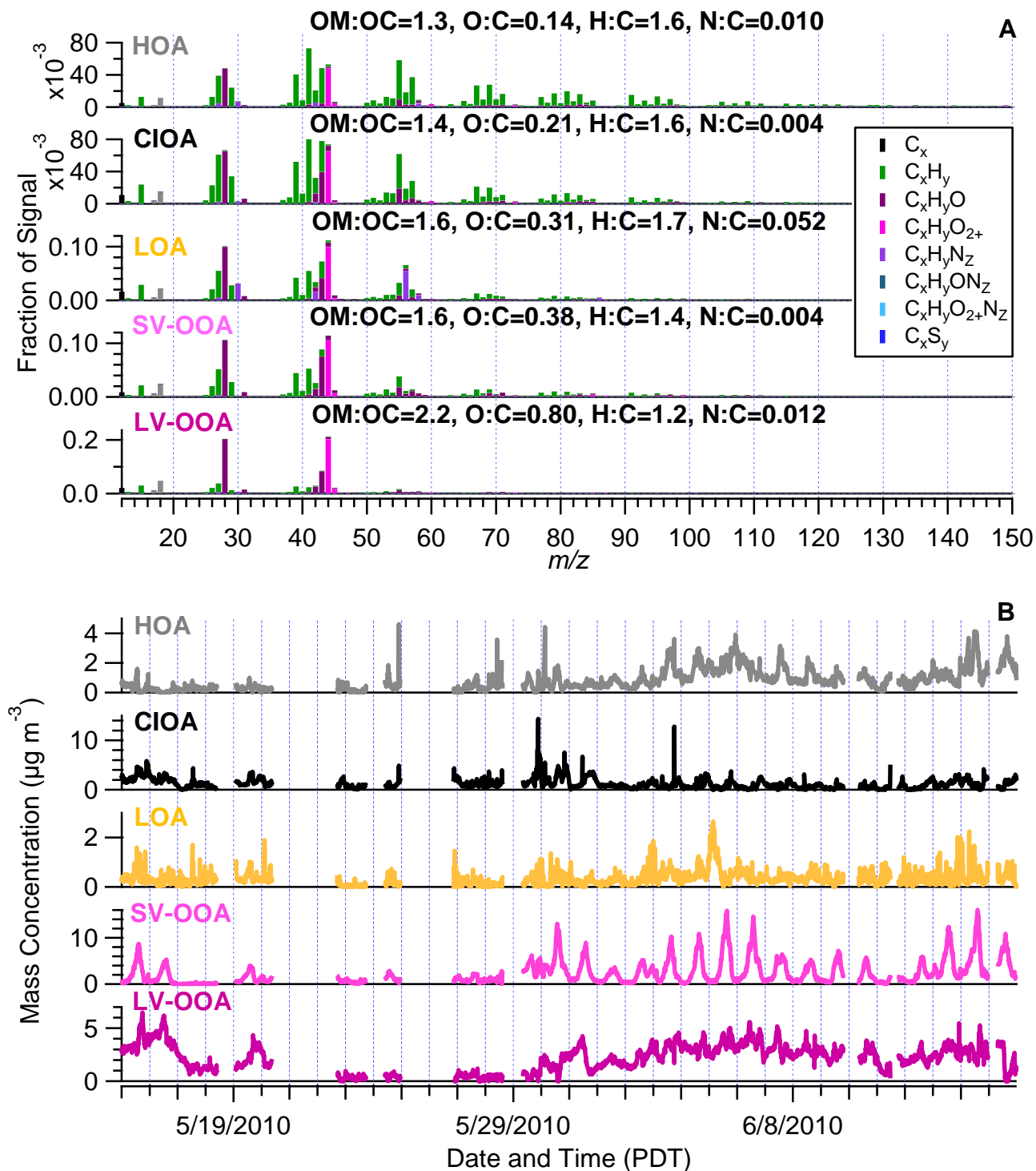


Figure 4: (A) Mass spectra for the five factors identified in the PMF analysis. The mass spectra are colored by the ion type to indicate the contribution of each ion type to the mass spectra. For clarity spectra are shown only to m/z 150, although spectra were measured up to m/z 204. (B) Time series of the PMF factors.

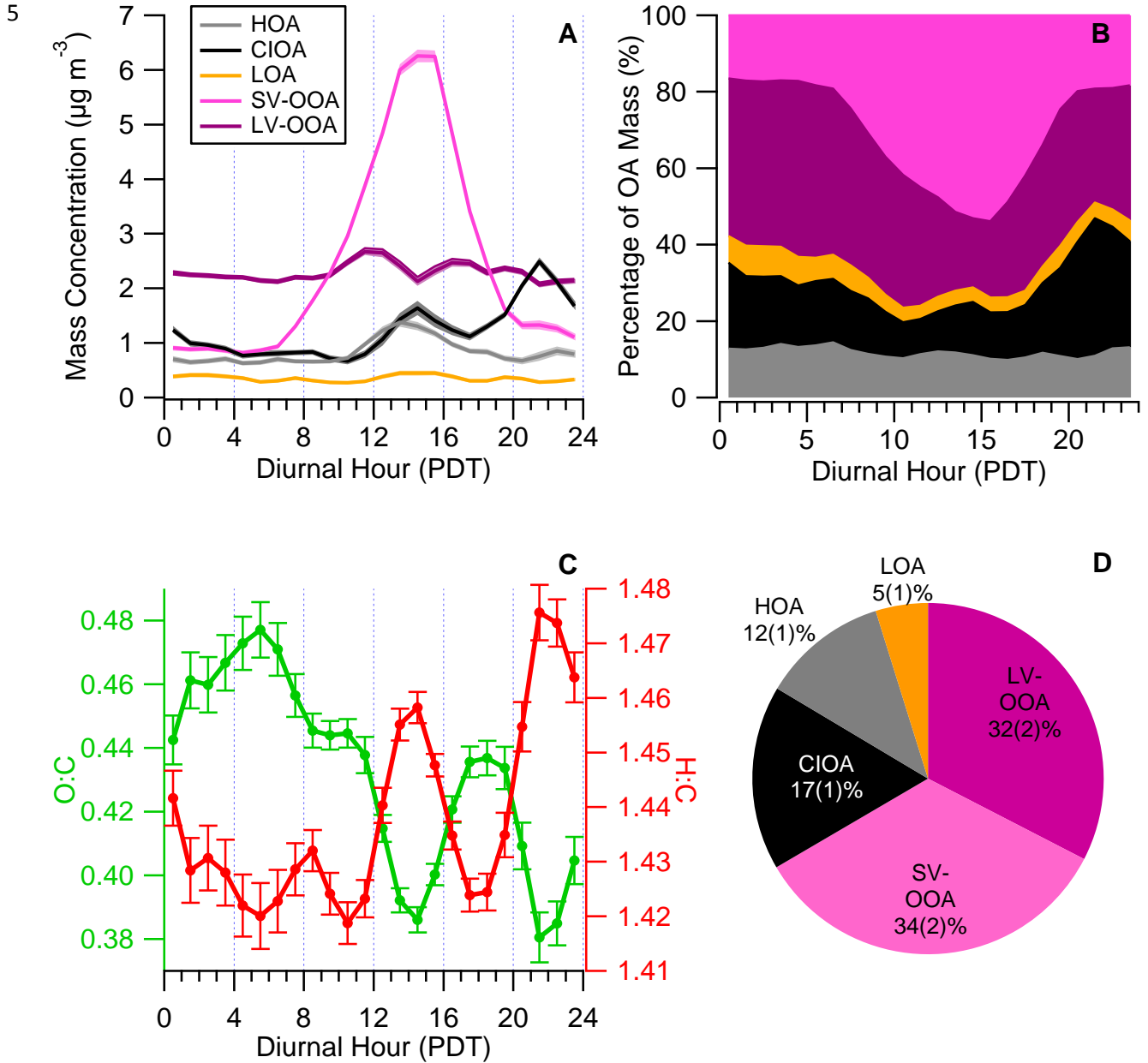


Figure 5: (A) Diurnal profiles for the PMF components. Shaded regions indicate uncertainties calculated using bootstrapping [Ulbrich *et al.*, 2009]. (B) Diurnal profiles of the PMF components by percent mass. (C) Diurnal profiles of the oxygen-to-carbon and hydrogen-to-carbon elemental ratios for the total OA mass. Error bars indicate the standard error of the mean. (D) The campaign average contribution of each PMF component to the PM_{10} organic aerosol mass concentration.

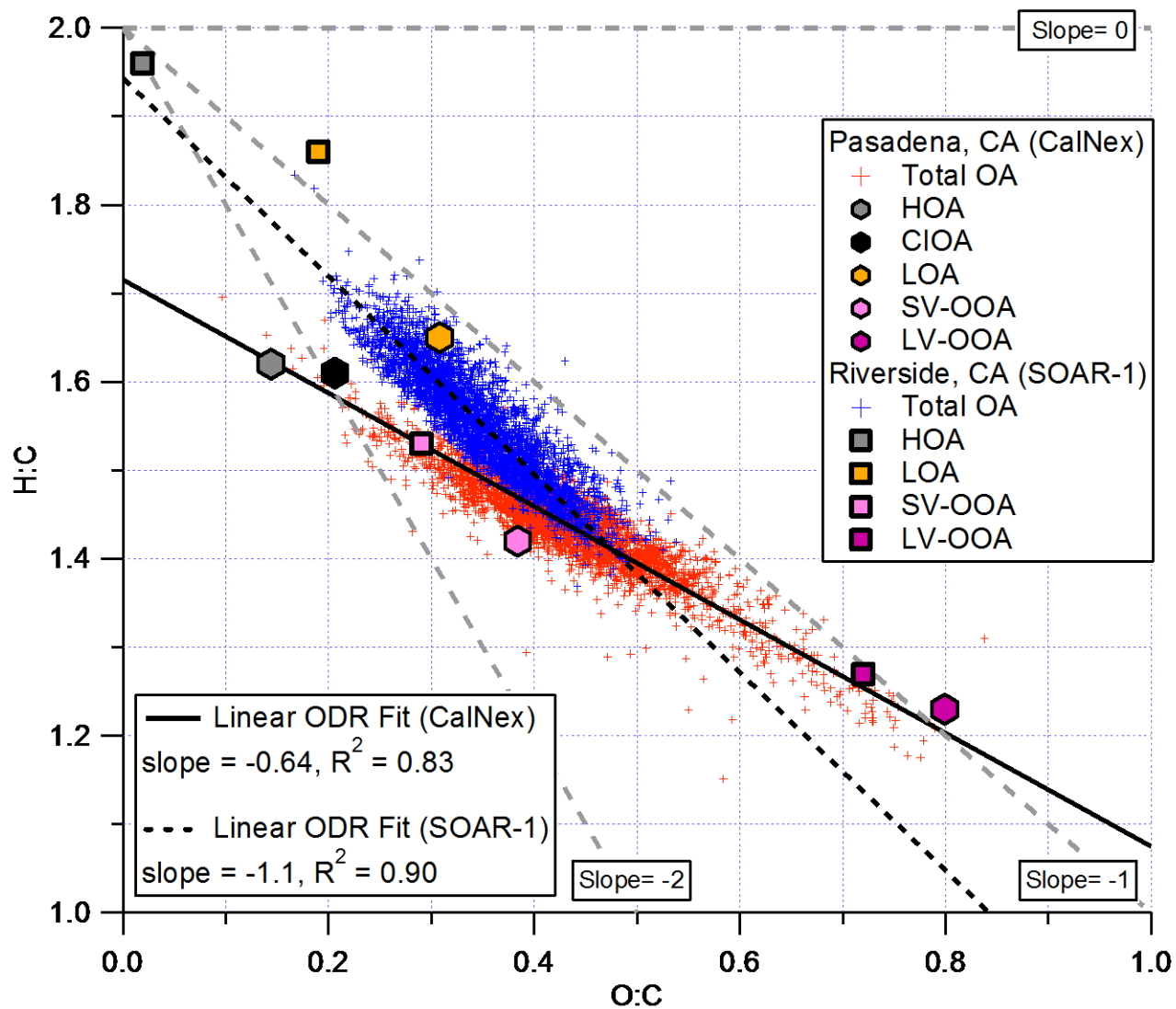


Figure 6: Van Krevelen diagram for Pasadena during the CalNex campaign (red crosses) and for Riverside, CA during the SOAR-1 campaign (blue crosses). The PMF factors identified for Pasadena (hexagons) and Riverside (squares) are shown as well. The linear regression analyses correspond to the total OA data.

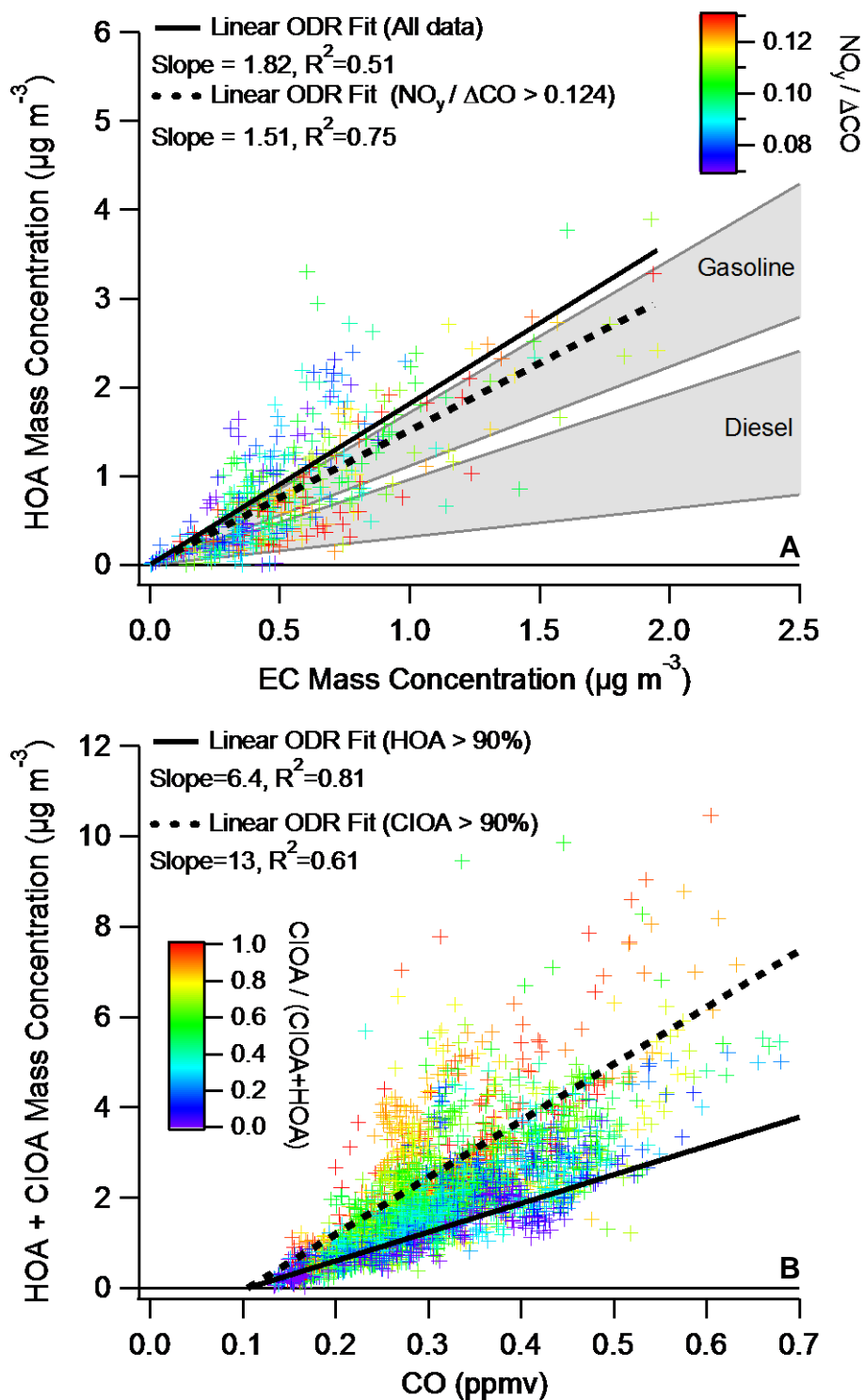


Figure 7: (A) HOA versus EC concentration measured *in-situ* by the Sunset analyzer. Fits are shown for the entire plot (solid line) and for only data points corresponding to high $\text{NO}_y/\Delta\text{CO}$ ratios (dashed line). The gray shaded regions indicate the range of expected slopes for gasoline and diesel vehicles based on the reported emission ratios of Ban-Weiss et al. [2008b] and a 1.34 OM:OC. (B) The sum of HOA and CIOA versus CO concentration. Linear fits are shown for data points corresponding to high HOA (solid line) and high CIOA concentrations (dashed line).

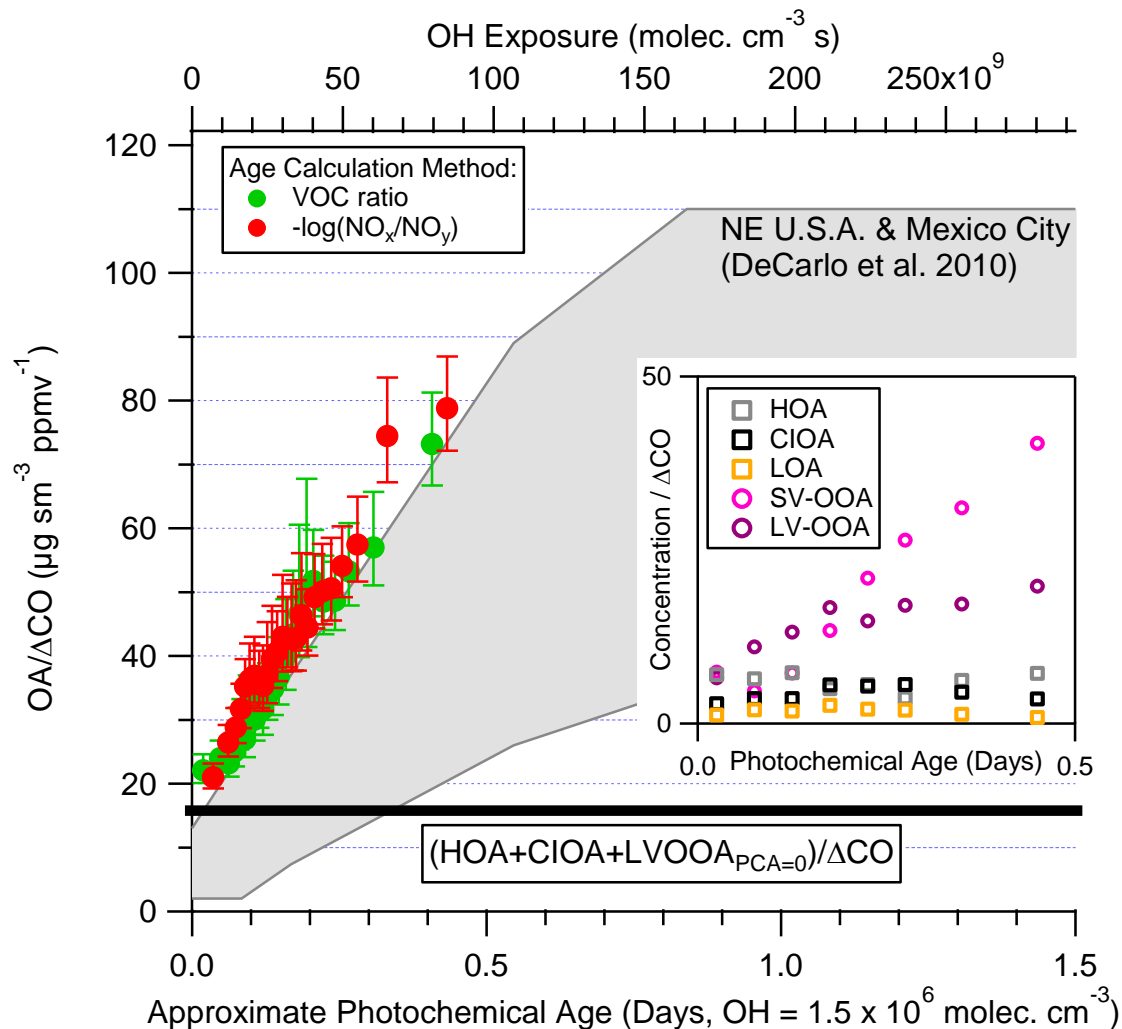


Figure 8: The evolution of $OA/\Delta CO$ versus photochemical age for Pasadena during CalNex. The measured ratios are averaged into 25 bins according to photochemical age. The enhanced CO (ΔCO) is the ambient CO minus the estimated background CO (105 ppb). The standard error of $OA/\Delta CO$ is smaller than the size of the data point, and therefore is not plotted. Instead error bars representing the uncertainty in the ratio due to an uncertainty of ± 20 ppbv in background CO are shown. Photochemical age is determined by two methods: (1) Following Parrish et al. [2007] and using the ratio of 1,2,4-trimethylbenzene to benzene (green); (2) Following Kleinman et al. [2008] and defining the photochemical age as $-\log_{10}(NO_x/NO_y)$ (red). All photochemical ages have been standardized to an OH radical concentration 1.5×10^6 molec. cm^{-3} , and the corresponding OH exposure for a given photochemical age is shown on the top axis. The gray region is adapted from DeCarlo et al. [2010] and represents the evolution of $OA/\Delta CO$ observed in the northeastern United States and the Mexico City area. The black horizontal line is the ratio of (HOA + CIOA + ‘background LVOOA’) to ΔCO . (**Inset**) Evolution of the PMF component concentrations normalized to ΔCO versus photochemical age. Data is binned according to photochemical age.

9

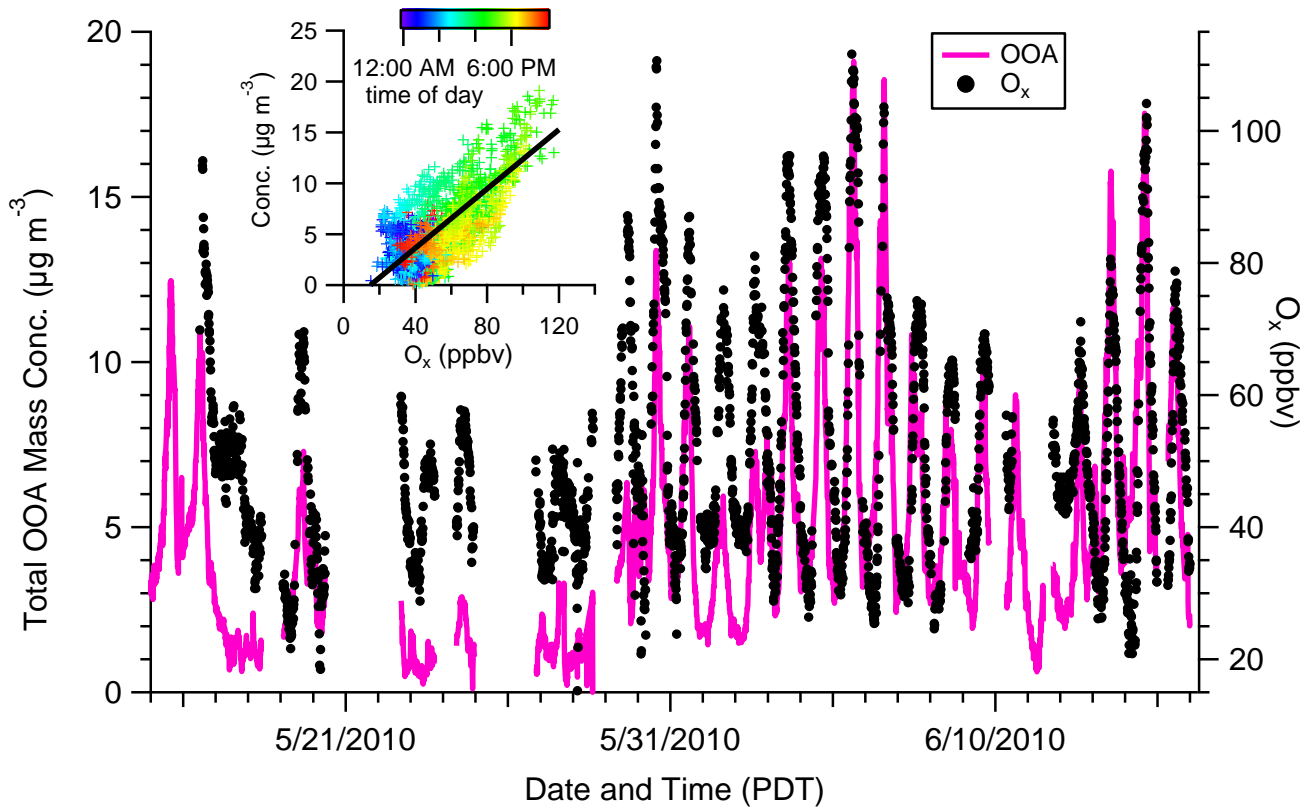


Figure 9: Time series for OOA (the sum of SV-OOA and LV-OOA), and O_x (the sum of O_3 and NO_2). (**Inset**) Scatter plot of OOA versus O_x with linear fit and colored by time-of-day. The best-fit slope is 0.146 ($R^2 = 0.53$). A fixed x-intercept of 15 ppmv O_x is used in the fitting procedure identical to previously published work.

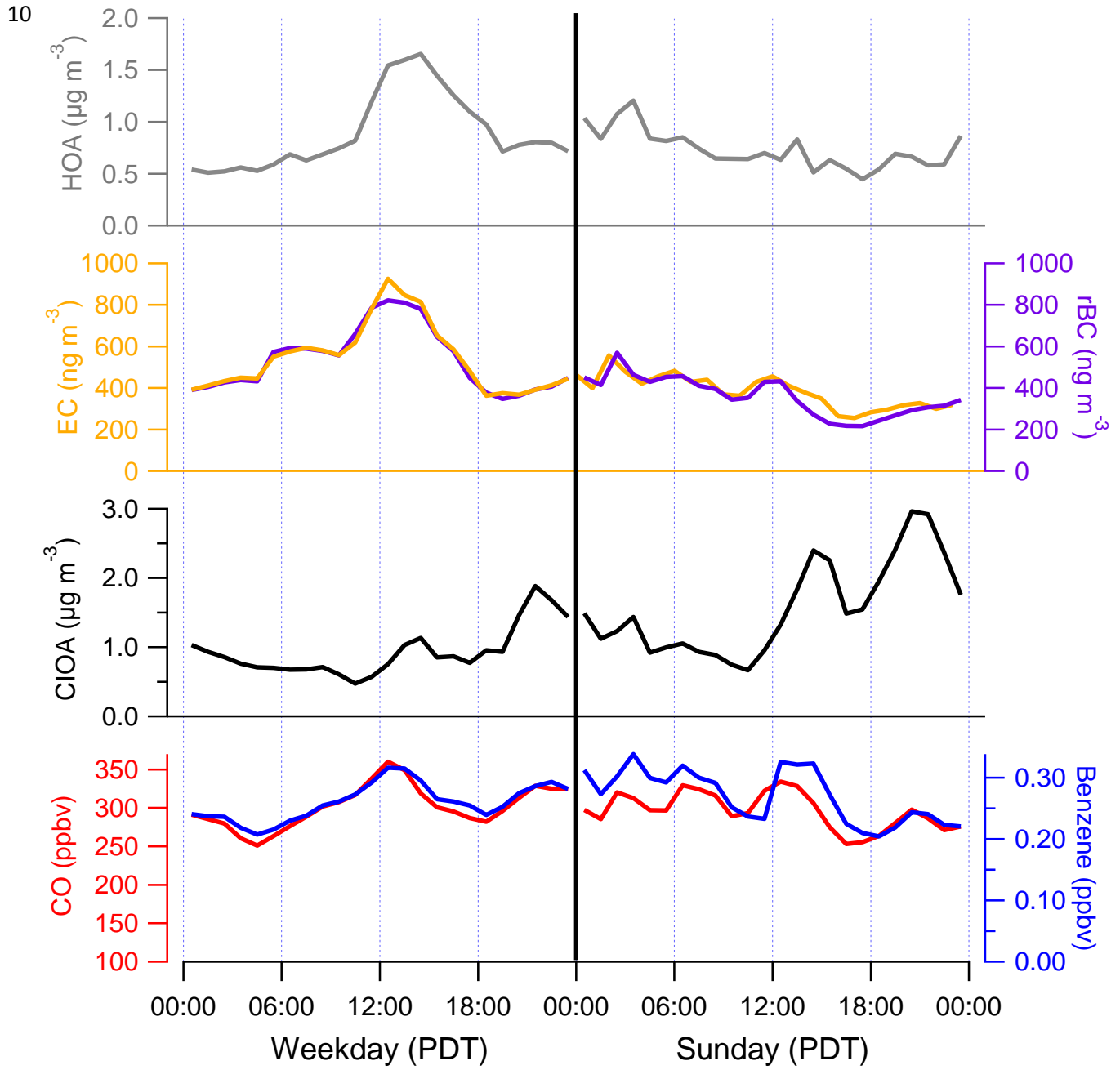


Figure 10: Diurnal profiles, calculated using means, of HOA, EC, rBC, CIOA, CO, and Benzene for weekdays and Sundays during CalNex.

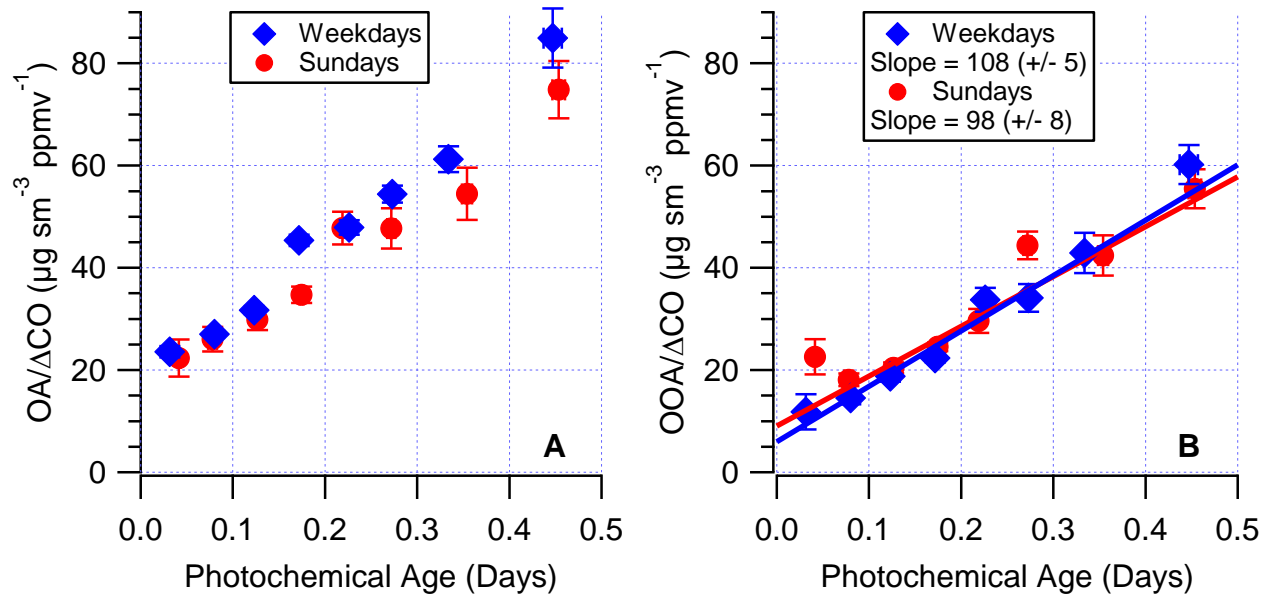


Figure 11: (A) The evolution of $\text{OA}/\Delta\text{CO}$ versus photochemical age for Pasadena during CalNex separated by day of the week. The enhanced CO (ΔCO) is the ambient CO minus the estimated background CO (105 ppb). Error bars indicate the standard errors. Photochemical age is determined using the method of Parrish et al. [2007]. (B) Also shown is the analogous plot for OOA with the linear ODR fits of the data.

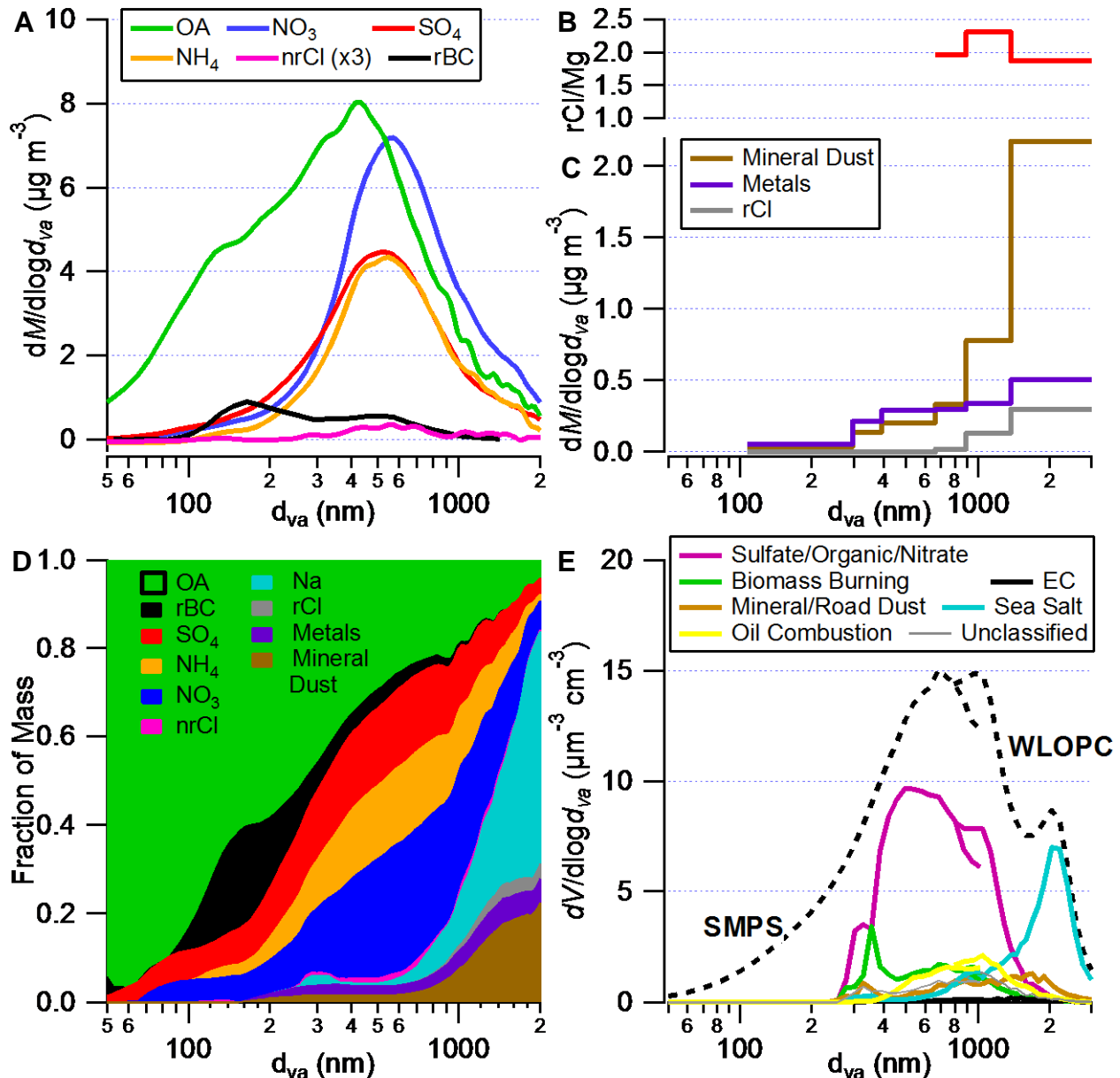


Figure 12: (A) Size distributions measured by the AMS. Also shown is rBC measured by the SP-AMS. Note: The AMS size distributions have a gradual cut of approximately PM_{10} and can have a tail due to slow evaporating particles and should be interpreted accordingly. (B) The ratio of rCl to Mg plotted versus particle size. Ratio is calculated using mass concentrations from XRF for 5/20 00:00 to 5/25 00:00. (C) Distribution for refractory components measured by XRF. (D) PM_{10} size distributions by percent mass. The XRF data are calculated by interpolating the original data to provide sufficient data points to create the stacked plot. Note: rBC concentrations below 100 nm may be underestimated due to instrument limitations. Sodium is estimated from the PALMS data as described in the Figure 2 caption. (E) Distributions of particle types measured by the PALMS. Volume distributions determined from the SMPS and WLOPC are shown as well. For the size range overlap of the SMPS and WLOPC each particle type has two data points in each size bin, which is due to mapping the PALMS particle fractions onto the two sizing instruments.

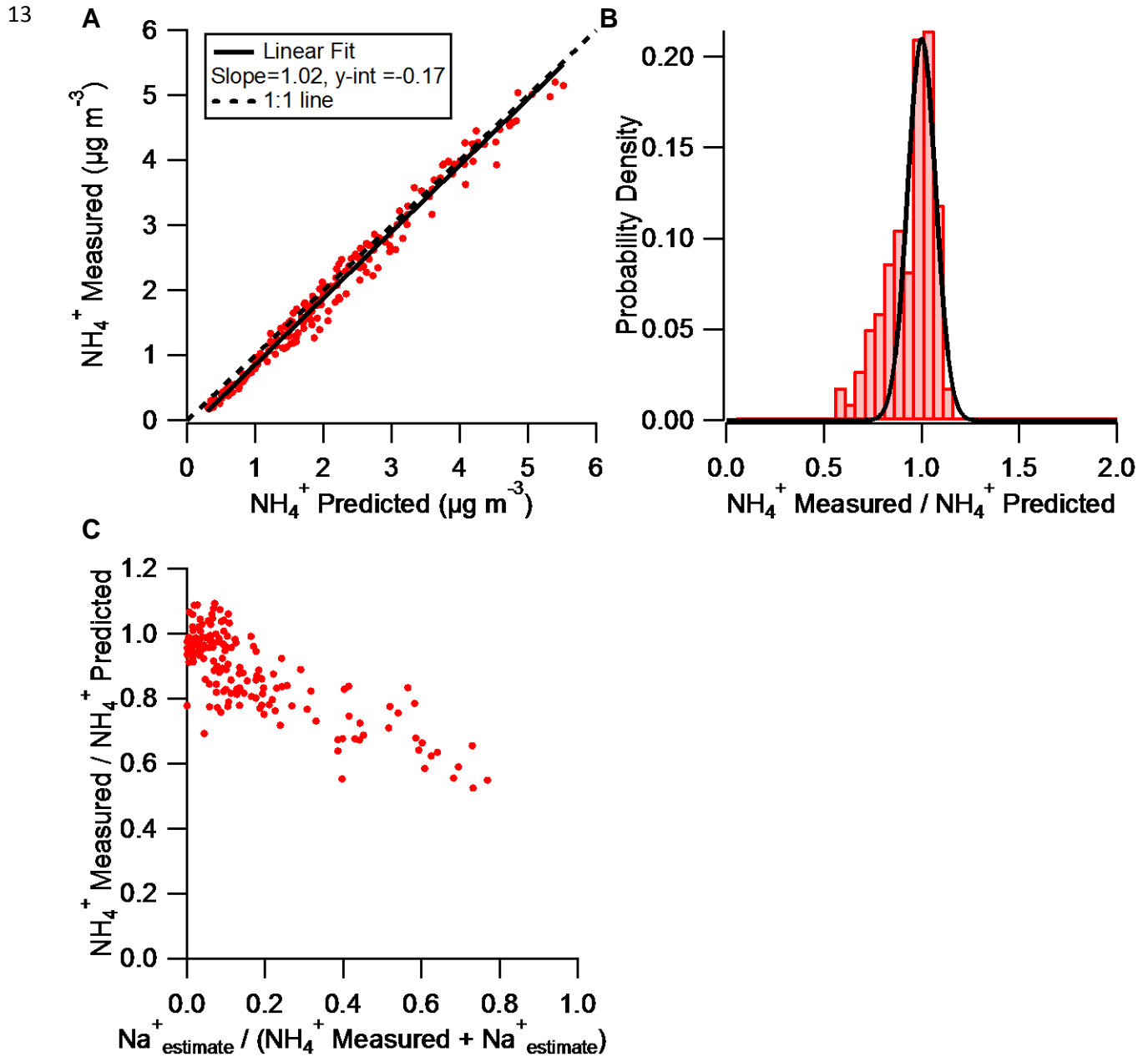


Figure 13: (A) Scatter plot of the measured ammonium versus ‘ NH_4^+ predicted’, which is calculated using the concentrations of nitrate, sulfate, and chloride, as well as assuming full neutralization by ammonium (all data from AMS). (B) Histogram for the ratios of the measured ammonium to the NH_4^+ predicted. A Gaussian distribution is shown in the histogram for reference and is generated using the standard deviation of the data. (C) Scatter plot of the measured-to-predicted ratios versus the ratios of sodium to the total cations (ammonium plus sodium). Sodium is estimated from the PALMS sea salt concentrations as described in the Figure 2 caption.

Supporting Material for:

Organic Aerosol Composition and Sources in Pasadena, California during the 2010 CalNex Campaign

P. L. Hayes^{1,2}, A. M. Ortega^{1,3}, M. J. Cubison^{1,2}, K. D. Froyd^{1,4}, Y. Zhao⁵, S. S. Cliff⁵, W. W. Hu^{1,6}, D. W. Toohey³, J. H. Flynn⁷, B. L. Lefer⁷, N. Grossberg⁷, S. Alvarez⁷, B. Rappenglück⁷, J. W. Taylor⁸, J. D. Allan^{8,9}, J. S. Holloway^{1,4}, J. B. Gilman^{1,4}, W. C. Kuster⁴, J. A. de Gouw^{1,4}, P. Massoli¹⁰, X. Zhang¹¹, J. Liu¹¹, R. J. Weber¹¹, A. L. Corrigan¹², L. M. Russell¹², G. Isaacman¹³, D. R. Worton^{13,14}, N. M. Kreisberg¹⁴, A. H. Goldstein¹³, R. Thalman^{1,2}, E. M. Waxman^{1,2}, R. Volkamer^{1,2}, Y. H. Lin¹⁵, J. D. Surratt¹⁵, T. E. Kleindienst¹⁶, J. H. Offenberg¹⁶, S. Dusanter^{17,18,19}, S. Griffith¹⁷, P. S. Stevens¹⁷, J. Brioude^{1,4}, W. M. Angevine^{1,4}, J. L. Jimenez^{1,2}

(1) Cooperative Institute for Research in the Environmental Sciences (CIRES), Univ. of Colorado, Boulder, CO, USA

(2) Dept. of Chemistry and Biochemistry, Univ. of Colorado, Boulder, CO, USA

(3) Dept. of Atmospheric and Oceanic Sciences, Univ. of Colorado, Boulder, CO, USA

(4) NOAA Chemical Sciences Division, Boulder, CO, USA

(5) Univ. of California, Davis, CA, USA

(6) College of Environmental Sciences and Engineering, Peking Univ., China

(7) Dept. of Earth and Atmospheric Sciences, Univ. of Houston, TX, USA

(8) School of Earth, Atmospheric, and Environmental Sciences, The Univ. of Manchester, Manchester, UK

(9) National Centre for Atmospheric Science, The Univ. of Manchester, Manchester, UK

(10) Aerodyne Research Inc., Billerica, MA, USA

(11) Georgia Institute of Technology, Atlanta, GA, USA

(12) Scripps Institution of Oceanography, Univ. of California San Diego, La Jolla, CA, USA

(13) Univ. of California, Berkeley, CA, USA

(14) Aerosol Dynamics Inc., Berkeley, CA, USA

(15) Dept. of Environmental Sciences and Engineering, Univ. of North Carolina, Chapel Hill, NC USA

(16) US Environmental Protection Agency, Research Triangle Park, NC, USA

(17) Center for Research in Environmental Science, School of Public and Environmental Affairs, and Department of Chemistry, Indiana Univ., Bloomington, IN, USA

(18) Univ Lille Nord de France, F-59000 Lille, France

(19) EMDouai, CE, F-59508 Douai, France

Correspondence to: J. L. Jimenez (jose.jimenez@colorado.edu)

41 **Supporting Material Sections:**

42 **Section A: CalNex Pasadena Ground Site Meteorology & Back-Trajectories**

43

44 **Section B: Instrument Comparisons & Selected Diagnostics**

45

46 **Section C: Comparisons to Previous Campaigns in Los Angeles Area and Additional**

47 **Aerosol Composition Figures**

48

49 **Section D: Selection of PMF Solution & Additional PMF Figures**

50

51 **Section E: Evaluation of Photochemical Age Error**

52

53 **Section F: NO_x Branching Ratios: Box-and-Whiskers Plot**

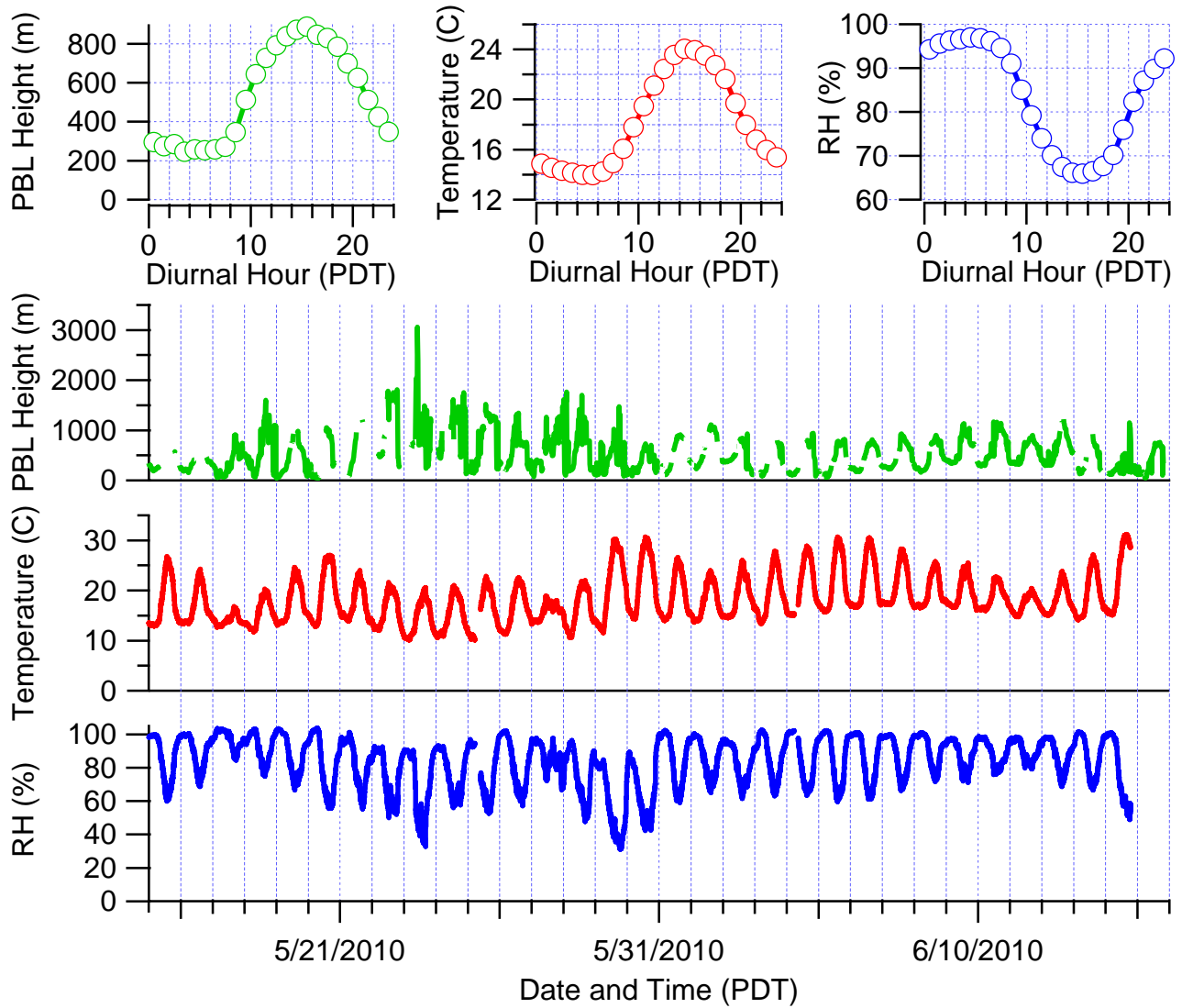
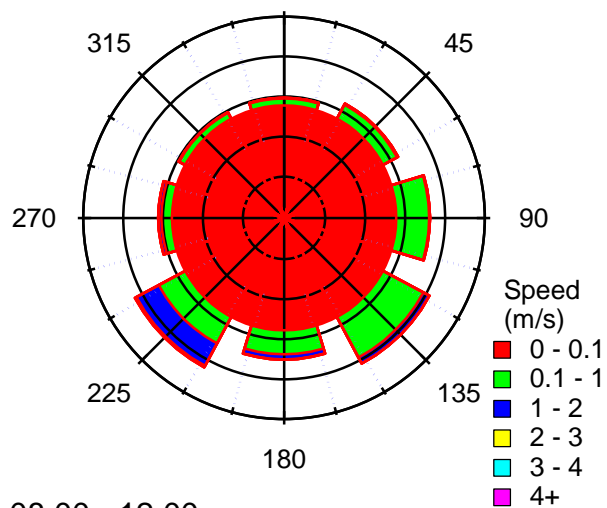
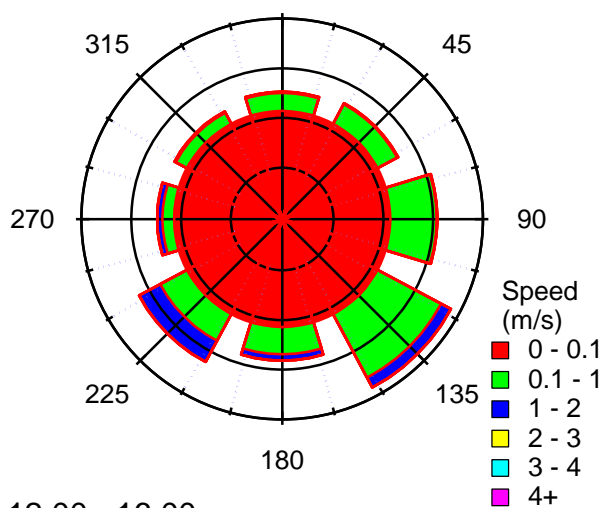


Figure A-1: Time series and diurnal profiles for planetary boundary layer height (PBL), temperature, and relative humidity at the Pasadena ground site during CalNex.

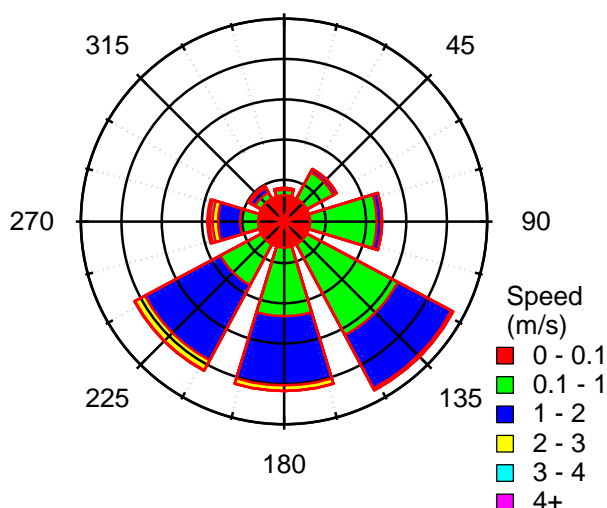
00:00 - 04:00



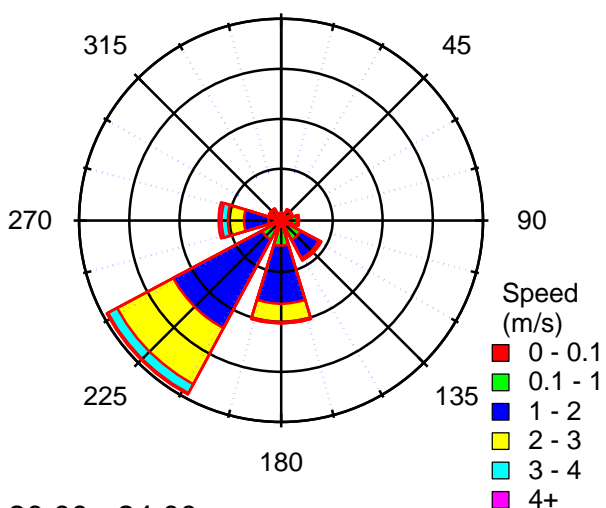
04:00 - 08:00



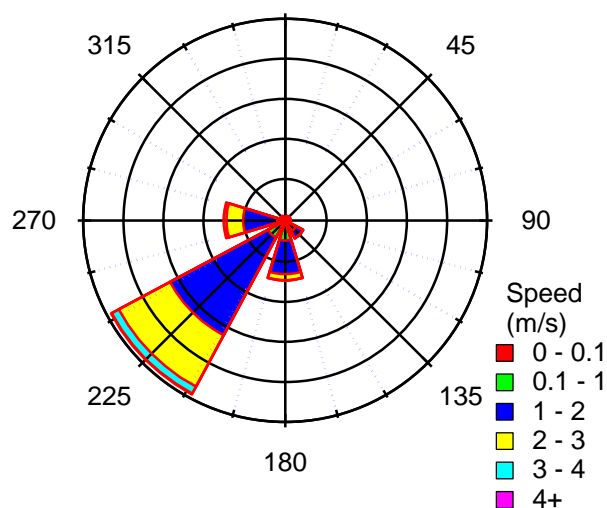
08:00 - 12:00



12:00 - 16:00



16:00 - 20:00



20:00 - 24:00

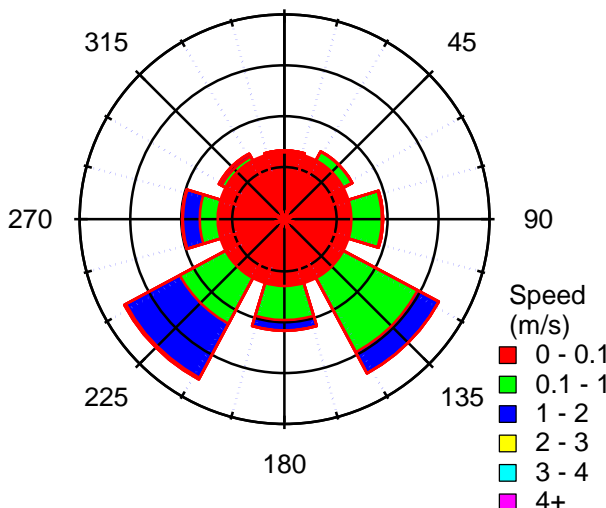


Figure A-2: Wind roses for the Pasadena ground site during CalNex organized by time of day (PDT). Zero on the polar coordinate is north and radial distance indicates relative frequency.

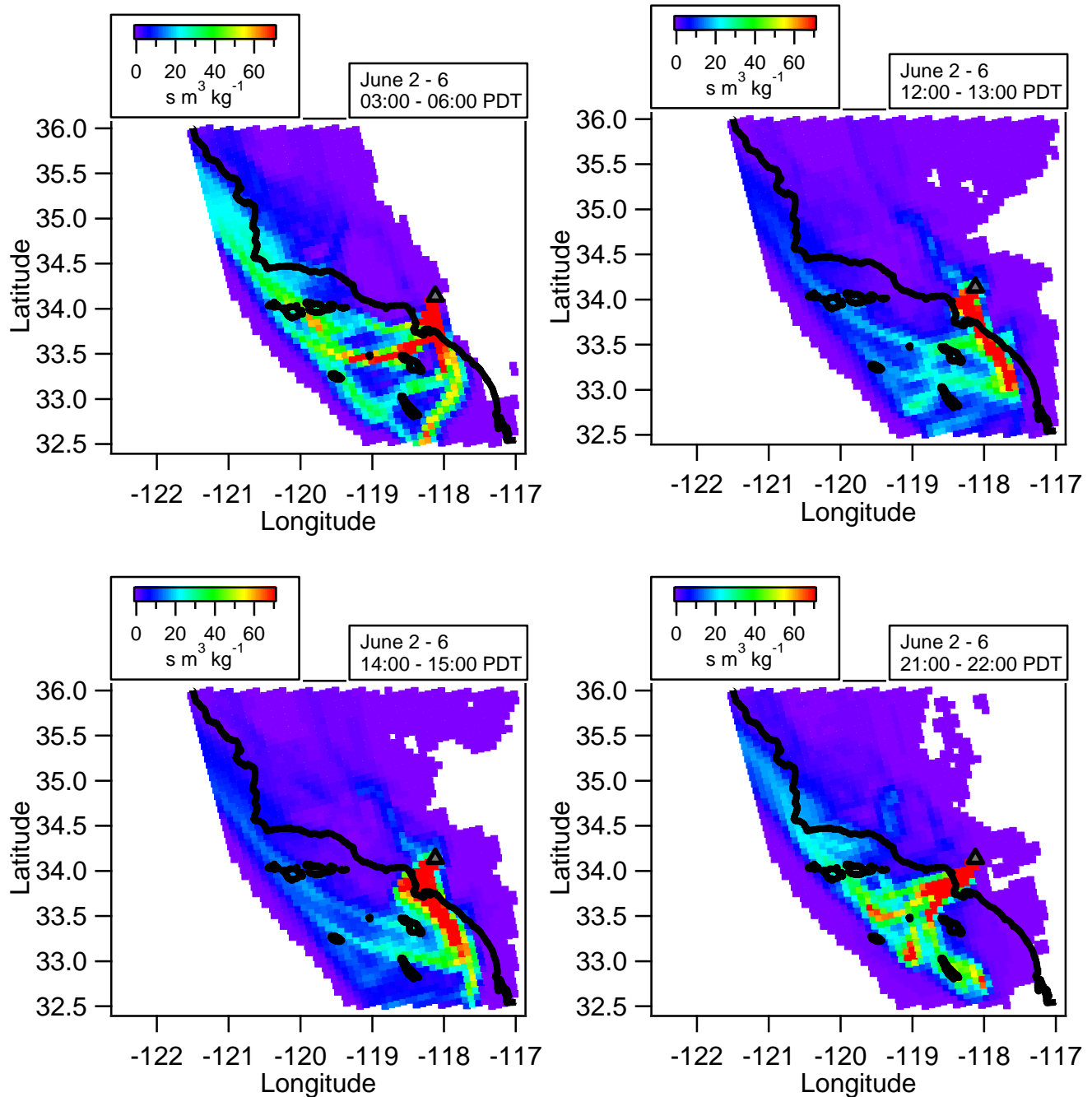


Figure A-3: Average 48 h FLEXPART back-trajectories for air masses arriving at the Pasadena ground site. Colors represent the footprint residence times. Each panel corresponds to a different time-of-day and is the average for June 2nd through June 6th. The grey triangle indicates the location of the Pasadena ground site.

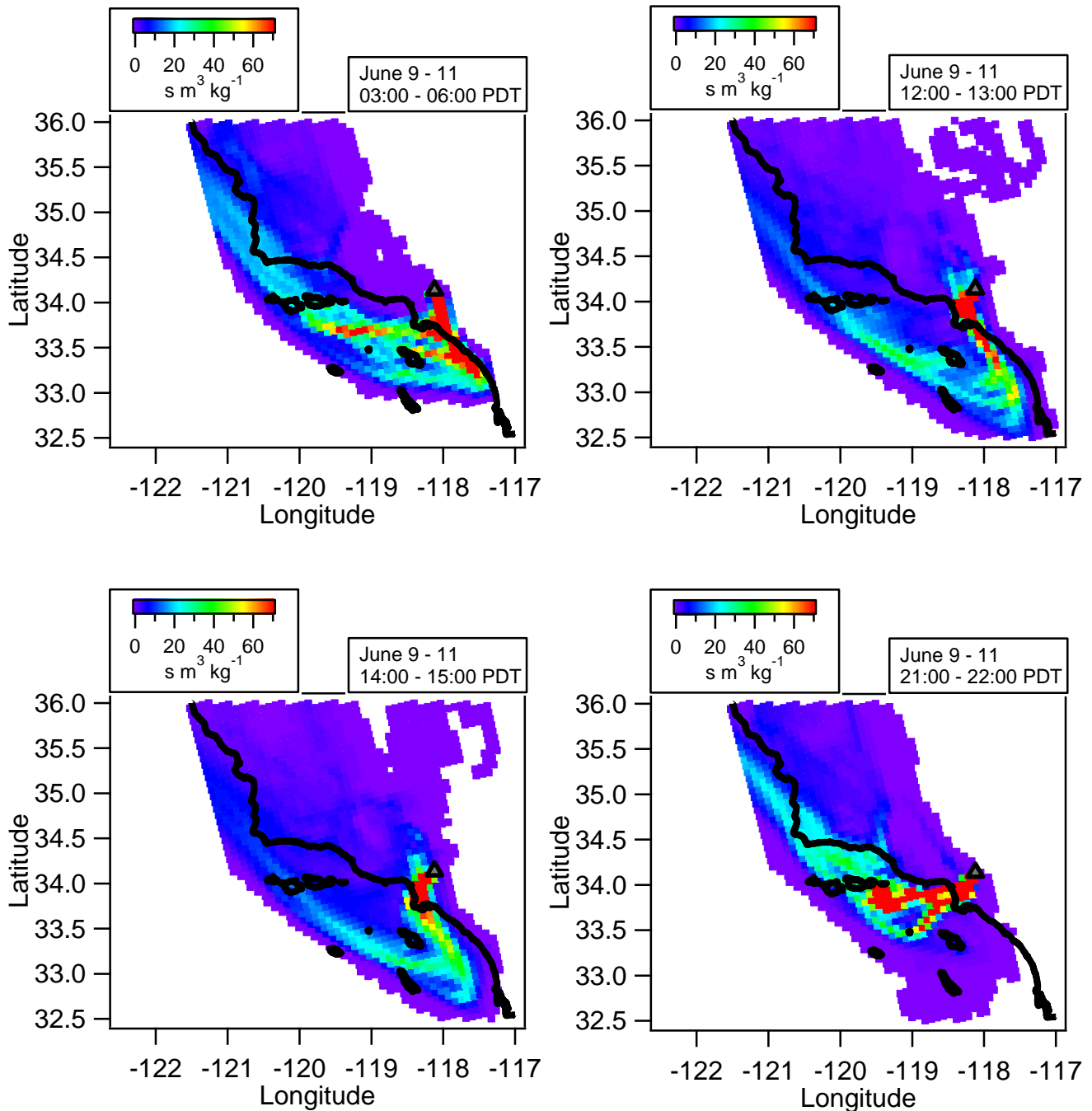


Figure A-4: Average 48 h FLEXPART back-trajectories for air masses arriving at the Pasadena ground site. Colors represent the footprint residence times. Each panel corresponds to a different time-of-day and is the average for June 9th through June 11th. The grey triangle indicates the location of the Pasadena ground site.

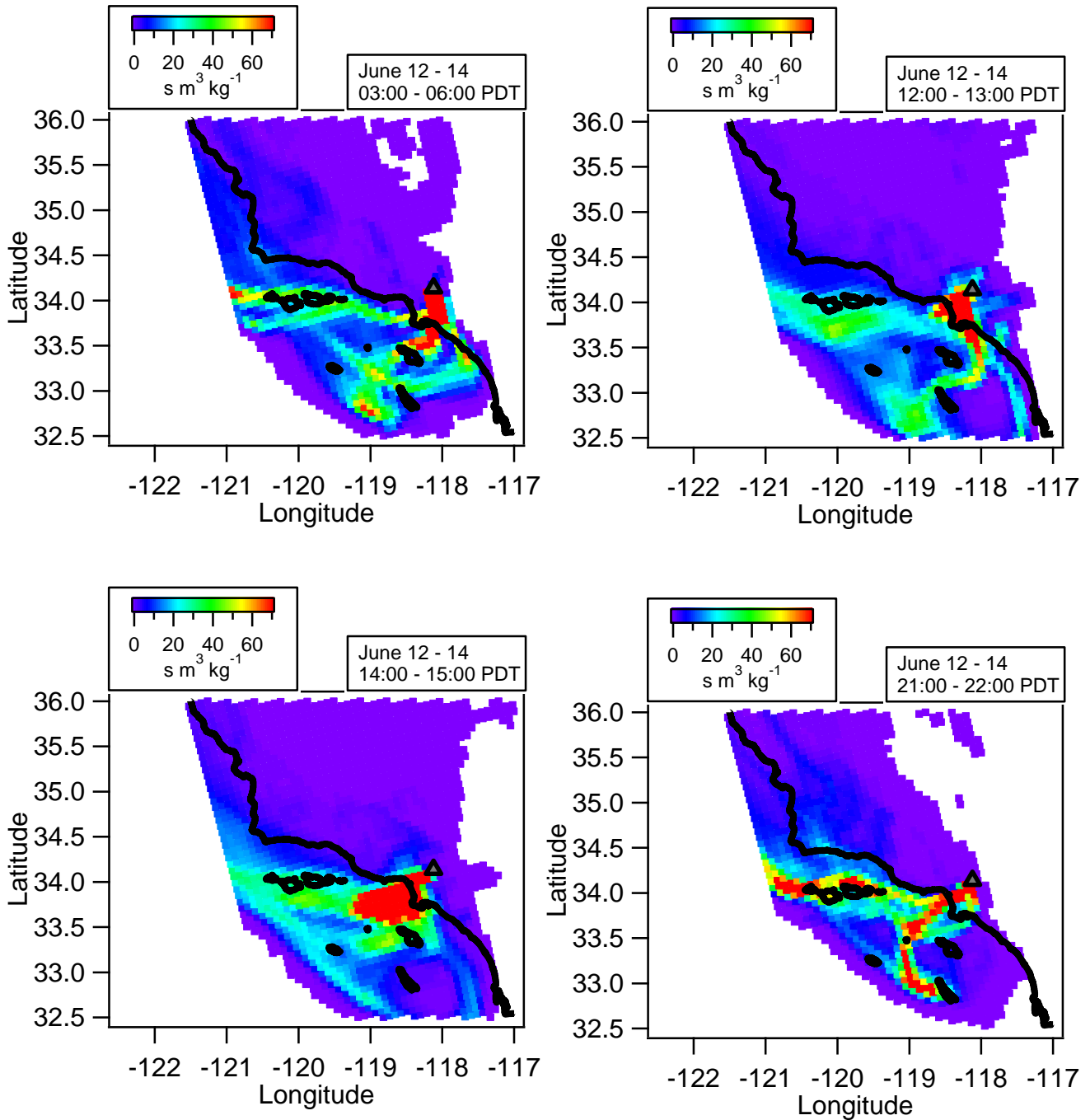


Figure A-5: Average 48 h FLEXPART back-trajectories for air masses arriving at the Pasadena ground site. Colors represent the footprint residence times. Each panel corresponds to a different time-of-day and is the average for June 12th through June 14th. The grey triangle indicates the location of the Pasadena ground site.

59 **Section B: Instrument Comparisons & Selected Diagnostics**

60 This section provides information that supports the validity of the AMS measurements. In
61 Figure B-1 the time series of submicron aerosol mass concentration measured by the AMS and
62 calculated from the SMPS and UHSAS number distributions are shown along with correlation
63 plots for the various instruments. (Note: the UHSAS number distribution was determined using a
64 refractive index of 1.515, which corresponds to dry ammonium sulfate at 1050 nm. A very brief
65 discussion of refractive index and optical properties is contained in the next paragraph.) The
66 AMS only measures non-refractory aerosol, and to partially compensate for this limitation the
67 rBC concentration from the SP2 is added to the AMS time series. The AMS also does not
68 measure mass from other refractory sources such as sea salt or mineral dust. These species are
69 not expected to significantly impact the instrument comparison though, because the relative
70 amount of the non-EC refractory mass is less than 5% of the total PM₁ aerosol mass (Figure 2B,
71 main text). Similarly, the PALMS instrument quantified the sum of mineral/road dust and sea
72 salt to be 9% of total submicron volume (Figure 3A, main text). The AMS and SMPS
73 instruments show good agreement, and a linear regression analysis of the two data results in a
74 slope of 1.03 ($R^2 = 0.85$) as shown in Panel C. The agreement between the AMS and UHSAS is
75 not as good (slope = 1.28, $R^2 = 0.84$) when the UHSAS data is truncated at 740 nm geometric
76 diameter to approximate the 1 μm aerodynamic diameter size cut of the AMS (Panel D). Given
77 the reasonable agreement between the AMS and SMPS as well as other instruments (see below),
78 it appears that the UHSAS, including the uncertainties in the conversion to volume and the
79 estimation of refractive index, may be responsible for this discrepancy. It is noted that from 6/4
80 through 6/6 there are extended periods when the AMS measurement is lower than both the
81 SMPS and UHSAS. This period exhibits an unusually large amount of mass above 740 nm

82 (estimated geometric diameter, equivalent to an estimated vacuum aerodynamic diameter of
83 1080 nm using the average density of 1.46 g cm^{-3} calculated from the AMS and SP2 aerosol
84 composition measurements.) as measured by the UHSAS (Panel B). Similarly, PALMS
85 measurements show a large volume concentration of sulfate/OA/nitrate particles above 784 nm
86 geometric diameter during this period (Figure 1 in main paper). The discrepancy from 6/4
87 through 6/6 is therefore attributed to a period of unusually large particles, which are near and
88 above the $1 \mu\text{m}$ aerodynamic diameter size cut for measurement by the AMS.

89 The SMPS measurements are also validated by calculating the Mie scattering from the
90 number size distribution data, and then comparing the result against extinction measurements
91 (Figure B-2). The extinction measurements are from the CAPS instrument and were taken at 532
92 and 630 nm. Good agreement between the calculated scattering and measured extinction is
93 observed when using an index of refraction 1.54, which is the average for dry ammonium sulfate
94 and ammonium nitrate [Kleinman *et al.*, 2007]. The refractive index of OA will vary depending
95 on composition, but an average value of 1.55 is often assumed when predicting optical properties
96 [Dick *et al.*, 2007; Kleinman *et al.*, 2007]. The particles were dried before measurements by the
97 SMPS and CAPS. It should be noted that the amount of black carbon at the site is relatively
98 small, and thus, scattering dominates the aerosol extinction [Thompson *et al.*, 2012], which
99 allows for the direct comparison of calculated scattering and measured extinction performed
100 here.

101 To further examine the AMS data, the concentrations of nitrate and sulfate aerosols
102 measured by the AMS and the PILS-IC instrument were compared (Figure B-3). An important
103 consideration when carrying out this comparison is that the PILS-IC was equipped with a $\text{PM}_{2.5}$
104 inlet, which transmits larger particles that cannot be measured AMS. For sulfate the agreement is

105 generally good, and a linear ODR regression analysis of the two data sets results in a best-fit
106 slope of 1.01 ($R^2 = 0.84$). The same analysis for nitrate results in a slope of only 0.64 ($R^2 =$
107 0.85), however. A possible explanation for the discrepancy between the nitrate measurements is
108 the presence of super-micron sodium nitrate that is formed when sea salt reacts with nitric acid as
109 discussed in the Appendix of the main text. To test this hypothesis, the regression analysis for
110 nitrate was repeated using only periods with PALMS sea salt volume concentrations of less than
111 $0.35 \mu\text{m}^3 \text{cm}^{-3}$, which corresponds to the 5th percentile of the data. A substantial improvement in
112 agreement is observed with the slope increasing to 0.89 (from 0.64). For the sake of
113 completeness the same test was performed on the sulfate data, but there is only a small increase
114 in the slope to 1.09 (from 1.01). Interestingly, the excellent agreement between the PILS-IC and
115 AMS sulfate, as well as the weak dependence on PALMS sea salt concentrations in the sulfate
116 scatter plot, suggests that little sodium sulfate has been formed from the reaction of sea salt and
117 sulfuric acid. Despite the technical differences between the AMS and PILS-IC, after accounting
118 for the presence of sodium nitrate in the supermicron mode there is reasonable agreement
119 between these two instruments with respect to sulfate and nitrate concentrations.

120 The comparisons of the AMS organic mass (OM) with multiple other measurements of
121 organic aerosols at the Pasadena ground site exhibits reasonable agreement. The different OM
122 and OC measurements are listed in Table B-1, and the results of the OM and OC comparisons
123 are summarized Table B-2 and Figure B-4. In Panel A of Figure B-4 the AMS OM_1 (the
124 subscript indicates the size cut in μm) and the online Sunset organic carbon mass ($\text{OC}_{2.5}$) are
125 plotted together and a strong correlation between the two measurements is observed. The AMS
126 OM_1 and online Sunset $\text{OC}_{2.5}$ data (Panel B) yield an R^2 value of 0.76, but the regression slope of
127 3.3 is significantly higher than the expected range of 1.4 – 2.3 [Aiken *et al.*, 2008; Turpin *et al.*,

128 2001]. Such a large discrepancy is outside the AMS uncertainty bounds of $\pm 30\%$ [Middlebrook
129 *et al.*, 2012]. While the exact reason for this discrepancy is unclear it may be related, at least
130 partially, to the presence of a denuder upstream of the Sunset carbon analyzer. Specifically, the
131 denuder may cause volatilization of particulate OC from the collection filter that is induced by
132 re-equilibration of organic concentrations after removal of vapor-phase organics by the denuder
133 [Grover *et al.*, 2008].

134 A scatter plot of the AMS OM₁ versus the OC_{2.5} measured from two sets of filter samples
135 collected by the Georgia Institute of Technology (GIT) and U.S. Environmental Protection
136 Agency (EPA) groups (Panel C) yields very reasonable slopes of 1.7 and 1.9 ($R^2 = 0.82$ and $R^2 =$
137 0.80 , respectively). These slopes are similar to the OM₁:OC₁ of 1.7 that was determined from the
138 elemental analysis of the AMS mass spectra. The OC_{2.5} concentration was also measured on a
139 third set of filter samples collected by the University of North Carolina (UNC) group. For the
140 UNC OC_{2.5} measurement the slope obtained from the regression analysis (Panel D) is 1.4, which
141 is lower than the other filter samples. This difference seems to be related to the collection times
142 for the filter samples. The UNC samples included several intensive sampling periods of 6 h or
143 less, whereas the GIT and EPA filters were switched daily. If only the daily UNC samples are
144 included in the regression analysis a slope of 1.8 is obtained, which is similar to the GIT and
145 EPA samples. The AMS OM₁ and the FTIR OM_{2.5} obtained from filter samples are compared in
146 Panel E resulting in a regression slope of 1.3 ($R^2 = 0.63$). Both the filters analyzed by FTIR as
147 well as the UNC filters exhibit higher amounts of organics relative to the 24 hr filters when the
148 collection times are shorter, which is likely due to evaporation losses of semi-volatiles from the
149 daily samples [Russell *et al.*, 2009b]. Furthermore, high temperatures on the asphalt-coated roof
150 where the filter samplers were located may have increased the influence of evaporation. It should

151 be noted that all the analyses are for PM_{2.5} particles except the AMS, which is a PM₁ instrument.
152 The impact of the different size cuts on the comparison can be evaluated by estimating that 15%
153 of the PM_{2.5} organic mass is present between 1 and 2.5 μm on average. This percent is
154 determined from online Sunset OC measurements that were performed while switching between
155 a PM_{2.5} and PM₁ cyclone from 6/12 through 6/16. Accounting for this additional mass that is not
156 measured by the AMS would increase the slopes for the regression analyses, but the corrected
157 values for the GIT, EPA, and UNC filter samples would still fall within the expected range of 1.2
158 – 2.2 for OM/OC (the expected 1.7 value with a ±30% uncertainty range for the AMS, and
159 neglecting the uncertainty of the OC measurements).

160 For completeness, the slopes from linear ODR regression analyses for each possible
161 pairing of OM or OC measurements are summarized in Table B-2 along with R² values. The
162 AMS measurements of OM₁ are converted to OC₁ using the OM₁:OC₁ ratios determined from
163 the elemental analysis of the AMS mass spectra. In general, the AMS and all three of the filter
164 OC_{2.5} measurements (GIT, EPA, UNC) are in agreement within the uncertainties, exhibiting
165 slopes between 0.81 and 1.14 and R² values higher than 0.60. The lowest correlations are for
166 comparisons with the UNC filter samples, which is likely due to different slopes observed in the
167 regression analyses for the 24 h versus intensive UNC sampling periods. If comparing only 24 h
168 OC_{2.5} data from the UNC group against the AMS as well as the EPA and GIT filter samples, then
169 all the R² values are higher than 0.78. The online Sunset OC_{2.5} measurement shows good
170 correlation with the AMS and the filter OC measurements (R² ≥ 0.75), but it is systematically
171 lower by about a factor of two against all other measurements, which might be due to the
172 denuder utilized in the online Sunset OC_{2.5} measurement as described in the preceding
173 paragraph. Alternatively, the un-denuded OC_{2.5} filter samples may be impacted by a positive

174 artifact due to adsorbing volatile organic gases, although the agreement between the online AMS
175 OC_1 and offline filter $OC_{2.5}$ indicates that this positive artifact is not impacting other
176 comparisons. Lastly, when comparing the 24 h FTIR $OM_{2.5}$ against the 24 h GIT and EPA filter
177 $OC_{2.5}$ the slope is considerably lower than the expected OM:OC ratio, and the correlation
178 between the measurements is only moderate ($R^2 \geq 0.52$). One possible reason for the low FTIR
179 $OM_{2.5}$ concentrations and the lack of a strong correlation is that the evaporation of organics from
180 the FTIR samples was more extensive. The UNC filter $OC_{2.5}$ shows better agreement with the
181 FTIR $OM_{2.5}$ results (FTIR $OM_{2.5} : UNC OC_{2.5} = 1.29$, $R^2 \geq 0.76$), which is expected since these
182 samplers were located closer to each other on the Keck Building rooftop, and both analyses
183 included intensive samples. Selecting only the intensive periods slightly improves the best-fit
184 slope in the regression analysis (1.33 vs. 1.29). As discussed above the AMS OM_1 and FTIR
185 $OM_{2.5}$ agree reasonably well although the FTIR $OM_{2.5}$ is somewhat lower (AMS $OM_1 : FTIR$
186 $OM_{2.5} = 1.25$, $R^2 \geq 0.63$). This observation is consistent with previous comparisons that have
187 shown FTIR measurements tend to be lower than and less correlated with AMS measurements
188 when carried out in urban areas [Russell *et al.*, 2009a].

189 **Table B-1:** Summary of the different OM and OC measurements taken on the Caltech campus
 190 during the CalNex campaign (GIT = Georgia Institute of Technology, EPA = U.S.
 191 Environmental Protection Agency, UNC = University of North Carolina). Note: the intensive
 192 periods for the UNC Filter OC and FTIR OM coincided.

	Online/Offline?	Location	Dates for Sampling	Number of Samples	Time Resolution	Size Cut
AMS	Online	Ground Site	5/15-6/15	3681	2.5 min	PM ₁
Sunset Online OC	Online	Ground Site	5/15-6/15	775	44 min	PM _{2.5}
GIT Filter OC	Offline	Keck Roof	5/15-6/15	31	23 h	PM _{2.5}
EPA Filter OC	Offline	Keck Roof	5/15-6/15	32	23 h	PM _{2.5}
UNC Filter OC	Offline	Keck Roof	5/15-6/13	58	23 h, or 3-6 h	PM _{2.5}
FTIR OM (Scripps)	Offline	Keck Roof	5/15-6/15	57	23 h, or 3-6 h	PM _{2.5}

193

194 **Table B-2:** Slopes and correlation coefficients for regression analyses of various OM and OC
 195 measurements located on the CalTech campus during CalNex (GIT = Georgia Institute of
 196 Technology, EPA = U.S. Environmental Protection Agency, UNC = University of North
 197 Carolina). *Note:* FTIR results correspond to FTIR OM data, while all other data sets are
 198 exclusively OC.

Slope	AMS OC ₁	FTIR OM _{2.5} (Scripps)	Online Sunset OC _{2.5}	GIT Filter OC _{2.5}	EPA Filter OC _{2.5}	UNC Filter OC _{2.5}	(y data)
AMS OC ₁							
FTIR OM _{2.5} (Scripps)	1.25 ^a						
Sunset Online OC _{2.5}	1.95	3.13					
GIT Filter OC _{2.5}	0.99	0.83	0.48				
EPA Filter OC _{2.5}	1.13	0.99	0.56	1.14			
UNC Filter OC _{2.5}	0.81	1.29	0.41	1.12	0.88		
(x data)							
R ²	AMS OC ₁	FTIR OM _{2.5} (Scripps)	Online Sunset OC _{2.5}	GIT Filter OC _{2.5}	EPA Filter OC _{2.5}	UNC Filter OC _{2.5}	
AMS OC ₁							
FTIR OM _{2.5} (Scripps)	0.63 ^a						
Sunset Online OC _{2.5}	0.75	0.49					
GIT Filter OC _{2.5}	0.78	0.52	0.86				
EPA Filter OC _{2.5}	0.78	0.55	0.82	0.93			
UNC Filter OC _{2.5}	0.76	0.76	0.75	0.75	0.60		

199
 200 ^aThe AMS vs. FTIR comparison is for OM vs. OM.

201

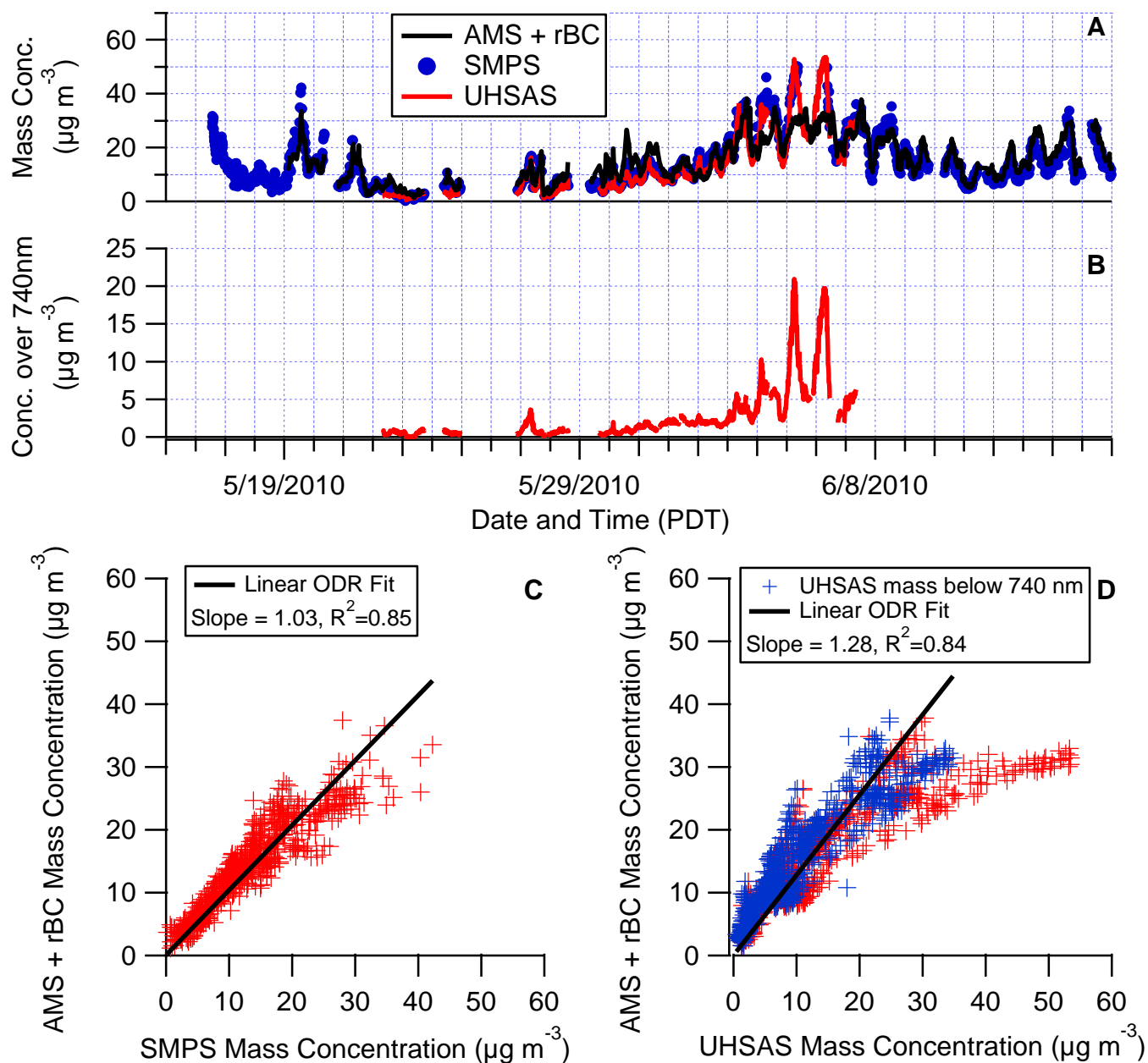


Figure B-1: (A) Time series of mass concentrations as measured by the AMS, SMPS, and UHSAS. rBC from the SP2 has been added to the AMS time series. The SMPS and UHSAS mass concentrations are calculated assuming spherical particles and using an estimated density obtained from the AMS and rBC measurements [Zhang *et al.*, 2005]. (B) The mass over 740 nm estimated geometric diameter, equivalent to ~ 1080 vacuum aerodynamic diameter, as measured by the UHSAS. (C) Scatter plot of the AMS plus rBC versus SMPS mass concentrations with linear fit. (D) Scatter plot of the AMS plus rBC versus UHSAS mass concentrations. The total UHSAS mass (red markers) and the UHSAS mass for particles less than 740 nm in geometric diameter (blue markers) are displayed. The linear fit corresponds to the UHSAS mass below 740 nm geometric diameter.

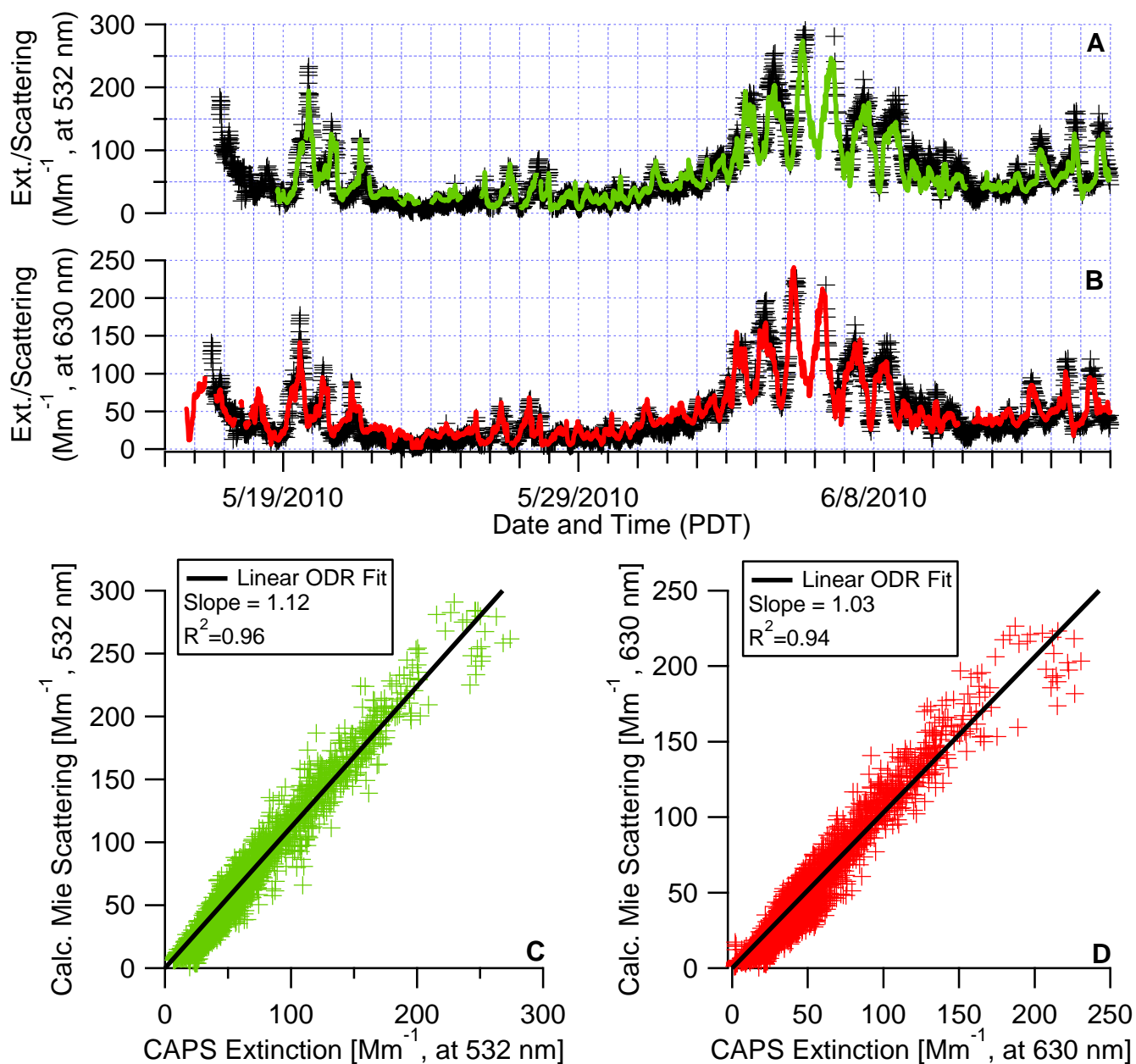


Figure B-2: (A) Time series of extinction measured by the CAPS instrument (green line) and Mie scattering calculated from SMPS data (black markers). Both traces correspond to a wavelength of 532 nm, and the Mie scattering was calculated using a refractive index of 1.54, which is the average for $(\text{NH}_4)_2\text{SO}_4$ and NH_4NO_3 [Kleinman *et al.*, 2007]. (B) Time series of CAPS extinction (red line) and calculated Mie scattering (black markers). Both traces correspond to a wavelength of 630 nm, and the Mie scattering was calculated using the same index of refraction (1.54). (C) Scatter plot of calculated Mie scattering and CAPS extinction for 532 nm with a linear fit of the data. (D) Scatter plot of calculated Mie scattering and CAPS extinction for 630nm with a linear fit of the data.

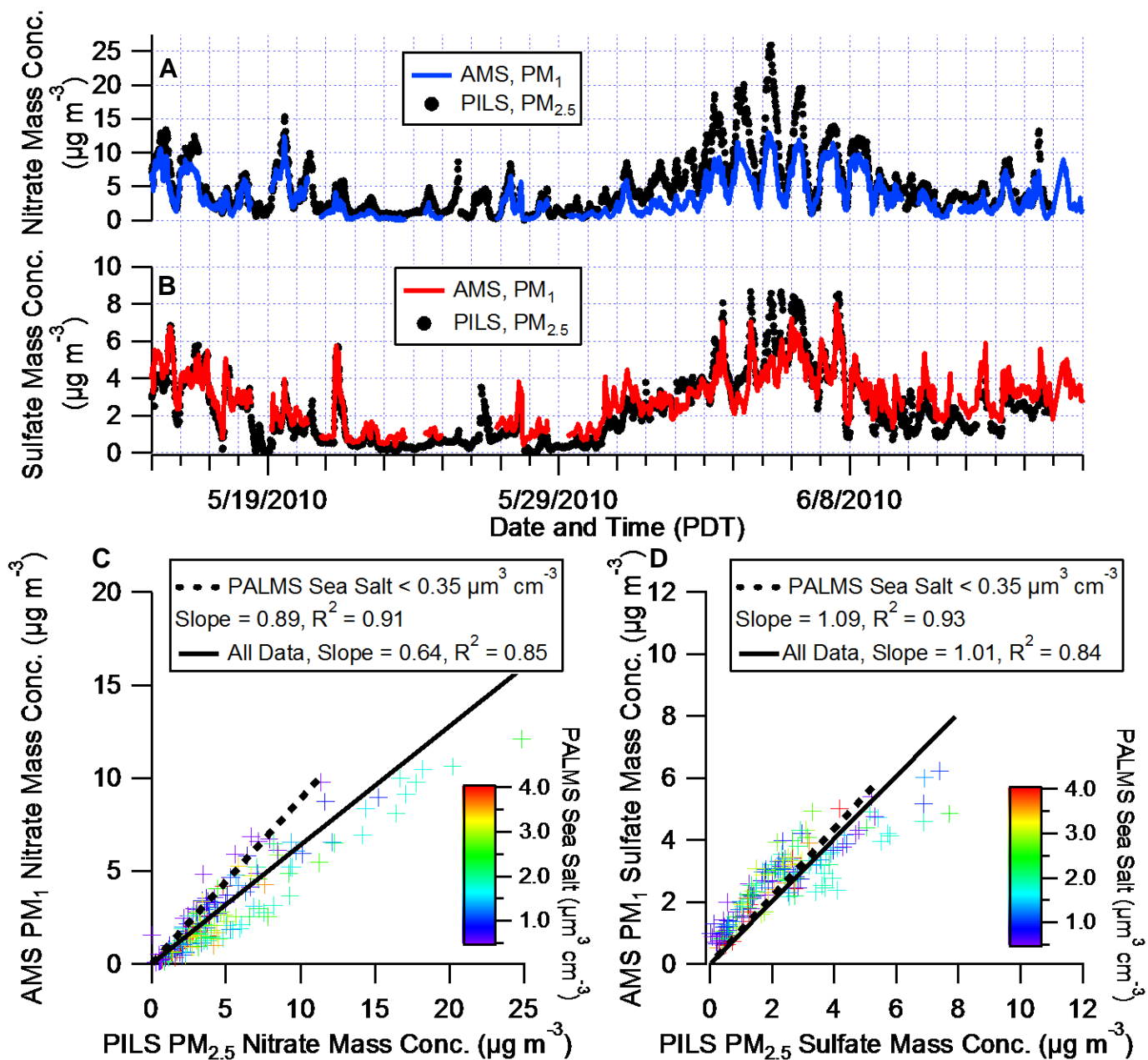


Figure B-3: (A) Time series of nitrate mass concentration measured by the AMS and the PILS-IC instrument. (B) Time series of sulfate mass concentration measured by the AMS and the PILS-IC instrument. (C) Scatter plot of the AMS and PILS-IC nitrate mass concentrations. Linear fits are shown for the entire data set (solid line), and also for selected periods with low PALMS sea salt concentrations (dashed line). (D) Scatter plot of the AMS and PILS-IC sulfate mass concentrations. Linear fits are shown for the entire data set (black solid line), and also for periods with low PALMS sea salt concentrations dashed line). The PALMS data corresponds to a PM_{2.5} size cut.

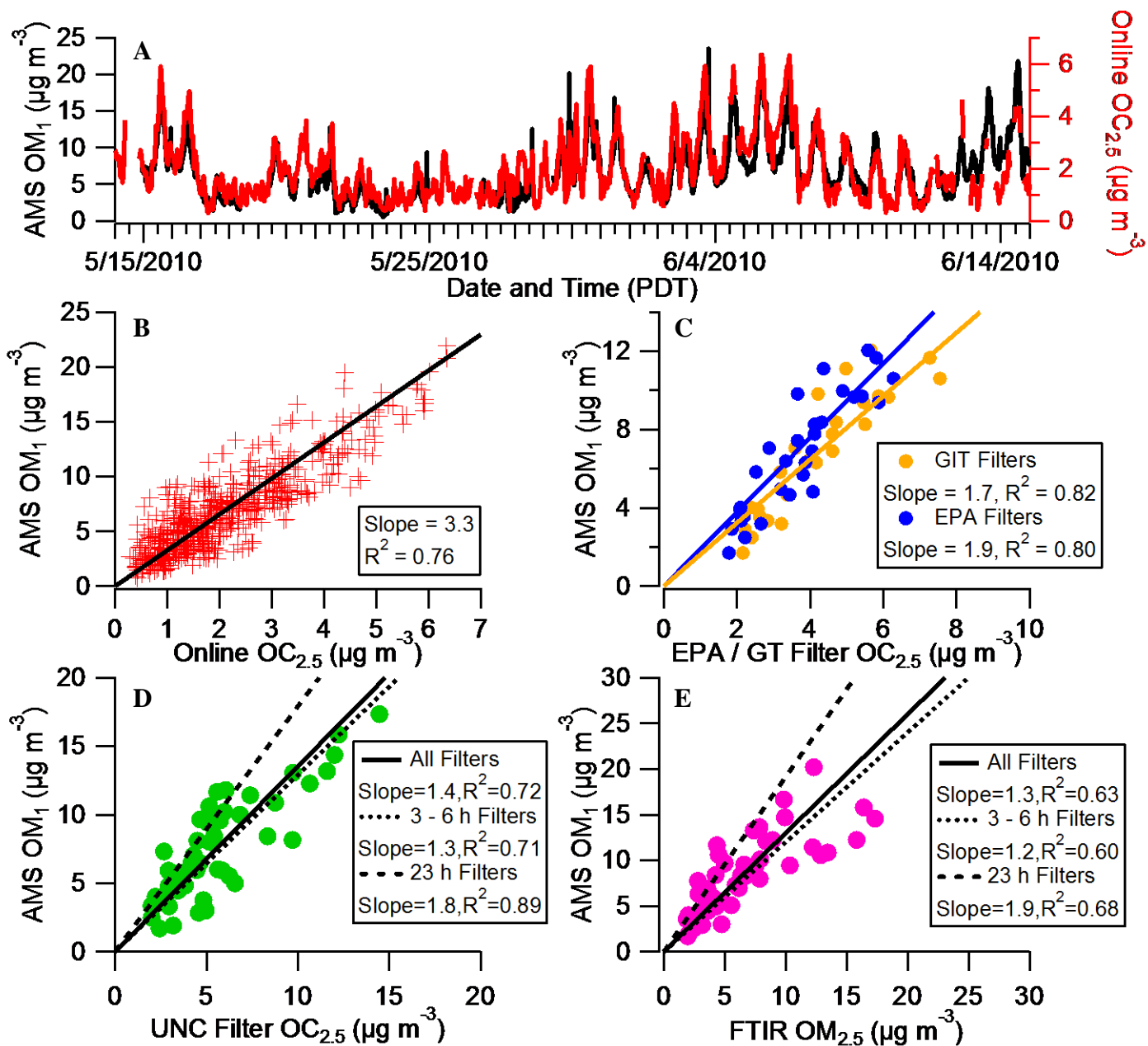


Figure B-4: (A) Times series of the OM_1 measured by the AMS and the $OC_{2.5}$ measured online by the Sunset Labs OC/EC analyzer. (B) Scatter plot of the AMS OM_1 versus the online Sunset $OC_{2.5}$. (C) Plot of the AMS OM_1 versus the $OC_{2.5}$ measured using two sets of filter samples collected by the Georgia Institute of Technology group (gold) and the EPA group (blue). (D) Plot of the AMS OM_1 versus the $OC_{2.5}$ measured from the UNC group filter samples. (E) Plot of the AMS OM_1 versus the $OM_{2.5}$ determined from FTIR measurements. The lines in Panels B – E represent linear fits of the data. Subscripts indicate measurement size cut in μm and for aerodynamic diameter.

206 **Section C: Comparisons to Previous Campaigns in Los Angeles Area and Additional**
207 **Aerosol Composition Figures**

208 In Table C-1 the campaign average mass concentrations reported for CalNex are
209 compared against those from three previous campaigns that took place in the LA basin: SOAR-1
210 [Docherty *et al.*, 2011], PACO [Hersey *et al.*, 2011], and SCAQS [Chow *et al.*, 1994]. It should
211 be noted that the PACO campaign consisted of three periods, and for the purpose of this
212 comparison the first and third periods were selected, since those portions of PACO took place at
213 the same time of year as CalNex and SOAR-1, respectively. The fractional composition is
214 similar between the sites despite the different locations and years for the campaigns, as well as
215 the utilization of different measurement techniques during the SCAQS campaign. The dominant
216 fraction is OA, which accounts for about half of the total mass. Sulfate and nitrate are the next
217 largest fractions ranging between 16 – 30% and 14 – 22% of the total mass, respectively. The
218 relative amount of ammonium is surprisingly consistent between the campaigns accounting for
219 12 – 13% of the total mass, while the chloride is a small percentage for all the studies. In
220 Pasadena, Riverside, and Burbank EC accounted for 3 – 6% of the aerosol mass concentration,
221 respectively.

222 The fraction of organic signal at m/z 44, termed f_{44} , is often taken as an indicator of
223 relative oxygen content in OA because in ambient measurements m/z 44 is typically dominated
224 by the CO_2^+ ion. The scatter plot of O/C and f_{44} shown in Figure C-1 confirms and quantifies this
225 relationship for Pasadena during CalNex. (Note: CO_2^+ was not separated using the high-
226 resolution data for this figure, but on average CO_2^+ accounted for 95% of the organic signal
227 measured at m/z 44.) In addition, Figure C-1 includes the best-fit lines determined from
228 regression analyses of the CalNex data as well as for Riverside and Mexico City. All three lines

229 are similar, which supports the validity of the AMS measurements for Pasadena and provides a
230 sample of the variability of the O/C to f_{44} relationship across different field sites and time
231 periods.

232 Shown in Figure C-2 is the relative contribution of each species to the submicron mass as
233 a function of the total mass. A probability density distribution of the submicron mass is displayed
234 as well (right axis). All data represent three hour averages. The relative composition does not
235 vary greatly between low and high concentration periods. Nitrate becomes more important with
236 increasing total concentrations (up to 29%). OA is important at all concentrations and is typically
237 40% of PM_{10} . The data in Figure C-2 illustrate that OA and ammonium nitrate contribute
238 substantially to the number of high PM_{10} events. Shown in Figure C-3 is the relative contribution
239 of each PMF component to the OA mass as a function of the total OA mass (similar to Figure C-
240 2). A probability density of the OA mass is displayed as well (right axis). The relative OA
241 composition is increasingly dominated by OOA, and in particular SV-OOA, during high
242 concentration periods. As discussed previously, OA is an important contributor to the total
243 submicron mass at all concentrations. Combining the data shown in Figures C-2 and C-3, it can
244 then be concluded that freshly formed SOA, likely from photochemical production within the
245 basin, contributes substantially to the number of high PM_{10} events along with nitrate. As
246 discussed in Section 3.1 many of the highest PM_{10} concentrations occur during periods when
247 synoptic conditions (e.g., low boundary layer heights) trap pollution in the LA Basin.

248

249

250 **Table C-1:** Summary of campaign average mass concentrations as a percent of the total nrPM₁
 251 and EC during CalNex, SOAR-1, PACO, and SCAQS. (Note: Campaign average EC
 252 concentrations were not reported for PACO. Given the low concentrations of EC observed for
 253 selected days during PACO however, the impact on the calculated percentages is likely to be
 254 small.)

	CalNex ^a	SOAR-1 ^b	PACO (I) ^c	PACO (III) ^d	SCAQS ^{e,f,g}
Location	Pasadena	Riverside	Pasadena	Pasadena	Burbank
OA	43	45	42	55	43
Nitrate	22	22	15	15	14
Sulfate	18	17	30	16	24
Ammonium	13	12	13	13	12
Chloride	<1	<1	<1	<1	<1
EC	3	4	N/A	N/A	6

255

^a May 15th to Jun 16th, 2010 (AMS and Sunset EC measurements)
^b Jul 15th to Aug 15th, 2005 (AMS and Sunset EC measurement)
^c May 22nd to Jun 12th, 2009 (AMS measurements)
^d Jul 10th to Aug 4th, 2009 (AMS measurements)
^e Jun 9th to Sept 3rd, 1987 (Selected Days)
^f PM_{2.5}, OC measurement converted to OM using OM:OC of 1.7, water-soluble inorganics only
^g Chloride, nitrate, and sulfate measured by ion chromatography, ammonium measured by colorimetry, OC measured by thermal manganese oxidation.

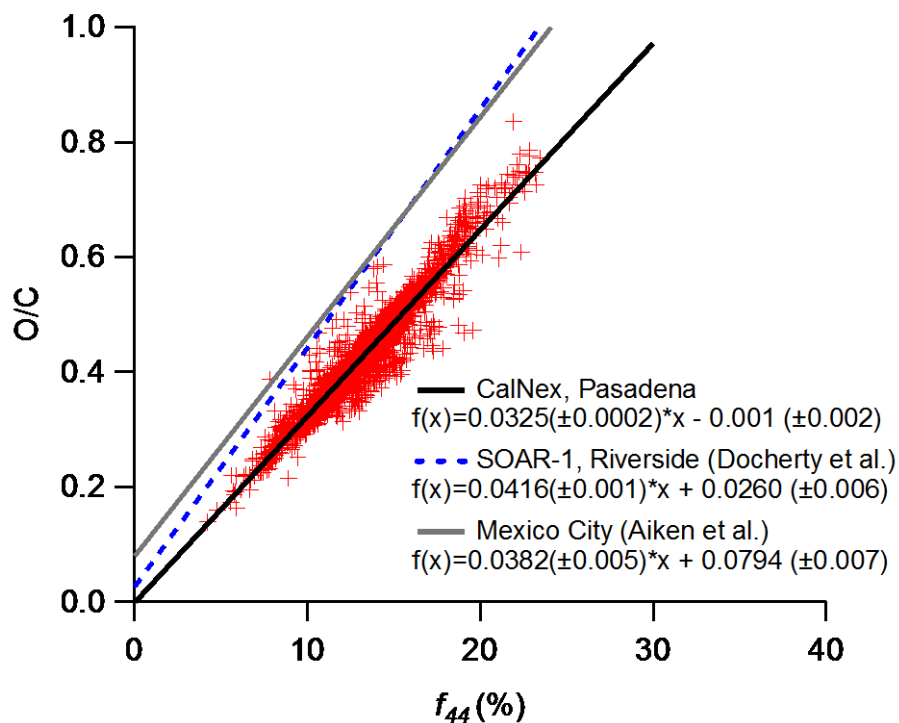


Figure C-1: Scatter plot of f_{44} versus O/C calculated from HR-ToF-AMS high resolution data. A linear ODR fit of the CalNex data is shown along with the similar results from Riverside, CA [Docherty *et al.*, 2011] and Mexico City [Aiken *et al.*, 2008].

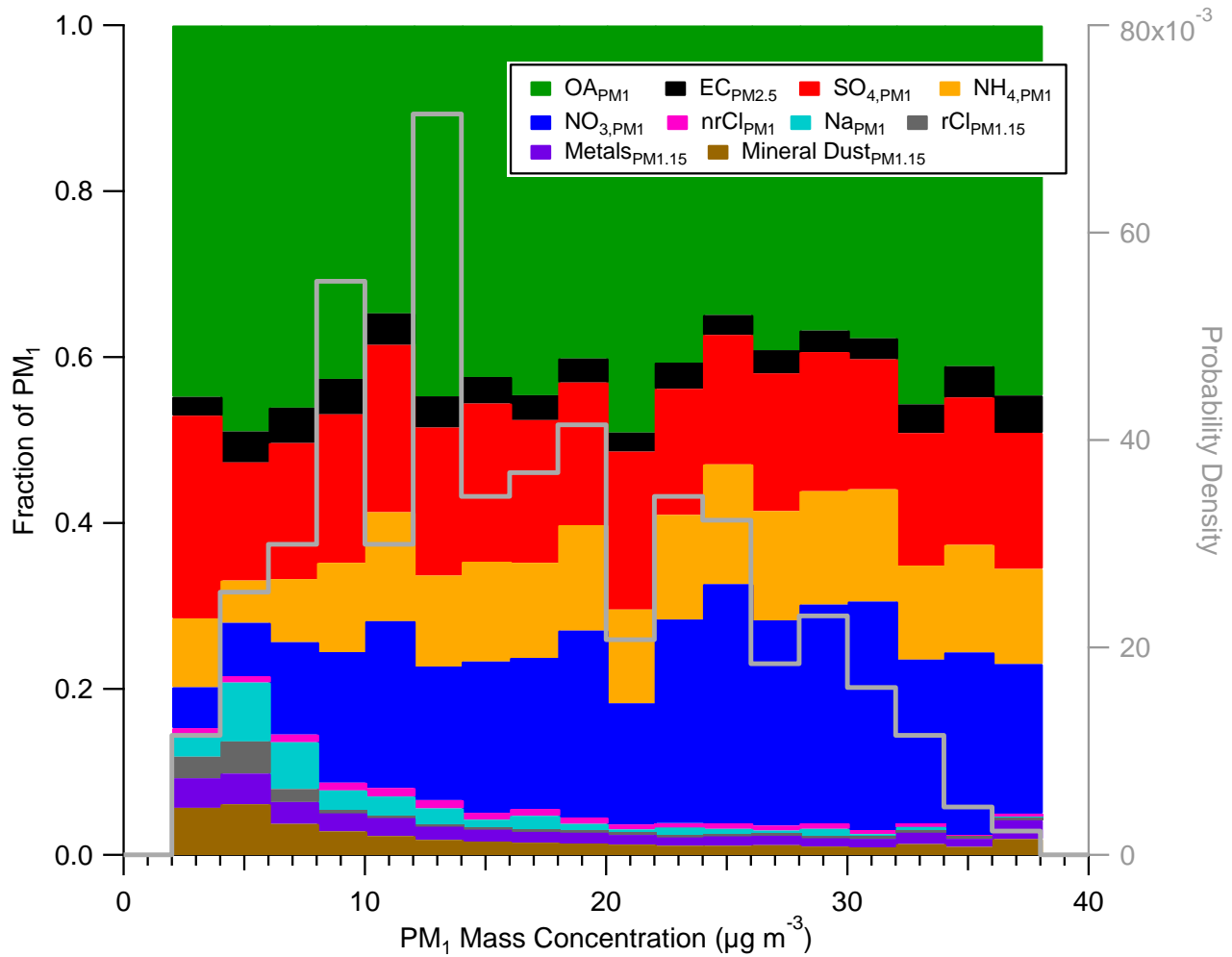


Figure C-2: The fraction of the total submicron aerosol mass contributed by different aerosol species as a function of the total mass. Also shown is a histogram of the total submicron aerosol mass for CalNex (right axis).

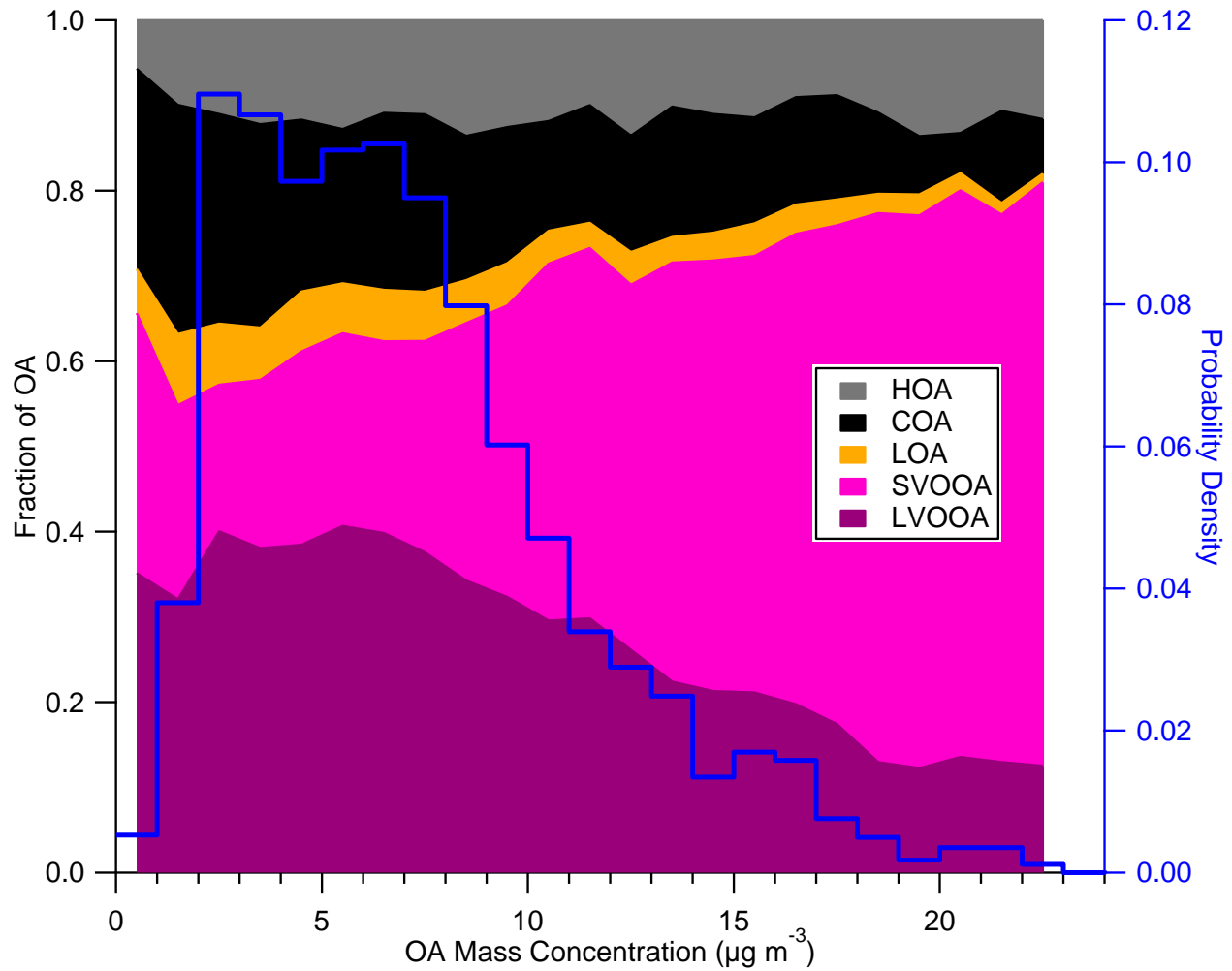


Figure C-3: The fraction of the OA mass contributed by different components as a function of the total OA mass. Also shown is a histogram of the total OA mass for CalNex (blue, right axis).

259 **Section D: Selection of PMF solution & Additional PMF Figures**

260 This section describes the process for selecting the 5-component PMF solution that is
261 described in the main text. An in-depth description of PMF and its application to AMS data is
262 not included here as it has already been provided in previous publications [*Paatero et al.*, 1994;
263 *Ulbrich et al.*, 2009], and instead we focus on the specific analysis of the CalNex data set. The
264 selection of the solution was based on the mass spectral profiles, the time series, diurnal cycles,
265 and the correlations of the components with time series for tracer species. Panel A of Figure D-1
266 summarizes the types and mass fractions of the different components identified as the number of
267 components is systematically increased from 3 to 10 (for FPeak=0). The 3-component solution is
268 similar to that found for PMF analyses of other data sets with HOA, SV-OOA, and LV-OOA
269 components identified. If the number of components is increased to four, then CIOA is also
270 resolved. The mass fraction of HOA is substantially reduced in the 4-component solution
271 compared to the 3-component solution. Furthermore, HOA in the 3-component solution exhibits
272 a unique evening peak, and in the 4-component solution CIOA displays this peak instead of
273 HOA. Together these observations suggest that a large portion of the CIOA mass is classified as
274 HOA in the 3-component solution. We conclude that the CIOA component is distinct from the
275 other components, and in particular HOA, based on its substantially different diurnal cycle
276 (Figure 5A, main text), and the dramatic improvement in the correlation of HOA with rBC (R
277 increases from 0.55 to 0.72) when increasing the number of components to four. This conclusion
278 is further supported by the mass spectra as discussed in this section below.

279 Increasing the number of components to five leads to a third OOA component, but it is
280 unclear if the additional component represents a different type of OOA given the lack of unique
281 correlations with tracers. In contrast, at six components LOA is resolved, which is clearly

282 distinct from the previously identified components. The LOA component is nitrogen-rich, and
283 has a substantially different time series (Figure 4, main text). As described in the main text the
284 LOA mass spectra is distinguished by prominent fragments that are characteristic of amines:
285 CH_4N^+ (m/z 30), $\text{C}_2\text{H}_4\text{N}^+$ (m/z 42), $\text{C}_3\text{H}_6\text{N}^+$ (m/z 56), $\text{C}_3\text{H}_8\text{N}^+$ (m/z 58), $\text{C}_5\text{H}_{10}\text{N}^+$ (m/z 84),
286 $\text{C}_5\text{H}_{12}\text{N}^+$ (m/z 86). The sum of the absolute residuals associated with these amines is plotted
287 versus number of components in Panel B of Figure D-1. This residual decreases with the number
288 of components, but the decrease is largest between the five-component and six-component
289 solutions. In addition, there is only a slight decrease in the residuals when increasing the number
290 of components beyond six. Clearly, LOA in the 6-component solution is needed for PMF to
291 properly account for amines in OA measured at the Pasadena ground site.

292 For PMF solutions with more than 6 components interpretation becomes increasingly
293 difficult. Numerous oxygen-rich components are identified, which could be classified as OOA.
294 Unique correlations to identify separate sources for these components are not found though. A
295 key limitation of PMF analysis is the assumption of a constant mass spectrum for each
296 component. Thus, it is possible that the variable nature of the SOA spectrum with, for instance,
297 photochemical age leads to significant residuals in PMF, and when increasing the number of
298 components beyond six these residuals control the additional components in the PMF solution,
299 leading to more ‘OOA’ components [Ulbrich *et al.*, 2009].

300 Even in the 6-component solution it is unclear if the three OOA components represent
301 distinct sources or chemical types. Specifically, for the 6-factor solution two of the three OOA
302 components (OOA-2 and OOA-3) exhibit a high correlation in time ($R=0.77$) and very similar
303 correlations with tracers (Figure D-2), which suggests these two components may not be distinct.
304 Furthermore, OOA-3 is the most oxidized component, but does not show the strongest

305 correlation with sulfate, which is usually associated with more aged OOA [DeCarlo *et al.*, 2010;
306 Sun *et al.*, 2011; Ulbrich *et al.*, 2009]. It is proposed therefore, that the OOA-3 factor results
307 from artificial “splitting” and/or “mixing” of distinct components that is observed when too
308 many components are requested in a PMF solution [Ulbrich *et al.*, 2009]. This artifact is likely
309 due to the fixed nature of the OOA spectra that do not fully capture the chemical variability of
310 SOA, which is a potentially larger source of residuals than omission of the LOA component. To
311 address this problem while at the same time resolving the LOA component, the PMF analysis is
312 repeated after subtracting out the contribution of LOA to the mass spectral matrix. The LOA
313 contribution is determined from the 6-component solution of the original PMF analysis, and is
314 included when summarizing the final PMF results. Thus, this method is equivalent to
315 constraining LOA to have a time series and mass spectrum that is invariant as the number of
316 component is increased similar to advanced factor analysis of Lanz *et al.* [2008]. It is also noted
317 that while selection of a PMF solution does require subjective ‘user input’, the exploration of
318 higher factor solutions and the recombination of factors that are indistinct has been previously
319 reported in the literature [e.g., Docherty *et al.*, 2011; Liu *et al.*, 2011; Zhang *et al.*, 2007].

320 It should be noted that the LOA contribution to the total OA mass is small. Also, LOA
321 exhibits a time series and mass spectra that contributes significantly to the PMF residual and is
322 quite different from the other components. Thus, it is expected that subtracting the LOA
323 contribution only has a weak influence on the other PMF components. To verify this weak
324 influence, a correlation analysis was carried out that compared each component for the four
325 component solution without LOA subtracted against the five component solution in which the
326 LOA was subtracted. In other words, the 4-component solution (HOA, CIOA, SVOOA, and
327 LVOOA) in the original PMF analysis is compared against the 5-component solution in the PMF

328 analysis with a fixed LOA contribution (HOA, CIOA, SVOOA, LVOOA, and LOA). As can be
329 seen in Figure D-3 the time series and mass spectra of HOA, CIOA, SVOOA, and LVOOA for
330 the two PMF methods are almost identical. The correlation plot for the HOA time series exhibits
331 a slope of slightly lower than one (0.86) likely due to re-apportionment of HOA mass to LOA,
332 but the correlation is still very high ($R=0.97$). In total, Figure D-3 indicates subtracting the LOA
333 contribution does not substantially impact the other components in the PMF solution.

334 In Panel C of Figure D-1, the mass fraction and identities of the components are
335 summarized for the PMF analysis with the fixed LOA contribution. The 5-component solution is
336 the final solution described in the main text. Similar to the original PMF analysis, a dramatic
337 increase in the correlation of HOA and rBC is observed when the CIOA component is resolved
338 in the 5-component solution (Panel D), and subsequent increases in the number of components
339 either marginally increase or decrease this correlation. This observation is consistent with
340 concluding that CIOA is distinct from the other components. In addition, the 6-component
341 solutions for the two PMF analyses are similar, which is expected since the LOA contribution in
342 both analyses is identical. The similarity indicates that holding the LOA contribution fixed does
343 not create unforeseen changes in the PMF analysis. The Q/Q_{exp} values for the various PMF
344 solutions are shown in Panels C and D. (Note: Q is the total sum of the squares of each residual
345 divided by its expected error, and Q_{exp} equals the degrees of freedom in the fitted data, which is
346 approximately the product of the number of rows and columns for the input mass spectral matrix.
347 In addition, F_{peak} is a parameter that explores different “rotations” of the PMF solution where
348 the component time series are made more different or the component mass spectra are made
349 more different [Ulbrich *et al.*, 2009].) For the final 5-component solution a reasonable Q/Q_{exp}
350 value of 1.9 is obtained (Panel D). A Q/Q_{exp} value near one indicates that the assumptions of the

351 bilinear PMF model are appropriate and that the estimation of the errors for the input data is
352 accurate.

353 Figure D-4 shows the value of Q/Q_{exp} as a function F_{Peak} for the 5-component solution
354 with the fixed LOA contribution. Minimum Q/Q_{exp} values are observed for F_{Peak} equal to zero.
355 In addition, the correlation of the HOA component time series with that of the external tracer
356 rBC does not improve for non-zero F_{Peak} values. Thus, the 5-component solution corresponding
357 to $F_{\text{Peak}} = 0$ is the final solution selected for further discussion in the main text. Additionally,
358 Figure D-5 summarizes an analysis of the residuals for the final 5-component solution (with
359 $F_{\text{Peak}} = 0$).

360 It was recently shown by Mohr et al. [2011] that HOA and cooking organic aerosol can
361 be distinguished by their relative values of AMS f_{55} and f_{57} , which represent the fraction of the
362 total OA at m/z 55 and m/z 57, respectively. The differences in f_{55} and f_{57} between the two
363 components are driven by the relative prominence of the oxygenated fragments $\text{C}_3\text{H}_3\text{O}^+$ and
364 $\text{C}_3\text{H}_5\text{O}^+$ in the mass spectra of cooking organic aerosol. For the CalNex PMF solution, the mass
365 spectrum of the CIOA component (Figure 4A) shows the presence of these fragments, and they
366 represent a greater fraction of the signal at m/z 55 and m/z 57 for CIOA versus HOA. To further
367 explore if the mass spectra of HOA and CIOA for CalNex are consistent with previously
368 published studies, f_{55} versus f_{57} data for the two PMF components are plotted in Figure D-6A.
369 The lines in Figure D-6A are taken directly from Mohr et al. [2011] and represent linear fits of
370 f_{55} versus f_{57} data from previously reported cooking organic aerosol and HOA PMF components
371 as well as from cooking and traffic source emission studies. Also plotted in Figure D-6A is f_{55}
372 versus f_{57} for the total time-resolved organic mass spectra after subtracting out the contribution of
373 SV-OOA and LV-OOA (the axes are labeled with 'OOA sub' to indicate this subtraction) so the

374 data reflects only contributions from primary components. The resulting data points are colored
375 by the relative contribution of CIOA. The CIOA component lies along the line for cooking
376 source emissions, consistent with the description of CIOA as ‘cooking-influenced’ aerosol. The
377 HOA component at CalNex does not match the linear fits for HOA as well, but it does lie within
378 the range of the raw values used for the regression analysis in Mohr et al. [2011]. Since the
379 differences between CIOA and HOA in f_{55} versus f_{57} space are related to oxygenated fragments,
380 it is possible that the higher HOA oxidation in our study may lead to changes in the HOA data
381 points in this space and explain the difference between the CalNex HOA component and the
382 linear fits from Mohr et al. [2011]. For the time-resolved data, when CIOA has a large
383 contribution the data in f_{55} versus f_{57} space resembles cooking emission sources, whereas when
384 the CIOA contribution is low the data more closely resemble the expected HOA values. This
385 result supports the conclusion that the organic aerosol at the Pasadena ground site had substantial
386 contributions from both primary combustion and cooking sources. In addition, the CIOA and
387 HOA components contain spectral characteristics that are similar to analogous components and
388 primary emissions from previous studies.

389 The robustness of the PMF CIOA component is verified by comparing the CIOA time
390 series against the concentration predicted for cooking organic aerosol using the estimation
391 method presented in Mohr et al. [2011], which is derived from several previous source emission
392 and PMF studies. Briefly, this method calculates the amount of cooking organic aerosol by
393 scaling up the measured organic concentration at m/z 55 after accounting for possible
394 interferences from other primary and secondary OA. A scatter plot of PMF CIOA versus the
395 concentration calculated from m/z 55 is shown in Figure D-6B. For the entire CalNex data set
396 the slope is near one (0.98), but the correlation is not particularly strong ($R=0.63$). The data in

397 Figure D-6B are also colored by the amount of organic mass measured at m/z 44, which is an
398 indicator for the relative influence of SOA [Aiken *et al.*, 2009; Mohr *et al.*, 2011; Ng *et al.*,
399 2011]. It is observed that many periods with high m/z 44 exhibit a worse correlation, which is
400 expected given the known contribution of SOA compounds to m/z 55 as already mentioned.
401 Mohr *et al.* [2011] account for this interference by assuming the interference from SOA at m/z 55
402 is proportional to the amount of signal at m/z 44. This assumption may not hold in cases when
403 multiple SOA sources with different amounts of aging are contributing to the organic mass at m/z
404 44 and m/z 55 resulting in varying proportionalities. To minimize the impact of this interference
405 the data is fit a second time using only periods when m/z 44 is below its median value, which
406 results in a higher correlation ($R=0.88$) and lower slope (0.76). The difference of less than 25%
407 in average concentration represents reasonable agreement between the two methods, and can be
408 mostly explained by the 20% uncertainty in the scaling factor used in Mohr *et al.* [2011] to
409 calculate cooking organic aerosol from the organic mass measured at m/z 55. While the
410 possibility that PMF is apportioning non-cooking OA to the CIOA mass cannot be completely
411 ruled out, the comparison presented in this paragraph indicates a large majority of CIOA is from
412 cooking sources.

413 The time series of the PMF components can be further analyzed using an autocorrelation
414 plot in which the correlation of each factor with itself is calculated for various time offsets. In
415 this analysis species with high frequency fluctuations in concentrations (i.e., having many
416 ‘spikes’ in their time series) will have a steep profile and vice versa. As seen in Figure D-7 the
417 autocorrelation profiles of SV-OOA and LV-OOA are the flattest, which is consistent with the
418 more regional nature of these components. Furthermore, the observation that the LV-OOA
419 profile is less steep than SV-OOA supports the association of LV-OOA with aged secondary

420 organic aerosol that is expected to vary in concentration on longer time scales than fresh
421 secondary organic aerosol. In contrast, the HOA component has a steep profile at the shortest
422 times and a flatter profile at longer times indicating that this component has both local and
423 regional sources. This finding is not surprising given that some HOA is generated by local traffic
424 in the Pasadena area, but HOA is also advected to Pasadena from other areas in the LA Basin.
425 Interestingly, the CIOA component appears to be more dominated by local sources in
426 comparison to HOA, which may be related to the lower wind speeds and reduced advection in
427 the evenings when CIOA is highest in concentration. Alternatively, if the atmospheric lifetime of
428 CIOA was shorter than HOA, then that would also result in a relatively steeper profile for CIOA.
429 As described previously, the LOA component time series varies rapidly with time, and thus
430 displays the steepest profile in the auto-correlation plot, supporting the description of this factor
431 as 'local' organic aerosol.

432 The correlations of the PMF component time series with various other species measured
433 at the Pasadena ground site are summarized in Table D-1, and generally support the description
434 of the components discussed in the main text. For the readers convenience the correlations are
435 also summarized in a bar graph in Figure D-8. The most notable correlations are summarized in
436 this section. First, the primary combustion emissions tracers EC, rBC, NO_x, CO, and primary
437 hydrocarbons correlate with HOA. A correlation is also observed between HOA and PM_{1.15} Zn.
438 The correlation with Zn may be explained by abrasion of tire-tread by road surfaces, which is
439 thought to be a major source of Zn in urban atmospheres [*Adachi et al.*, 2004; *Councell et al.*,
440 2004; *Hjortenkrans et al.*, 2007; *Salma et al.*, 2006], although a comparably strong correlation is
441 not observed for other metals that have been linked to brake wear or road dust. NO_x does not
442 exhibit as strong a correlation with HOA as the other primary combustion tracers, and this

443 observation is probably due to the short lifetime of NO_x and the multi-hour transport time for
444 advection of HOA from the more western portion of the LA basin to the Pasadena ground site.
445 Moreover, NO_y correlates better with HOA than NO_x (R of 0.63 versus 0.45) likely because
446 oxides of nitrogen emitted by vehicles have a longer atmospheric lifetime when measured as
447 NO_y . Taken together, the correlations of the various species with HOA suggest that primary
448 vehicular emissions are the dominant source for this component. The primary combustion tracers
449 do not correlate with CIOA with the exception of the moderate correlation with CO (R = 0.43).
450 The correlations of HOA and CIOA with CO, as well as the correlation of HOA with EC are
451 discussed in further detail in Section 3.2.3 of the main text. Previous work by Sun et al. [2011]
452 reported that the AMS fragments $\text{C}_5\text{H}_8\text{O}^+$ and $\text{C}_6\text{H}_{10}\text{O}^+$ showed high correlations specific to
453 cooking organic aerosols, and this correlation is also observed for the PMF results presented
454 here. However, these oxygenated fragments show an even stronger correlation with SV-OOA,
455 which suggests that these tracers are not highly specific to cooking OA.

456 The SV-OOA component correlates strongly with acetaldehyde and odd-oxygen.
457 Acetaldehyde is a well-known secondary photochemical product with direct emissions that are
458 quickly overwhelmed by secondary formation within hours of processing [Sommariva et al.,
459 2011; Washenfelder et al., 2011], and odd-oxygen is a useful tracer for the oxidation of VOCs
460 [Herndon et al., 2008; Wood et al., 2010]. Thus, the strong correlation of these species with SV-
461 OOA is consistent with treating this component as a surrogate for ‘fresh’ SOA. Previous
462 publications have reported a correlation between nitrate and SV-OOA at some locations [e.g.
463 DeCarlo et al., 2010; Ulbrich et al., 2009], but a similar correlation is not observed at the
464 Pasadena ground site. The lack of correlation is likely due to the higher temperatures and
465 reduced RH in the afternoon at the ground site, which lead to the volatilization of ammonium

466 nitrate at the same time SV-OOA concentrations are typically increasing. For LV-OOA a strong
467 correlation with sulfate is observed that is consistent with other studies [*DeCarlo et al.*, 2010;
468 *Sun et al.*, 2011; *Ulbrich et al.*, 2009] and has been previously attributed to the non-volatile
469 nature of both sulfate and LV-OOA as well as the formation of these species from secondary
470 sources. The correlation of OOA with odd-oxygen is discussed in detail in Section 3.2.4 of the
471 main text.

472 $PM_{1.15}$ Ti exhibits a correlation with LOA ($R = 0.63$). A strong peak in LOA
473 concentrations occurred on the morning of June 5th (PDT), and a similar event is seen in the
474 $PM_{1.15}$ Ti time series. Paint-pigment has been identified as a source of titanium particles in the
475 atmosphere [*Alpert et al.*, 1981], and amines are often used in paint application and surface
476 coatings [*Unnikrishnan et al.*, 2006]. Still, a lack of corroborating evidence prevents assigning
477 LOA to any specific source with confidence.

478 Several other tracers are listed in Table 2. In particular, acetonitrile is a common tracer
479 for biomass burning emissions, and a lack of correlation with acetonitrile is initially observed (R
480 ≤ 0.1). In contrast, after filtering out the acetonitrile data with concentrations above 1.5 ppmv to
481 remove the possible influence of local solvent use, a moderately strong correlation is observed
482 with CIOA ($R = 0.67$) despite the relatively low acetonitrile concentrations that are near
483 background levels. This correlation may be due to barbecuing with biomass fuels such as
484 charcoal. Indicators for marine influenced air masses used in this study are dimethyl sulfide
485 (DMS) and PALMS sea salt volume concentrations [*Malm et al.*, 1994; *Zorn et al.*, 2008], as
486 well as methanesulfonic acid (MSA) [*Gaston et al.*, 2010], which is measured by the PALMS as
487 a relative concentration [*Froyd et al.*, 2010]. However, the low correlations observed between

488 these indicators and all the PMF components provide little information about the role of marine
489 sources.

490 The concentrations for a variety of organic species were quantified by 2DTAG
491 measurements. The correlations between a selection of these species and the PMF components
492 are summarized in Table D-2. For a variety of polycyclic aromatic hydrocarbons (PAHs),
493 phytane, dibenzofuran, and the lowest-volatility measured Hopane the correlation with HOA is
494 strongest, which is not surprising given that these compounds are characteristic of primary
495 vehicle emissions [*Schauer et al.*, 1999a; 2002a; *Williams et al.*, 2010]. In addition, several
496 ketones and undecylbenzene exhibit a higher correlation with HOA than the other PMF
497 components, and it is known that ketones and aromatics are found in tailpipe emissions from gas
498 and diesel vehicles [*Jakober et al.*, 2006; *Jakober et al.*, 2008]. However, some species such as
499 chrysene, a PAH, are clearly primary emissions, but show a similar level of correlation with both
500 HOA and SV-OOA. This observation may be due to the similar time-of-day that HOA and SV-
501 OOA concentrations peak (13:00 – 14:00 versus 14:00 – 15:00), and the lower time resolution of
502 the 2DTAG, which averaged samples over 85 minutes. Thus, periods of high HOA and SV-OOA
503 concentrations may appear to occur close to simultaneously on the time scale of the 2DTAG,
504 which unfortunately adds uncertainty to the comparison of the 2DTAG data against the PMF
505 components. This concern may also explain the apparent correlation of HOA with some
506 oxygenates. Considering only the compounds that have the highest correlation with SV-OOA,
507 this component tracks the concentrations of several phthalic acids and other compounds
508 structurally similar to phthalates. This finding is consistent with the description of SV-OOA
509 presented here since phthalic acids are well-known tracers for SOA from anthropogenic VOCs
510 [*Williams et al.*, 2010]. In contrast, the LV-OOA component exhibits weaker correlations with

511 2DTAG compounds ($R < 0.5$), which is likely due to the poor transfer efficiency of highly
512 oxidized compounds that is typical in GC systems [Williams *et al.*, 2006].

513 For CIOA, a weak correlation is observed with pentadecane. It should be noted that n-
514 alkanes have been identified in emissions from meat charbroiling [Schauer *et al.*, 1999b], but
515 also from gasoline and diesel vehicle emissions [Schauer *et al.*, 1999a; 2002a]. Thus, the
516 correlation with pentadecane does not distinguish between possible cooking or vehicle emission
517 sources. Using one-dimensional TAG Williams *et al.* [2010] observed in Riverside that several
518 alkanolic acids and alkylnitriles were the highest contributors to food cooking aerosols, although
519 it is recognized that some of these compounds can have secondary sources. For CalNex,
520 hexadecanoic acid correlates most strongly with SV-OOA rather than CIOA suggesting that
521 secondary sources of alkanolic acids are influencing the air mass above the ground site.
522 However, if the correlation analysis is limited to only periods with low SV-OOA concentrations
523 (less than the median) then CIOA does exhibit the strongest correlation with hexadecanoic acid.
524 The alkylnitriles correlate more strongly with other PMF components than CIOA, which
525 suggests that these compounds may not be good markers for cooking emissions in Pasadena
526 possibly because they are also associated with vehicle emissions [Williams *et al.*, 2010].
527 Cholesterol and oleic acid are known to be present in cooking emissions as well [Schauer *et al.*,
528 1999b; 2002b]. For cholesterol its size and alcohol functionality limits the sensitivity of 2DTAG.
529 Oleic acid can be measured by the 2DTAG, but in the field its mass spectrum is difficult to
530 distinguish from the background unresolved complex mixture.

531 Many of correlations observed with the 2DTAG compounds are consistent with the
532 designations of the PMF components presented here, although there are two serious caveats.
533 First, a substantial number of compounds show correlations with HOA and SVOOA that are

534 similar in strength (e.g., Chrysene), which is likely due to the similar diurnal cycles of HOA and
535 SVOOA. Second, for CIOA a correlation with hexadecanoic acid is observed, but correlations
536 with other cooking-related compounds are either weak (alkylnitriles) or cannot be determined
537 because of instrument limitations (cholesterol & oleic acid).

538 **Table D-1:** Correlations (R values) of PMF component time series with the time series of tracers
 539 measured at the Pasadena ground site during CalNex. Tracers have been grouped for clarity, and
 540 important correlations for each tracer are boldfaced and underlined. Campaign average mass
 541 concentrations for each PMF component are also shown in the second row.

542

Tracer	HOA	CIOA	LOA	SVOOA	LVOOA	
Campaign Avg. Conc. ($\mu\text{g m}^{-3}$)	0.82	1.21	0.34	2.43	2.26	
rBC	<u>0.70</u>	0.07	0.36	0.40	0.35	Primary
EC	<u>0.71</u>	0.03	0.43	0.46	0.33	Primary
NO _x	0.45	0.26	0.28	0.01	-0.07	Primary
Benzene	<u>0.71</u>	0.37	0.44	0.37	0.42	Primary
CO	<u>0.59</u>	0.43	0.41	0.49	0.41	Primary
Zn (PM _{1.15})	<u>0.52</u>	-0.17	0.33	0.14	0.33	Primary
Acetonitrile ^a	0.47	<u>0.67</u>	0.47	0.03	0.48	Primary
Propane	<u>0.65</u>	0.17	0.49	0.44	0.42	Primary
n-Butane	<u>0.58</u>	0.13	0.48	0.36	0.38	Primary
Isobutane	<u>0.59</u>	0.21	0.51	0.37	0.42	Primary
n-Pentane	<u>0.66</u>	0.19	0.57	0.33	0.36	Primary
Isopentane	<u>0.72</u>	0.26	0.53	0.44	0.35	Primary
Ti (PM _{1.15})	0.33	-0.08	<u>0.63</u>	0.05	0.11	Primary
NO _y	<u>0.63</u>	0.25	0.40	0.37	0.23	Primary + Secondary
O _x	0.28	0.10	0.04	<u>0.73</u>	0.17	Secondary
Acetaldehyde	0.64	0.19	0.26	<u>0.82</u>	0.39	Secondary
DMS	0.06	0.11	0.03	-0.08	-0.04	Marine
PALMS Sea Salt Vol. Conc. (PM ₁)	0.17	0.08	0.04	-0.20	-0.06	Marine
MSA	-0.10	-0.03	-0.10	-0.18	-0.34	Marine
Chloride	0.16	0.01	0.13	0.01	0.31	AMS
Nitrate	0.38	-0.03	0.44	0.12	<u>0.70</u>	AMS
Ammonium	0.40	0.00	0.43	0.19	<u>0.77</u>	AMS
Sulfate	0.49	0.02	0.36	0.39	<u>0.69</u>	AMS
C ₅ H ₈ O ⁺	0.58	0.47	0.23	<u>0.86</u>	0.44	AMS
C ₆ H ₁₀ O ⁺	0.56	0.60	0.24	<u>0.71</u>	0.36	AMS

^a Correlations correspond to only acetonitrile concentrations below 1.5 ppbv to eliminate potential contributions from nearby solvent use.

543 **Table D-2:** Correlations (R) of PMF components with 2DTAG compounds. The highest
 544 correlation for each tracer is boldfaced and underlined. 2DTAG data are only available from 6/11
 545 - 6/16. Only compounds with R > 0.5 are shown.

2DTAG Compound	HOA	CIOA	LOA	SVOOA	LVOOA	
Phenanthrene	<u>0.60</u>	0.47	0.29	0.39	-0.01	H
1-Methylphenanthrene	<u>0.54</u>	0.48	0.22	0.46	0.03	Y
2-Methylphenanthrene	<u>0.56</u>	0.34	0.23	0.42	-0.10	D
1-Methylanthracene	<u>0.58</u>	0.41	0.26	0.46	-0.01	R
2-Methylanthracene	<u>0.54</u>	0.35	0.25	0.47	0.03	O
2-Phenylnaphthalene	<u>0.58</u>	0.28	0.36	0.48	0.14	C
Chrysene	0.58	0.27	0.24	<u>0.61</u>	0.21	A
Lowest-Volatility Hopane	<u>0.59</u>	0.38	0.41	0.49	0.15	R
Pentadecane	0.36	<u>0.52</u>	0.32	0.22	0.23	B
Octadecane	0.50	0.30	0.18	<u>0.51</u>	0.17	O
Phytane	<u>0.59</u>	0.29	0.31	0.45	0.15	N
Octacosane	0.46	0.05	0.08	<u>0.51</u>	0.10	S
Nonacosane	0.51	0.09	0.28	<u>0.71</u>	0.31	
Triacontane	0.52	0.05	0.22	<u>0.60</u>	0.25	
Hentriacontane	0.49	0.15	0.18	<u>0.61</u>	0.39	
Decylbenzene	0.54	0.34	0.27	<u>0.58</u>	0.20	
Undecylbenzene	<u>0.54</u>	0.36	0.25	0.48	0.11	
3-Methylphthalic Acid	0.51	0.03	0.12	<u>0.86</u>	0.20	O
4-Methylphthalic Acid	0.54	0.09	0.18	<u>0.81</u>	0.03	X
Dimethylphthalic Acids	0.53	0.03	0.13	<u>0.82</u>	0.13	Y
Chlorophthalic Acid	0.49	0.14	0.23	<u>0.74</u>	0.16	G
1H-Indene-1,3(2H)-dione	0.42	-0.05	0.06	<u>0.80</u>	0.24	E
delta-Decalactone	0.47	0.05	0.12	<u>0.72</u>	0.13	N
delta-Hexadecalactone	0.53	0.20	0.28	<u>0.76</u>	0.35	A
Pentadecanone	0.52	0.37	0.38	<u>0.54</u>	0.23	T
Hexadecanone	0.58	0.31	0.26	<u>0.64</u>	0.31	E
Heptadecanone	0.59	0.39	0.33	<u>0.64</u>	0.37	S
Octadecanone	<u>0.57</u>	0.21	0.31	0.54	0.07	
Nonadecanone	<u>0.50</u>	0.19	0.39	0.49	0.14	
Trimethylpentadecanone	<u>0.62</u>	0.22	0.39	0.59	0.36	
Fluorenone	0.47	0.21	0.10	<u>0.57</u>	0.24	
Hydroxyfluorenone	<u>0.54</u>	0.47	0.30	0.53	0.34	
Naphthalic Anhydride	0.49	0.11	0.17	<u>0.67</u>	0.17	
Benzophenone	0.66	0.37	0.36	<u>0.67</u>	0.43	
Benzyl Benzoate	0.68	0.35	0.38	<u>0.73</u>	0.30	
Isopropyl Myristate	<u>0.67</u>	0.00	0.62	0.45	0.15	
Dibenzofuran	<u>0.64</u>	0.39	0.32	0.47	0.05	
Hexadecanoic Acid (SV-OOA<2.4 µg/m3)	0.51	<u>0.66</u>	0.55	0.35	0.43	
Tetradecanenitrile	0.55	0.23	0.48	<u>0.59</u>	0.36	Nitrogen- Containing
Hexadecanenitrile	0.46	0.34	0.28	<u>0.59</u>	0.47	
Octadecanenitrile	0.44	0.35	0.28	<u>0.62</u>	0.48	
Phthalimide	0.56	0.23	0.22	<u>0.78</u>	0.36	
Homophthalimide	0.50	-0.01	0.13	<u>0.84</u>	0.22	

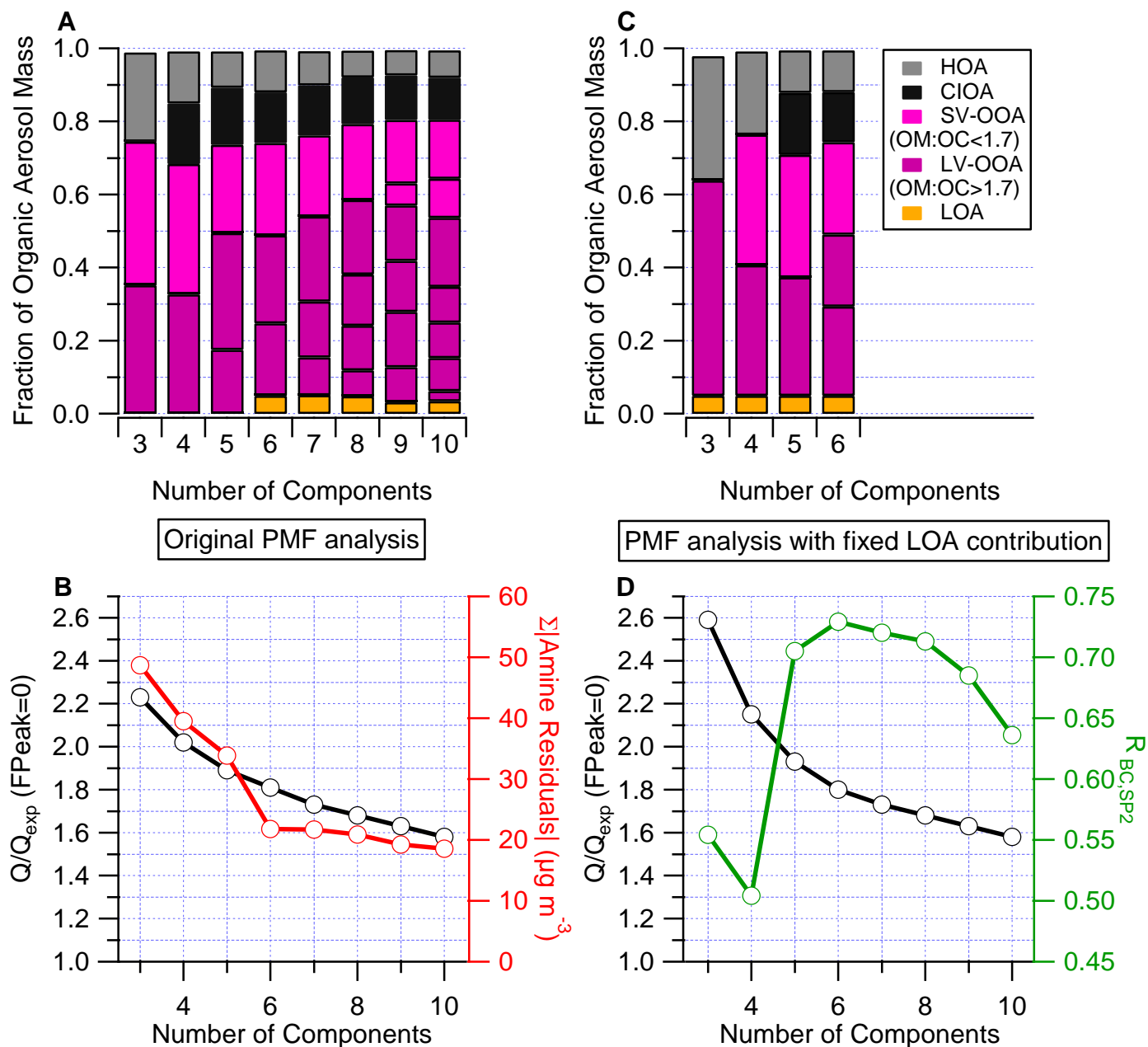


Figure D-1: (A) Stacked bar plot showing the relative contribution of each PMF component as a function of the number of components. (B) Q/Q_{exp} for the original PMF analysis (black line and markers) and the sum of the absolute values of the residuals for selected amine-containing ions (red line and markers). Both data traces are displayed as function of the number of components. (C) The relative contribution of each PMF component, similar to the figure on the top left, but for PMF solutions where the LOA contribution to the OA spectra is fixed. (D) Q/Q_{exp} for the PMF analysis with a fixed contribution from the LOA component versus number of components (black line with markers). The correlation of HOA with rBC is also displayed (green line and markers).

547
548

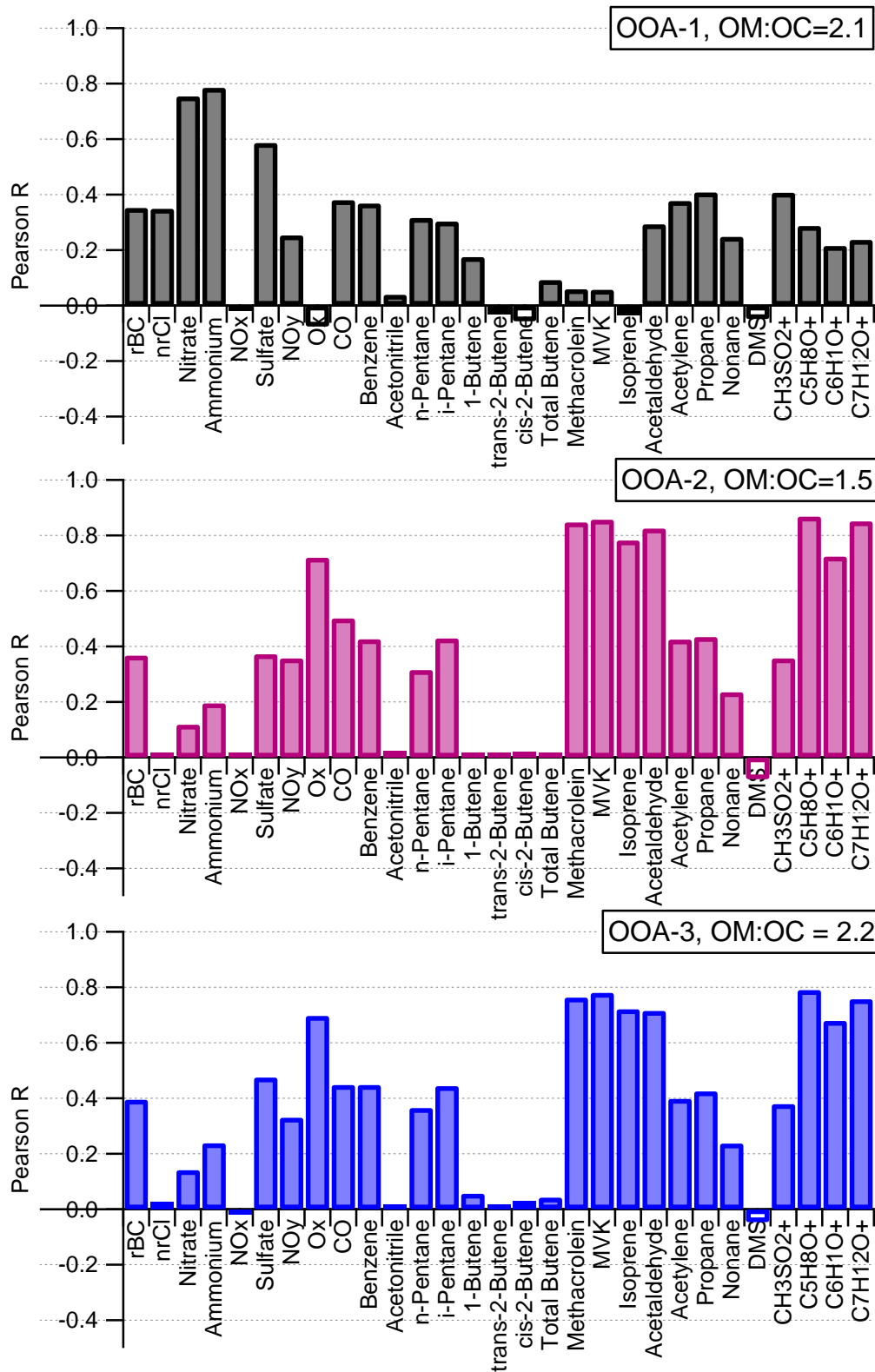


Figure D-2: Summary of correlations for the OOA components identified in the 6-component PMF solution (without a fixed LOA contribution to OA). The OM:OC ratio is indicated in the upper-right corner of each panel.

549
550

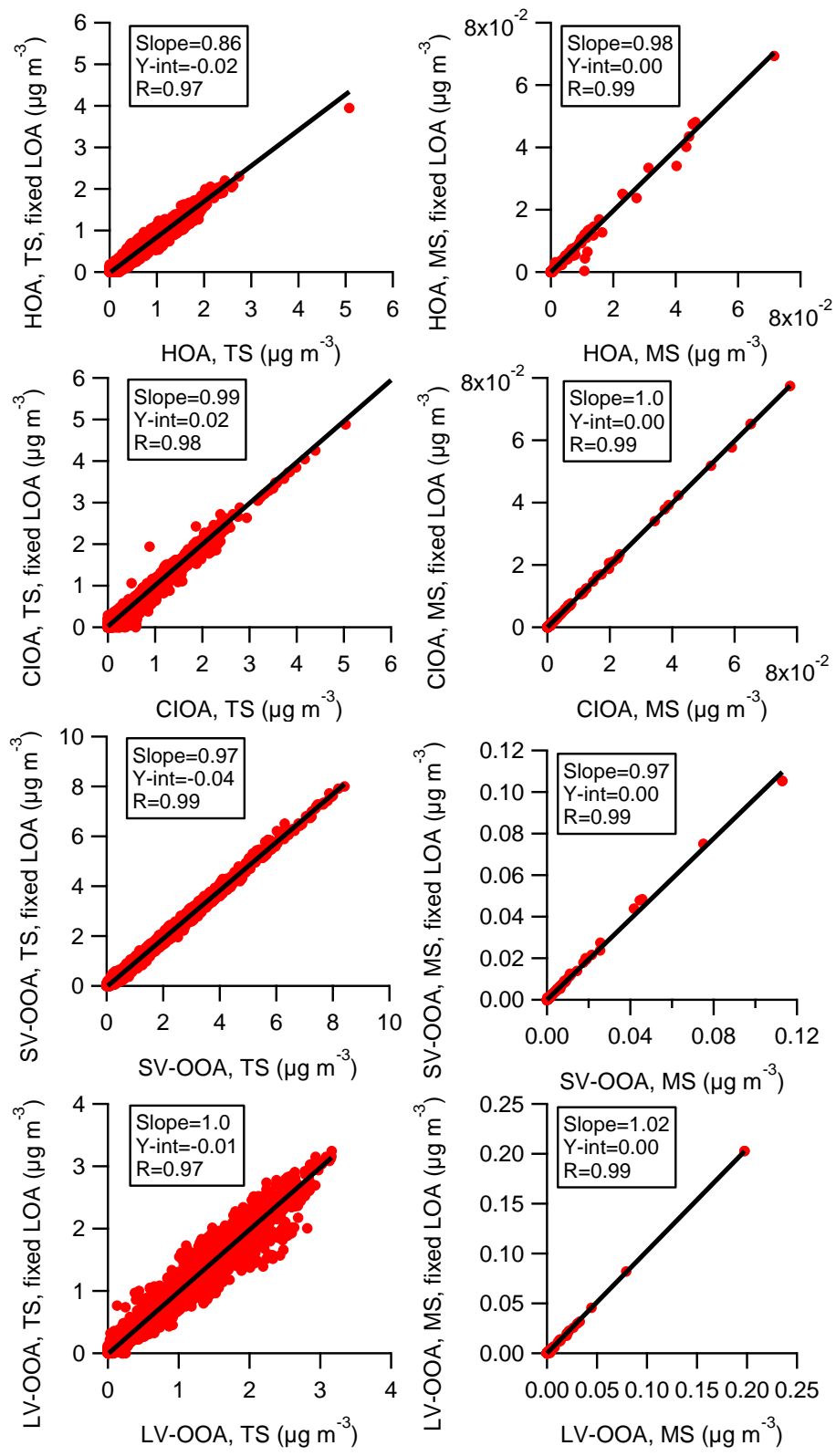


Figure D-3: Scatter plots of each component for the 4-component PMF solution and the 5-component PMF solution with a fixed LOA contribution. The left column contains plots for the time series and the right column contains plots for the mass spectra.

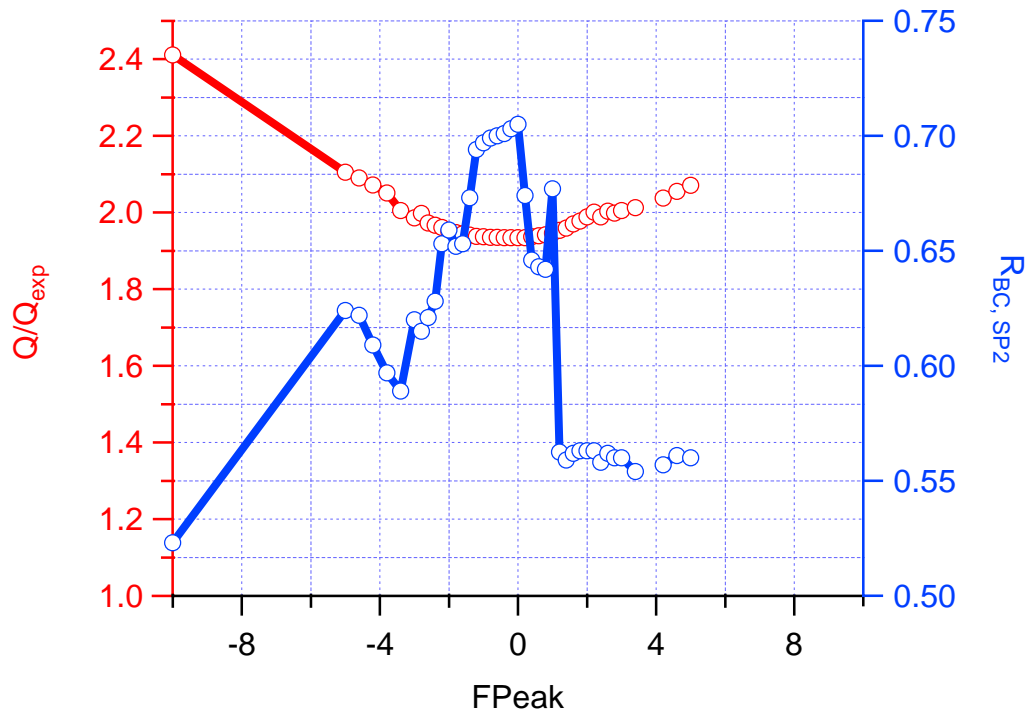


Figure D-4: (Left Axis) Q/Q_{exp} for the selected 5-component solution with the fixed LOA contribution plotted as a function of FPeak. **(Right Axis)** Correlation between HOA and rBC from the SP2 as a function of FPeak for the selected 5-component solution.

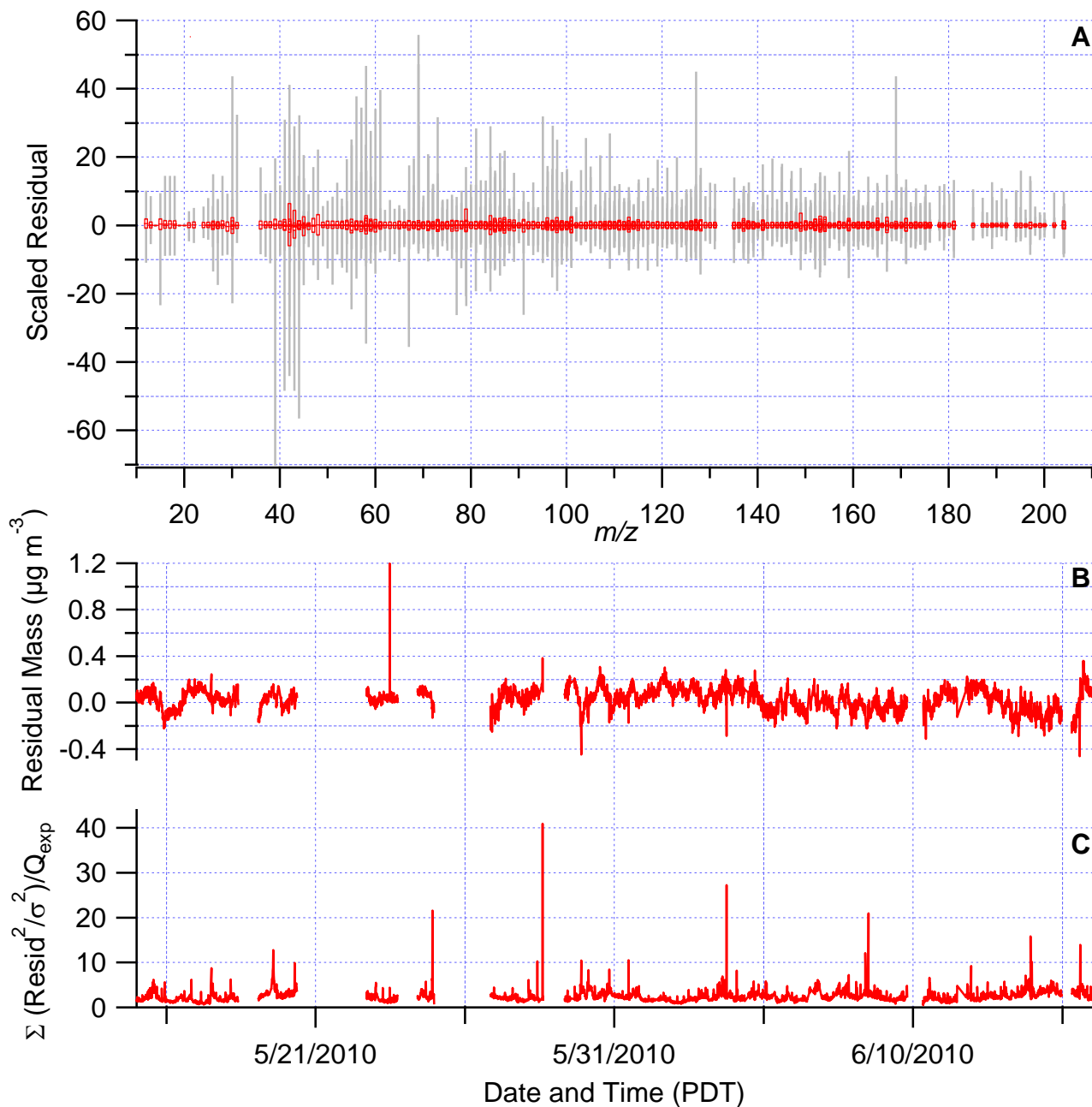


Figure D-5: (A) Box-and-whisker plot of residuals for each organic ion scaled to the predicted error from the error matrix. The boxes represent that 25th and 75th percentiles, and the whiskers represent the 5th and 95th percentiles. (B) Time series of the residual organic mass (= measured mass – reconstructed mass from PMF). (C) Time series of Q/Q_{exp} (i.e., the residual squared divided by the predicted error squared, which is then normalized to Q_{exp}).

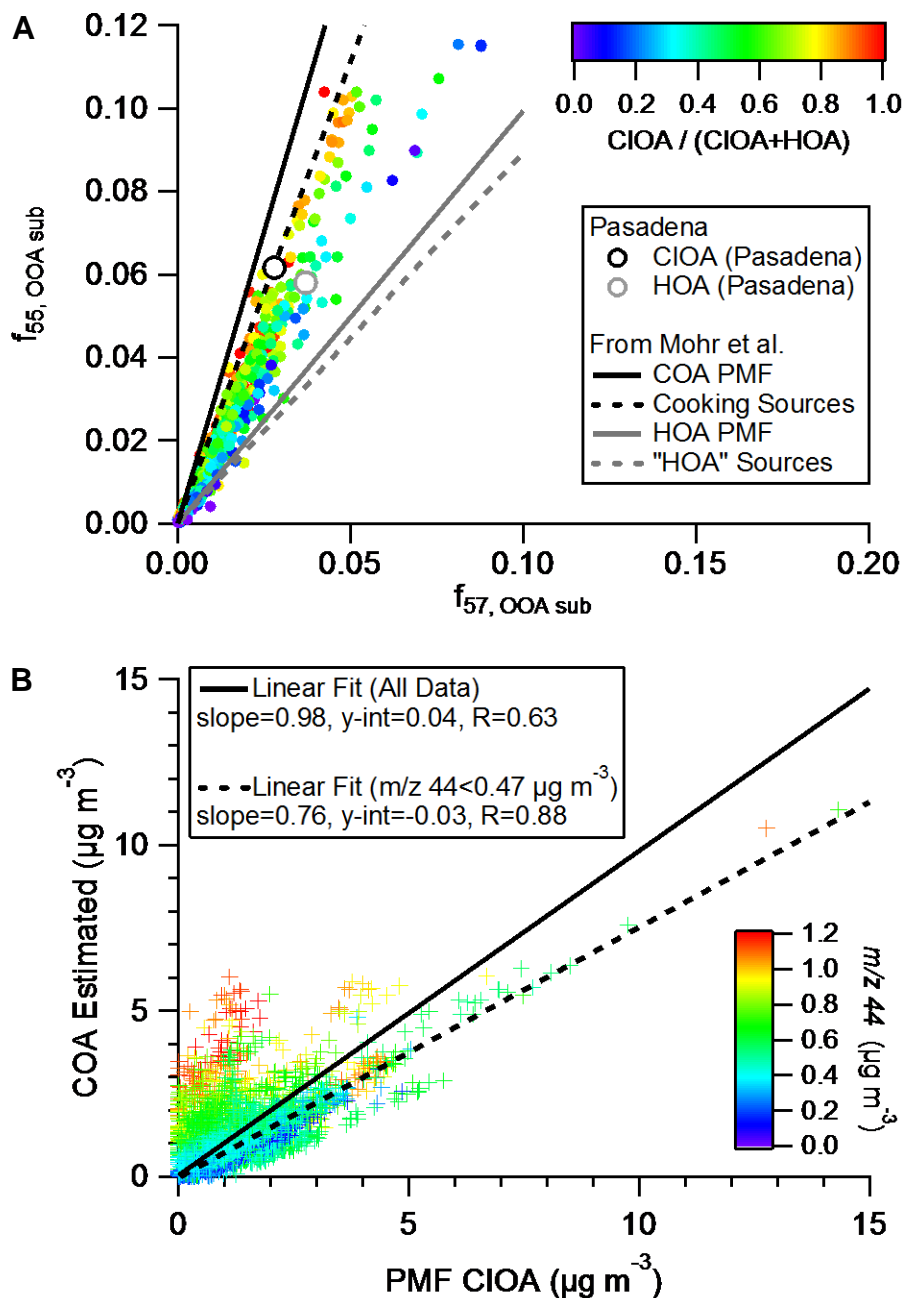


Figure D-6: (A) Scatter plot of $f_{55, OOA\ sub}$ versus $f_{57, OOA\ sub}$ colored by the relative amount of CIOA (markers). Also shown is f_{55} versus f_{57} for CIOA (black circle) and HOA (gray circle). The lines represent linear fits of f_{55} versus f_{57} data from previously reported cooking organic aerosol (COA) and HOA PMF factors (solid lines) as well as from cooking and traffic source emission studies (dashed lines). The linear fits are reproduced from Mohr et al. [2011]. (B) Scatter plot of CIOA concentration determined by PMF vs. COA concentration determined using the method of Mohr et al. Also shown are the linear regressions for the entire data set (solid line) and for periods when $m/z\ 44$ was below its median concentration of $0.47\ \mu\text{g m}^{-3}$ (dashed line).

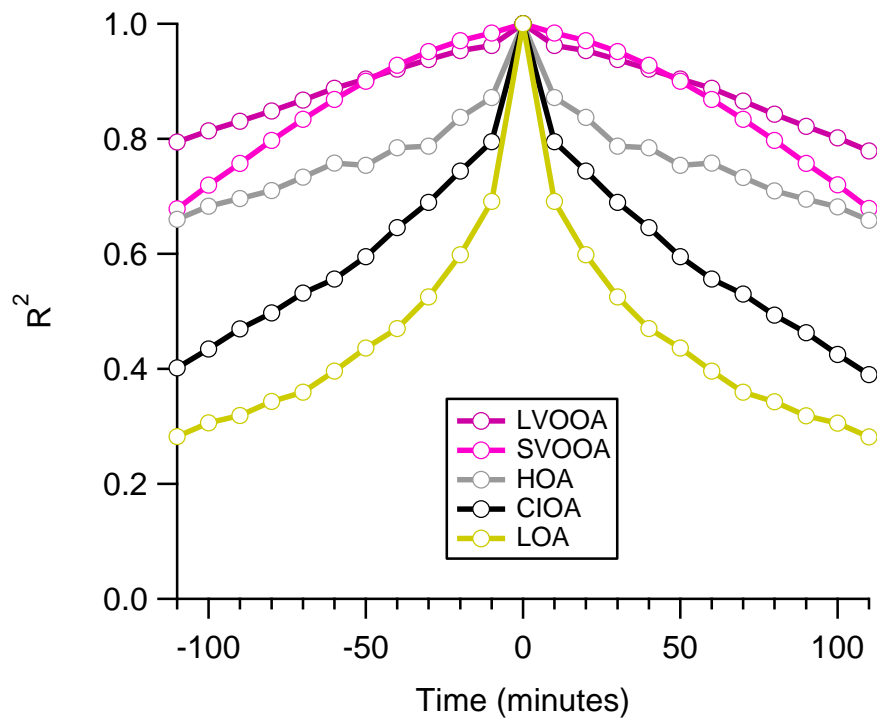


Figure D-7: Auto-correlations for the PMF component time series over +/-110 minutes.

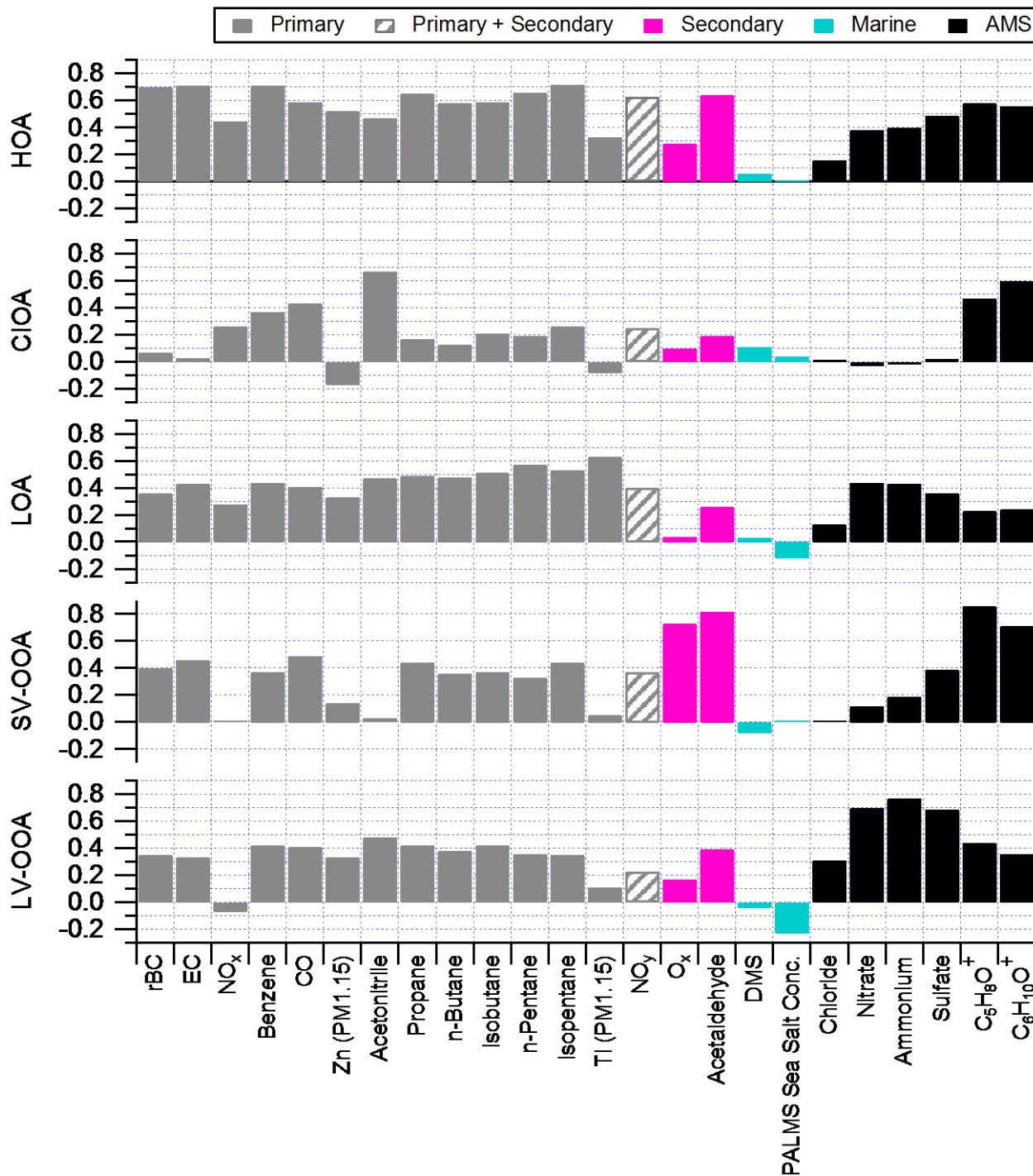


Figure D-8: Bar graph summarizing the correlations of the PMF factors with key tracer species. The correlations are taken from Table D-1. The bars are colored by the tracer classification. Note: Acetonitrile correlations correspond to only acetonitrile concentrations below 1.5 ppbv to eliminate potential contributions from nearby solvent use.

556 **Section E: Evaluation of Photochemical Age Error**

557 Photochemical age is a quantity developed as a metric for parcels of air arriving at remote
558 receptors sites, and it is derived by assuming that the parcel is decoupled from fresh emissions as
559 it is transported [*Kleinman et al.*, 2007; *Parrish et al.*, 2007]. However, the Pasadena ground site
560 is not a remote receptor site, and it is impacted by pollutants that have been emitted recently as
561 well as transported from more distant locations. The goal of this section is to evaluate the
562 potential errors that result from calculating the photochemical age for an air parcel that is
563 receiving continued additions of pollutants as it is transported to the measurement location.

564 A simple model was built that calculates the observed photochemical age based on a
565 given distribution of ages within an air parcel. For the dense urban region of Los Angeles it has
566 been assumed that emissions are constant as an air mass is advected from the coastline to the
567 Pasadena site [*Washenfelder et al.*, 2011]. Under this assumption the weights of the ages in the
568 distribution will be equal, and the distribution will range from zero to two times the chosen
569 photochemical age. Thus, the model has only one input parameter: photochemical age. It is
570 emphasized that in this analysis the flat distribution of ages assumed will not account for dilution
571 due to increasing boundary layer height, or diurnal cycles in emission rates and oxidant
572 concentrations. While different compounds could be used in the model, we specifically focus on
573 the case of photochemical age calculated from the ratio of 1,2,4-trimethylbenzene (1,2,4-TMB)
574 to benzene and utilize the emission ratios and OH reaction rates from Parrish et al. [2007]. The
575 model calculation involves: (1) calculating the concentrations of benzene and 1,2,4-TMB for
576 each age, (2) calculating the total contribution to benzene and 1,2,4-TMB concentrations from all
577 the age steps in the assumed age distribution, and (3) calculating the observed photochemical age
578 based on the VOC concentrations.

579 The results of the model are shown in Figure E-1 for a range of inputted photochemical
580 ages. For this analysis the error is defined as:

$$581 \quad \text{Error} = \frac{(Age)_{derived} - (Age)_{input}}{(Age)_{input}}$$

582 where $(Age)_{derived}$ is the photochemical age that would be derived from the observed VOC ratios,
583 and $(Age)_{input}$ is the age originally entered into the model. The error increases in magnitude with
584 photochemical age, and the age derived from the observed VOC ratios is systematically lower
585 than the actual average age. This trend can be explained by considering a hypothetical system
586 composed of a fresh and an aged air parcel of equal volumes. If each parcel started with the same
587 concentrations of emissions including benzene and 1,2,4-TMB, then when the two parcels are
588 mixed together the age of the mixed air should be simply the average of the ages of each
589 individual parcel. However, since both benzene and 1,2,4-TMB are depleted in the aged air
590 parcel due to chemical processing, in the photochemical age calculation the aged parcel has less
591 mathematical weight than the fresh parcel. This unequal weighting explains why observations, as
592 modeled here, will be systemically lower than the true average age of the mixed parcel.

593 The results reported here follow those previously published in Parrish et al. [2007], which
594 concludes that VOC ratios are a useful metric for determining photochemical ages even if mixing
595 of different air masses occurs. Based on the analysis presented here we estimate an error of
596 approximately 10%, corresponding to the mean photochemical age, which biases the observed
597 ages towards lower values. While this is a significant source of uncertainty, it should only impact
598 the accuracy of the observed photochemical ages and not relative comparisons for Pasadena (e.g.
599 weekday vs. Sunday), insofar as the distribution of ages is consistent. This requirement is likely
600 satisfied given the day-to-day similarity in meteorology and diurnal cycles at the ground site.

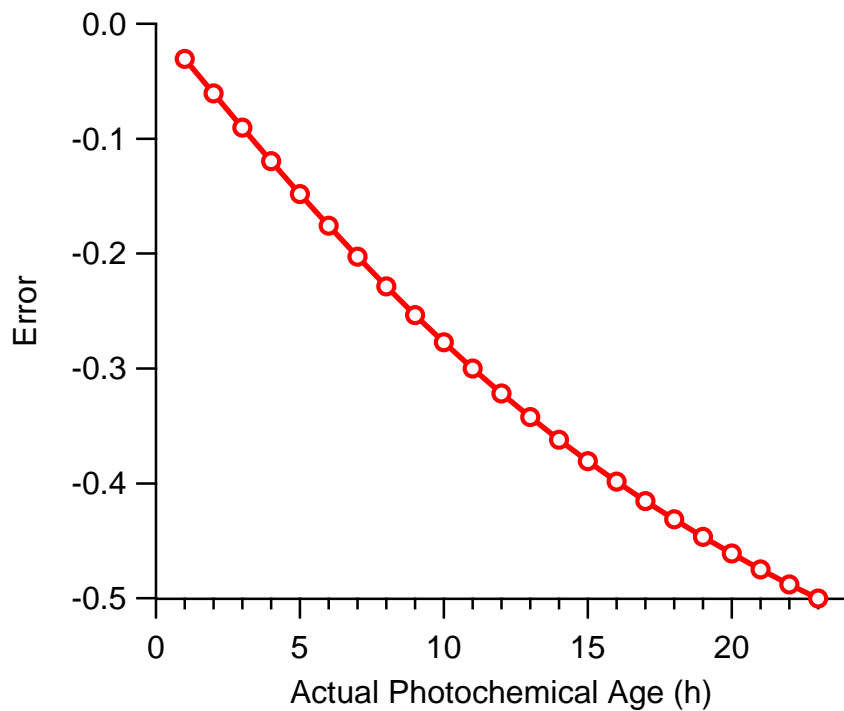


Figure E-1: The error in the photochemical age derived from the observed VOC ratios as a function of the actual photochemical age. The observed VOC ratios are simulated using the model described in Section E. The actual photochemical age is the mean of the different ages in the age distribution.

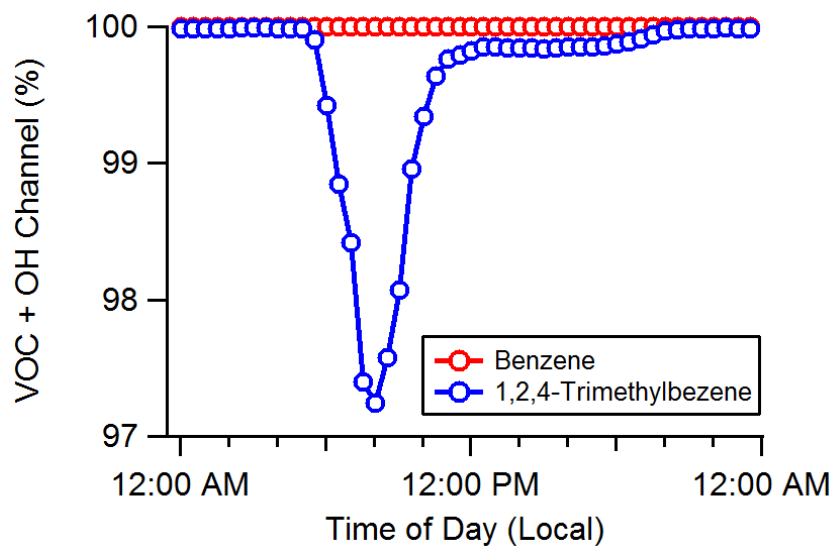


Figure E-2: Branching ratio between OH and Cl oxidation for benzene and 1,2,4-trimethylbenzene. The ratio was calculated using the relative OH to Cl concentrations as well as the corresponding rate constants from Young et al. [2013]. For both VOCs the oxidation chemistry is dominated by OH radicals, which is consistent with the method used to estimate photochemical age.

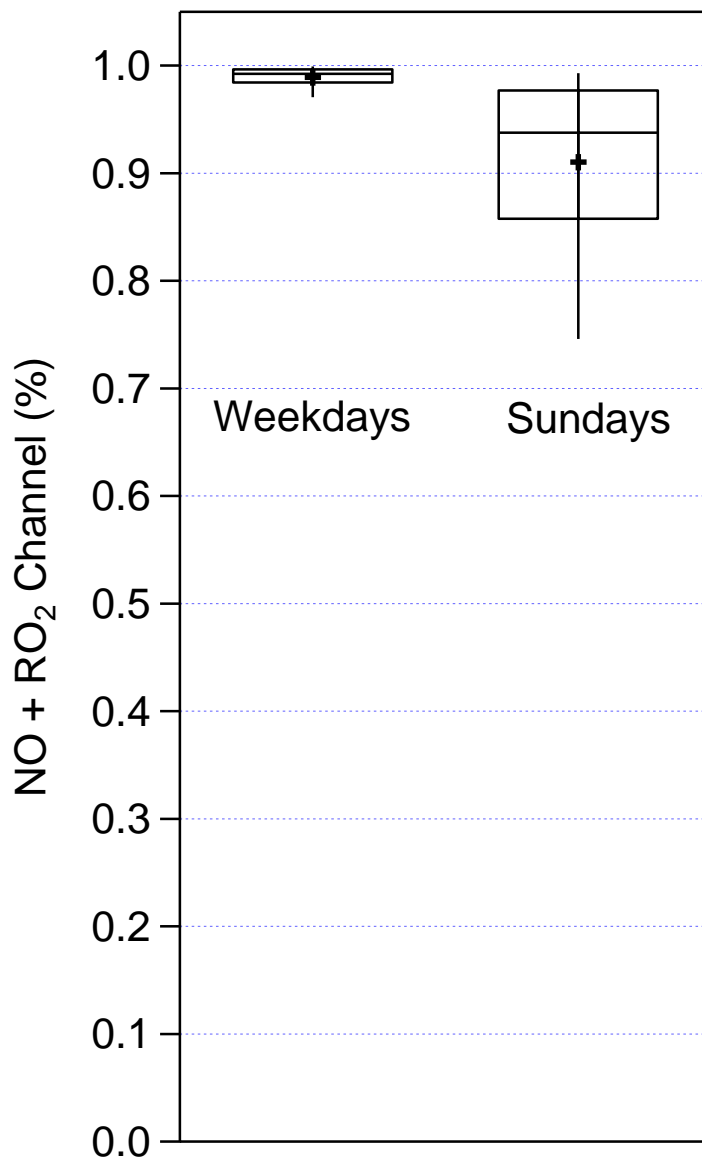


Figure F-1: Box-and-whiskers plot for the NO_x branching ratio on Weekdays vs. Sundays. Ratio was calculating using the method described in [Dzepina *et al.*, 2009]. Crosses represent the mean value.

605 **References**

- 606 Adachi, K., and Y. Tainosho (2004), Characterization of heavy metal particles embedded in tire dust,
607 *Environ. Int.*, 30(8), 1009-1017.
- 608
609 Aiken, A. C., et al. (2008), O/C and OM/OC ratios of primary, secondary, and ambient organic aerosols
610 with high-resolution time-of-flight aerosol mass spectrometry, *Environ. Sci. Technol.*, 42(12), 4478-4485.
- 611
612 Aiken, A. C., et al. (2009), Mexico City aerosol analysis during MILAGRO using high resolution aerosol
613 mass spectrometry at the urban supersite (T0) - Part 1: Fine particle composition and organic source
614 apportionment, *Atmos. Chem. Phys.*, 9(17), 6633-6653.
- 615
616 Alpert, D. J., and P. K. Hopke (1981), A determination of the sources of airborne particles collected
617 during the regional air-pollution study, *Atmos. Environ.*, 15(5), 675-687.
- 618
619 Chow, J. C., J. G. Watson, E. M. Fujita, Z. Q. Lu, D. R. Lawson, and L. L. Ashbaugh (1994), Temporal
620 and spatial variations of pm(2.5) and pm(10) aerosol in the Southern California Air-Quality Study, *Atmos.*
621 *Environ.*, 28(12), 2061-2080.
- 622
623 Councill, T. B., K. U. Duckenfield, E. R. Landa, and E. Callender (2004), Tire-wear particles as a source
624 of zinc to the environment, *Environ. Sci. Technol.*, 38(15), 4206-4214.
- 625
626 DeCarlo, P. F., et al. (2010), Investigation of the sources and processing of organic aerosol over the
627 Central Mexican Plateau from aircraft measurements during MILAGRO, *Atmos. Chem. Phys.*, 10(12),
628 5257-5280.
- 629
630 Dick, W. D., P. J. Ziemann, and P. H. McMurry (2007), Multiangle light-scattering measurements of
631 refractive index of submicron atmospheric particles, *Aerosol Sci. Technol.*, 41(5), 549-569.
- 632
633 Docherty, K. S., et al. (2011), The 2005 Study of Organic Aerosols at Riverside (SOAR-1): instrumental
634 intercomparisons and fine particle composition, *Atmos. Chem. Phys.*, 11(23), 12387-12420.
- 635
636 Dzepina, K., R. M. Volkamer, S. Madronich, P. Tulet, I. M. Ulbrich, Q. Zhang, C. D. Cappa, P. J.
637 Ziemann, and J. L. Jimenez (2009), Evaluation of recently-proposed secondary organic aerosol models
638 for a case study in Mexico City, *Atmos. Chem. Phys.*, 9(15), 5681-5709.
- 639
640 Froyd, K. D., S. M. Murphy, D. M. Murphy, J. A. de Gouw, N. C. Eddingsaas, and P. O. Wennberg
641 (2010), Contribution of isoprene-derived organosulfates to free tropospheric aerosol mass, *Proceedings of*
642 *the National Academy of Sciences of the United States of America*, 107(50), 21360-21365.
- 643

644 Gaston, C. J., K. A. Pratt, X. Y. Qin, and K. A. Prather (2010), Real-Time Detection and Mixing State of
645 Methanesulfonate in Single Particles at an Inland Urban Location during a Phytoplankton Bloom,
646 *Environ. Sci. Technol.*, *44*(5), 1566-1572.

647

648 Grover, B. D., M. Kleinman, N. L. Eatough, D. J. Eatough, R. A. Cary, P. K. Hopke, and W. E. Wilson
649 (2008), Measurement of fine particulate matter nonvolatile and semi-volatile organic material with the
650 Sunset Laboratory Carbon Aerosol Monitor, *J. Air Waste Manage. Assoc.*, *58*(1), 72-77.

651

652 Herndon, S. C., et al. (2008), Correlation of secondary organic aerosol with odd oxygen in Mexico City,
653 *Geophys. Res. Lett.*, *35*(15), L15804.

654

655 Hersey, S. P., J. S. Craven, K. A. Schilling, A. R. Metcalf, A. Sorooshian, M. N. Chan, R. C. Flagan, and
656 J. H. Seinfeld (2011), The Pasadena Aerosol Characterization Observatory (PACO): chemical and
657 physical analysis of the Western Los Angeles basin aerosol, *Atmos. Chem. Phys.*, *11*(15), 7417-7443.

658

659 Hjortenkrans, D. S. T., B. G. Bergback, and A. V. Haggerud (2007), Metal emissions from brake linings
660 and tires: Case studies of Stockholm, Sweden 1995/1998 and 2005, *Environ. Sci. Technol.*, *41*(15), 5224-
661 5230.

662

663 Jakober, C. A., M. J. Charles, M. J. Kleeman, and P. G. Green (2006), LC-MS analysis of carbonyl
664 compounds and their occurrence in diesel emissions, *Anal. Chem.*, *78*(14), 5086-5093.

665

666 Jakober, C. A., M. A. Robert, S. G. Riddle, H. Destailats, M. J. Charles, P. G. Green, and M. J. Kleeman
667 (2008), Carbonyl emissions from gasoline and diesel motor vehicles, *Environ. Sci. Technol.*, *42*(13),
668 4697-4703.

669

670 Kleinman, L. I., et al. (2007), Aircraft observations of aerosol composition and ageing in New England
671 and Mid-Atlantic States during the summer 2002 New England Air Quality Study field campaign, *J.*
672 *Geophys. Res.-Atmos.*, *112*(D9), D09310.

673

674 Lanz, V. A., et al. (2008), Source attribution of submicron organic aerosols during wintertime inversions
675 by advanced factor analysis of aerosol mass spectra, *Environ. Sci. Technol.*, *42*(1), 214-220.

676

677 Liu, S., D. A. Day, J. E. Shields, and L. M. Russell (2011), Ozone-driven daytime formation of secondary
678 organic aerosol containing carboxylic acid groups and alkane groups, *Atmos. Chem. Phys.*, *11*(16), 8321-
679 8341.

680

681 Malm, W. C., J. F. Sisler, D. Huffman, R. A. Eldred, and T. A. Cahill (1994), Spatial and seasonal trends
682 in particle concentration and optical extinction in the united-states, *J. Geophys. Res.-Atmos.*, *99*(D1),
683 1347-1370.

684

685 Middlebrook, A. M., R. Bahreini, J. L. Jimenez, and M. R. Canagaratna (2012), Evaluation of
686 Composition-Dependent Collection Efficiencies for the Aerodyne Aerosol Mass Spectrometer using Field
687 Data, *Aerosol Sci. Technol.*, *46*(3), 258-271.

688
689 Mohr, C., et al. (2011), Identification and quantification of organic aerosol from cooking and other
690 sources in Barcelona using aerosol mass spectrometer data, *Atmos. Chem. Phys.*, *11*(10), 1649-1665.

691
692 Ng, N. L., M. R. Canagaratna, J. L. Jimenez, Q. Zhang, I. M. Ulbrich, and D. R. Worsnop (2011), Real-
693 Time Methods for Estimating Organic Component Mass Concentrations from Aerosol Mass Spectrometer
694 Data, *Environ. Sci. Technol.*, *45*(3), 910-916.

695
696 Paatero, P., and U. Tapper (1994), Positive matrix factorization - a nonnegative factor model with optimal
697 utilization of error-estimates of data values, *Environmetrics*, *5*(2), 111-126.

698
699 Parrish, D. D., A. Stohl, C. Forster, E. L. Atlas, D. R. Blake, P. D. Goldan, W. C. Kuster, and J. A. de
700 Gouw (2007), Effects of mixing on evolution of hydrocarbon ratios in the troposphere, *J. Geophys. Res.-*
701 *Atmos.*, *112*(D10), D10S34.

702
703 Russell, L. M., R. Bahadur, L. N. Hawkins, J. Allan, D. Baumgardner, P. K. Quinn, and T. S. Bates
704 (2009a), Organic aerosol characterization by complementary measurements of chemical bonds and
705 molecular fragments, *Atmos. Environ.*, *43*(38), 6100-6105.

706
707 Russell, L. M., S. Takahama, S. Liu, L. N. Hawkins, D. S. Covert, P. K. Quinn, and T. S. Bates (2009b),
708 Oxygenated fraction and mass of organic aerosol from direct emission and atmospheric processing
709 measured on the R/V Ronald Brown during TEXAQS/GoMACCS 2006, *J. Geophys. Res.-Atmos.*, *114*,
710 D00F05.

711
712 Salma, I., and W. Maenhaut (2006), Changes in elemental composition and mass of atmospheric aerosol
713 pollution between 1996 and 2002 in a Central European city, *Environmental Pollution*, *143*(3), 479-488.

714
715 Schauer, J. J., M. J. Kleeman, G. R. Cass, and B. R. T. Simoneit (1999a), Measurement of emissions from
716 air pollution sources. 2. C-1 through C-30 organic compounds from medium duty diesel trucks, *Environ.*
717 *Sci. Technol.*, *33*(10), 1578-1587.

718
719 Schauer, J. J., M. J. Kleeman, G. R. Cass, and B. R. T. Simoneit (1999b), Measurement of emissions from
720 air pollution sources. 1. C-1 through C-29 organic compounds from meat charbroiling, *Environ. Sci.*
721 *Technol.*, *33*(10), 1566-1577.

722
723 Schauer, J. J., M. J. Kleeman, G. R. Cass, and B. R. T. Simoneit (2002a), Measurement of emissions from
724 air pollution sources. 5. C-1-C-32 organic compounds from gasoline-powered motor vehicles, *Environ.*
725 *Sci. Technol.*, *36*(6), 1169-1180.

726
727 Schauer, J. J., M. J. Kleeman, G. R. Cass, and B. R. T. Simoneit (2002b), Measurement of emissions from
728 air pollution sources. 4. C-1-C-27 organic compounds from cooking with seed oils, *Environ. Sci.*
729 *Technol.*, 36(4), 567-575.

730
731 Sommariva, R., J. A. de Gouw, M. Trainer, E. Atlas, P. D. Goldan, W. C. Kuster, C. Warneke, and F. C.
732 Fehsenfeld (2011), Emissions and photochemistry of oxygenated VOCs in urban plumes in the
733 Northeastern United States, *Atmos. Chem. Phys.*, 11(14), 7081-7096.

734
735 Sun, Y. L., et al. (2011), Characterization of the sources and processes of organic and inorganic aerosols
736 in New York city with a high-resolution time-of-flight aerosol mass spectrometer, *Atmos. Chem. Phys.*,
737 11(4), 1581-1602.

738
739 Thompson, J., P. L. Hayes, J. L. Jimenez, K. Adachi, X. Zhang, J. Liu, R. J. Weber, and P. R. Buseck
740 (2012), Aerosol Optical Properties at Pasadena, CA During CalNex 2010, *Atmos. Environ.*, 55, 190.

741
742 Turpin, B. J., and H. J. Lim (2001), Species contributions to PM_{2.5} mass concentrations: Revisiting
743 common assumptions for estimating organic mass, *Aerosol Sci. Technol.*, 35(1), 602-610.

744
745 Ulbrich, I. M., M. R. Canagaratna, Q. Zhang, D. R. Worsnop, and J. L. Jimenez (2009), Interpretation of
746 organic components from Positive Matrix Factorization of aerosol mass spectrometric data, *Atmos. Chem.*
747 *Phys.*, 9(9), 2891-2918.

748
749 Unnikrishnan, K. P., and E. T. Thachil (2006), Toughening of epoxy resins, *Des. Monomers Polym.*, 9(2),
750 129-152.

751
752 Washenfelder, R. A., et al. (2011), The glyoxal budget and its contribution to organic aerosol for Los
753 Angeles, California, during CalNex 2010, *J. Geophys. Res.-Atmos.*, 116, D00V02.

754
755 Williams, B. J., A. H. Goldstein, N. M. Kreisberg, and S. V. Hering (2006), An in-situ instrument for
756 speciated organic composition of atmospheric aerosols: Thermal Desorption Aerosol GC/MS-FID (TAG),
757 *Aerosol Sci. Technol.*, 40(8), 627-638.

758
759 Williams, B. J., A. H. Goldstein, N. M. Kreisberg, S. V. Hering, D. R. Worsnop, I. M. Ulbrich, K. S.
760 Docherty, and J. L. Jimenez (2010), Major components of atmospheric organic aerosol in southern
761 California as determined by hourly measurements of source marker compounds, *Atmos. Chem. Phys.*,
762 10(23), 11577-11603.

763
764 Wood, E. C., et al. (2010), Investigation of the correlation between odd oxygen and secondary organic
765 aerosol in Mexico City and Houston, *Atmos. Chem. Phys.*, 10(18), 8947-8968.

766

767 Young, C. J., et al. (2013), Evaluating evidence for Cl sources and oxidation chemistry in a coastal, urban
768 environment, *Atmos. Chem. Phys. Discuss.*, *Accepted*.

769
770 Zhang, Q., D. R. Worsnop, M. R. Canagaratna, and J. L. Jimenez (2005), Hydrocarbon-like and
771 oxygenated organic aerosols in Pittsburgh: insights into sources and processes of organic aerosols, *Atmos.*
772 *Chem. Phys.*, *5*, 3289-3311.

773
774 Zhang, Q., et al. (2007), Ubiquity and dominance of oxygenated species in organic aerosols in
775 anthropogenically-influenced Northern Hemisphere midlatitudes, *Geophys. Res. Lett.*, *34*(13), L13801.

776
777 Zorn, S. R., F. Drewnick, M. Schott, T. Hoffmann, and S. Borrmann (2008), Characterization of the
778 South Atlantic marine boundary layer aerosol using an aerodyne aerosol mass spectrometer, *Atmos.*
779 *Chem. Phys.*, *8*(16), 4711-4728.

780
781
782